

# Detection of Coal Fires in Soma with Landsat Temporal Thermal Images

Submitted to the Graduate School of Natural and Applied Sciences  
in partial fulfillment of the requirements for the degree of

Master of Science

in Geomatics Engineering

by

Merve KÖŞKER

Thesis Advisor: Prof. Dr. Özşen ÇORUMLUOĞLU

June 2022

This is to certify that we have read the thesis **Detection of Coal Fires in Soma with Landsat Temporal Thermal Images** submitted by **Merve KÖŞKER**, and it has been judged to be successful, in scope and in quality, at the defense exam and accepted by our jury as a MASTER'S THESIS.

**APPROVED BY:**

**Advisor:** **Prof. Dr. Özşen ÇORUMLUOĞLU** .....  
İzmir Kâtip Çelebi University

**Committee Members:**

**Assist.Prof.Dr.Fatih TAKTAK** .....  
Uşak University

**Assist. Prof. Dr. Mehmet Güven KOÇAK** .....  
İzmir Kâtip Çelebi University

**Date of Defense: June 02, 2022**

# Declaration of Authorship

I, **Merve KÖŞKER**, declare that this thesis titled **Detection of Coal Fires in Soma with Landsat Temporal Thermal Images** and the work presented in it are my own.

I confirm that:

- This work was done wholly or mainly while in candidature for the Master's degree at this university.
- Where any part of this thesis has previously been submitted for a degree or any other qualification at this university or any other institution, this has been clearly stated.
- Where I have consulted the published work of others, this is always clearly attributed.
- Where I have quoted from the work of others, the source is always given. This thesis is entirely my own work, with the exception of such quotations.
- I have acknowledged all major sources of assistance.
- Where the thesis is based on work done by myself jointly with others, I have made clear exactly what was done by others and what I have contributed myself.

Signature:

---

Date: 02.06.2022

---

# Detection of Coal Fires in Soma with Landsat Temporal Thermal Images

## Abstract

Coal is one of the most important energy resources used in many countries for decades to produce energy. A type of fire called coal fires occurs when the coal surface is exposed to sunlight and in contact with oxygen for a long time in coal mine areas where coal is extracted. Coal fires are prevalent and critical incidents for most coal mining areas around the world. Various problems arise due to coal fires in coal mines. These problems affect many factors such as environment, society, economy and security directly or indirectly. Burning coal fire causes the formation of poisonous gases, particles and condensation by-products, making it a great disaster for the environment and nature. It should not be forgotten that coal fires, which irreversibly damage the surrounding geology, nature, soil and atmosphere, cause waste of valuable natural resources and economic losses. Investigating and monitoring the condition of coal mines is utterly useful and necessary. The fire crisis can be managed well by obtaining sufficient information on the status and magnitude of coal fires. The science of remote sensing has eased the identification and dynamic monitoring of coal fires in a wide coal mine area by using multi-temporal satellite image data. Soma (Manisa) coal mine area is chosen as the study area. To identify coal fires, retrieval of land surface temperatures (LST) of landsat satellite images are done. Firstly, the land surface temperatures (LST) were retrieved by using a single channel algorithm on the Landsat 5 TM thermal infrared band and Landsat 8 OLI/TIRS thermal infrared band.

Afterwards, a number of analyzes were done to check accuracy of the results. Finally, 18 Landsat 8 OLI/TIRS land surface temperature (LST) images were mapped and 3 period coal fire maps were created.

**Keywords:** Remote Sensing, Soma, Coal Fires, Landsat Satellite Images, Land Surface Temperatures

# Landsat Temporal Termal Görüntüleri ile Soma'da Kömür Yangınlarının Tespiti

## ÖZ

Kömür, pek çok ülkede on yıllardır enerji elde etmek amacıyla kullanılan önemli enerji kaynaklarından biridir. Kömür çıkarımı yapılan kömür madeni sahalarında kömür yüzeyinin güneş ışığına uzun bir süre maruz kalmasıyla ve oksijenle temas halinde olmasıyla birlikte kömür yangınları denilen yangın çeşidi ortaya çıkar. Kömür yangınları, dünya çapındaki çoğu kömür madeni alanı için yaygın ve kritik bir olaydır. Kömür madenlerindeki yangınlar nedeniyle çeşitli problemler ortaya çıkar. Bu problemler; çevre, toplum, ekonomi ve güvenlik gibi birçok unsuru doğrudan veya dolaylı bir şekilde etkiler. Yanan kömür yangını; zararlı gazların, partiküllerin ve yoğunlaşma yan ürünlerinin oluşmasına sebebiyet vererek çevre ve doğa için büyük bir felaket haline gelir. Etraftaki jeolojiye, doğaya, toprağa ve atmosfere geri döndürülemeyecek kadar büyük oranda zarar veren kömür yangınlarının değerli doğal kaynak israfına ve ekonomik kayıplara yol açtığı da unutulmamalıdır. Kömür madenlerinin durumunu araştırmak ve izlemek son derece yararlı ve gereklidir. Kömür yangınlarının durumu ve büyüklüğü ile ilgili yeterli bilgiye ulaşılarak yangın krizi iyi bir şekilde yönetilebilir. Uzaktan algılama bilimi, çok zamanlı uydu görüntüleri kullanarak geniş bir kömür madeni alanında kömür yangınlarının tanımlanmasını ve dinamik olarak izlenmesini kolaylaştırmıştır. Çalışma alanı olarak Soma (Manisa) kömür madeni sahası seçilmiştir. Kömür yangınlarını belirlemek için, landsat uydu görüntülerinin arazi yüzey sıcaklıklarının (LST) hesaplandı. İlk olarak, Landsat 5 TM

termal kızılötesi bandı ve Landsat 8 OLI/TIRS termal kızılötesi bandı üzerinde tek kanal algoritması kullanılarak arazi yüzey sıcaklıkları (LST) elde edilmiştir. Daha sonra, elde edilen sonuçların doğruluğunu araştırmak için çeşitli analizler yapılmıştır. Son olarak, 18 tane Landsat 8 OLI/TIRS arazi yüzey sıcaklık görüntüsü haritalandı ve 3 periyotluk kömür yangını haritaları oluşturuldu.

**Anahtar Kelimeler:** Uzaktan Algılama, Soma, Kömür Yangınları, Landsat Uydu Görüntüleri, Arazi Yüzey Sıcaklıkları

*The thesis is dedicated to my family.*



# Acknowledgment

I would like to express my thanks of gratitude to my supervisor Prof. Dr. Özşen Çorumluođlu to help me to do this thesis.

# Table of Contents

Declaration of Authorship .....	ii
Abstract .....	iii
Öz .....	v
Acknowledgment .....	viii
List of Figures .....	xii
List of Tables.....	xvi
List of Abbreviations.....	xvii
List of Symbols .....	xiv
<b>1 Introduction .....</b>	<b>1</b>
1.1 Coal Fires .....	2
1.2 Spontaneous Combustion of Coal Fires .....	3
1.3 Impacts of Coal Fires .....	5
1.4 Detection of Coal Fires by Remote Sensing .....	8
1.5 Objectives of The Thesis .....	13
<b>2 Materials and Methods .....</b>	<b>14</b>
2.1 Study Area .....	14
2.1.1 Geographic Location of Soma.....	14
2.1.2 Geological Structure of Soma.....	16
2.1.3 Coal Mining in Soma.....	18
2.2 Data .....	21
2.2.1 Landsat 5 TM.....	22
2.2.2 Landsat 8 OLI/TIRS .....	24

2.3	Remote Sensing Techniques For Coal Fire Detection.....	26
2.3.1	Optical Satellite Data.....	28
2.3.2	Thermal Satellite Data.....	29
2.3.3	Thermal Infrared Data Used For Detecting Coal Fire Areas.....	31
<b>3</b>	<b>Data Acquisition and Preprocessing.....</b>	<b>33</b>
3.1	Landsat Data Acquisition.....	34
3.1.1	Procedure For Downloading Landsat Data .....	36
3.2	Landsat Image Data Preprocessing.....	36
3.2.1	Geometric Correction .....	38
3.2.2	Radiometric Correction .....	38
3.2.2.1	Conversion of Digital Numbers (DN) to Top of Atmospheric Spectral Radiance ( $L\lambda$ ).....	38
3.2.2.2	Conversion of Spectral Radiance ( $L\lambda$ ) to Reflectance ( $\rho\lambda$ )	40
3.2.2.3	Conversion of Spectral Radiance ( $L\lambda$ ) to Brightness Temperature (BT).....	41
3.2.2.4	Dark Object Subtraction (Histogram Minimum Method)..	41
<b>4</b>	<b>Data Processing.....</b>	<b>46</b>
4.1	Estimation of Land Surface Emissivity by Using Normalized Difference Vegetation Index (NDVI) .....	46
4.1.1	The Normalized Difference Vegetation Index (NDVI).....	48
4.1.2	The Land Surface Emissivity (LSE).....	52
4.2	Retrieval of The Land Surface Temperature (LST).....	52
4.2.1	The Single Channel Algorithm for The Retrieval of Land Surface Temperature (LST) .....	54
4.2.1.1	The Computation of Simulated Single Image (SSI) of Landsat 5 TM and Landsat 8 OLI/TIRS Land Surface Temperature (LST) Data.....	58
4.2.1.2	Evaluation of Landsat 8 OLI/TIRS Simulated Single Image (SSI) by Creating Threshold Value .....	61
4.2.1.3	Normalized Land Surface Temperature Calculation.....	62

4.2.1.4 The Assessment of Hot Spots from The Landsat 8 OLI/TIRS  
SSI LST Data in the Licensed Coal Mine Areas in Soma.. 66

**5 Results and Discussions..... 71**

**6 Conclusions ..... 90**

# List of Figures

Figure 1.1	Coal oxidizes as a result of contact with oxygen and starts to burn .....	2
Figure 1.2	Visual expression of spontaneous combustion of coal .....	4
Figure 1.3	Coal fires may cause serious problems to living life and nature.....	5
Figure 1.4	Surface Coal Mining Activities.....	7
Figure 1.5	Underground Coal Mining .....	8
Figure 2.1	Geographic Location of Soma.....	15
Figure 2.2	General Stratigraphic Sections for The Soma Coal Basin .....	17
Figure 2.3	Licensed Coal Mine Areas in Soma .....	18
Figure 2.4	(a) Deniz Bunker Area, (b) Deniz Open Pit Mining Area 1, (c) Deniz Open Pit Mining Area 2.....	19
Figure 2.5	(a) Soma Sarıkaya Telsiz Open Pit Mining Area 1, (b) Soma Sarıkaya Telsiz Open Pit Mining Area 2 .....	20
Figure 2.6	Soma Kısırakdere Işıklar Open Pit Mining Management, Soma Kısırakdere Işıklar Open Pit Mining Area 1, Soma Kısırakdere Işıklar Open Pit Mining Area 2... ..	20
Figure 2.7	(a) Soma Eynez Open Pit Mining Area 1, (b) Soma Eynez Open Pit Mining Area 2, (c) Soma Eynez Open Pit Mining Area 3, (d) Soma Eynez Open Pit Mining Area 4.....	20
Figure 2.8	(a) Deniz Dedetaşı C Panel Open Pit Mining Area 1, (b) Deniz Dedetaşı C Panel Open Pit Mining Area 2, (c) Deniz Dedetaşı C Panel Open Pit Mining Area 3, (d) Soma Elmalı Mining Area .....	21
Figure 2.9	Spectral Bands and Wavelengths of the Landsat 5 TM Satellite Sensor Landsat sensors, spectral channels and band-passes, superimposed on atmospheric transmission percentage (grey background). MSS: Landsat-1 through -5; TM: Landsat-4 and -5; ETM+: Landsat-7; OLI and TIRS: Landsat-8.....	22
Figure 2.10	Spectral response for Landsat 4 TM6, Landsat 5 TM6, Landsat 7 ETM+ 6, and Landsat 8 TIRS1 .....	26

Figure 2.11 The Electromagnetic Spectrum.....	30
Figure 3.1 Flowchart of Image Preprocessing .....	37
Figure 3.2 Illustration of the path radiances of the geographical objects .....	43
Figure 3.3 An illustration of solar radiation to explain atmospheric effects.....	44
Figure 3.4 An example image of the radiometrically corrected Landsat 5 TM and Landsat 8 OLI/TIRS satellite images .....	45
Figure 3.5 An subset image of the radiometrically corrected Landsat 5 TM and Landsat 8 OLI/TIRS satellite images.....	45
Figure 4.1 Flowchart of image processing.....	47
Figure 4.2 Correlation of plant health and bands of visible red and near-infrared that used for obtaining NDVI values.....	50
Figure 4.3 An example NDVI image which were generated by implementing Landsat 5 TM and Landsat 8 OLI/TIRS satellite images .....	51
Figure 4.4 The Simulated Single Image (SSI) of 25 Landsat 5 TM land surface temperature images and 18 Landsat 8 OLI/TIRS land surface temperature (LST) images (band 10) .....	60
Figure 4.5 The LST SSI Band 10 and 11 Correlation.....	61
Figure 4.6 Normalized land surface temperature images of the Landsat 5 TM and Landsat 8 OLI/TIRS satellites.....	62
Figure 4.7 The Normalized LST SSI Band 10 and 11 Correlation of Landsat 8.....	63
Figure 4.8 The Landsat 8 OLI/TIRS simulated single threshold LST image for Band 10.....	63
Figure 4.9 The Landsat 8 OLI/TIRS simulated single threshold LST image for Band 11.....	64
Figure 4.10 The Landsat 8 Threshold Normalized LST SSI Band Correlation Graphic.....	64
Figure 4.11 The Normalized threshold LST simulated single image of Landsat 5 TM.....	65
Figure 4.12 Landsat 5 Band 6 and Landsat 8 TIRS Band 10 Correlation Graph of Normalized Threshold LST SSI values.....	66

Figure 4.13	The SSI LST image from 18 Landsat 8 OLI/TIRS LST data using Band 11.....	67
Figure 4.14	The SSI LST images from 7 years of Landsat 8 OLI/TIRS LST data using Band 10 (a) and Band 11 (b).....	68
Figure 4.15	Assessment of licensed coal mine areas in Soma under coal fire threat by Landsat 8 OLI/TIRS SSI Data using Band 10 (a) and Band 11 (b).....	68
Figure 4.16	The Correlation Graphics of the 3 Landsat 8 OLI/TIRS Land Surface Temperature (LST) Data (a) 20130721, (b) 20160729 and (c) 20190731 .....	69
Figure 5.1	The land surface temperature (LST) maps of 18 Landsat 8 OLI/TIRS data with Band 10 (a) 2013.07.21, (b) 2013.07.30, (c) 2014.10.21, (d) 2014.11.06, (e) 2015.07.20, (f) 2015.07.27, (g) 2016.07.13, (h) 2016.07.22, (i) 2016.07.29 (j) 2017.07.09, (k) 2017.07.25, (l) 2018.07.03, (m) 2018.08.13, (n) 2019.07.06, (o) 2019.07.31, (p) 2020.07.01, (r) 2020.07.17, and (s) 2020.07.24.....	76
Figure 5.2	The map of Landsat 8 OLI/TIRS SSI image which were produced from 18 Landsat 8 OLI/TIRS land surface temperature (LST) data with Band 10 .....	76
Figure 5.3	The map of Landsat 8 OLI/TIRS SSI image which were produced from 7 Landsat 8 OLI/TIRS land surface temperature (LST) data with Band 10.....	77
Figure 5.4	The land surface temperature (LST) maps of 18 Landsat 8 OLI/TIRS data with Band 11 (a) 2013.07.21, (b) 2013.07.30, (c) 2014.10.21, (d) 2014.11.06, (e) 2015.07.20, (f) 2015.07.27, (g) 2016.07.13, (h) 2016.07.22, (i) 2016.07.29 (j) 2017.07.09, (k) 2017.07.25, (l) 2018.07.03, (m) 2018.08.13, (n) 2019.07.06, (o) 2019.07.31, (p) 2020.07.01, (r) 2020.07.17, and (s) 2020.07.24.....	81
Figure 5.5	The map of Landsat 8 OLI/TIRS SSI image which were produced from 18 Landsat 8 OLI/TIRS land surface temperature (LST) data with Band 11 .....	82

Figure 5.6	The map of Landsat 8 OLI/TIRS SSI image which were produced from 7 Landsat 8 OLI/TIRS land surface temperature (LST) data with Band 11.....	82
Figure 5.7	The three coal fire maps of Soma (a) 20130721, (b) 20160729 and (c) 20190731 .....	85
Figure 5.8	The Correlation Graphic of the Landsat 8 SSI LST Band 10 Threshold Values and the 2013.07.21 Landsat 8 LST Band 10 Threshold Values..	86
Figure 5.9	The Correlation Graphic of the Landsat 8 SSI LST Band 10 Threshold Values and the 2016.07.29 Landsat 8 LST Band 10 Threshold Values.....	86
Figure 5.10	The Correlation Graphic of the Landsat 8 SSI LST Band 10 Threshold Values and the 2019.07.31 Landsat 8 LST Band 10 Threshold Values..	87
Figure 5.11	The Google Earth display of Soma open pit mine and matching threshold coal fire pixels of (a) SSI Band 10 Threshold data, (b) 20130721, (c) 20160729 and (d) 20190731 .....	89



# List of Tables

Table 2.1	Characteristics of Landsat 8 Satellite Bands .....	25
Table 3.1	Qualifications of The Obtained Landsat 5 TM Satellite Data.....	34
Table 3.2	Qualifications of The Obtained Landsat 8 OLI/TIRS Satellite Data .....	35
Table 4.1	The Interval of NDVI Values According to The Type of Land Cover....	49

# List of Abbreviations

TM	Thematic Mapper
SPOT	Satellite Pour l'Observation de la Terre
CBERS	China–Brazil Earth Resources Satellite program
NOAA	National Oceanic and Atmospheric Administration
AVHRR	The Advanced Very High Resolution Radiometer
MODIS	The Moderate Resolution Imaging Spectroradiometer
ETM+	The Enhanced Thematic Mapper Plus
OLI/TIRS	Operational Land Imager/Thermal Infrared Sensor
ASTER	The Advanced Spaceborne Thermal Emission and Reflection Radiometer
BIRD	Bi-spectral Infrared Detection
LULC	Land Use and Land Cover
LST	Land Surface Temperature
TIR	Thermal Infrared
NDVI	The Normalized Difference Vegetation Index
LSE	Land Surface Emissivity
USGS	The United States Geological Survey
SWIR	Shortwave Infrared
LDCM	Landsat Data Continuity Mission
ATSR	Along Track Scanning Radiometer
MSS	Multispectral Scanner
NASA	National Aeronautics and Space Administration
TIRS	Thermal Infrared Sensor

SWIR	Short-wave Infrared
NIR	Near-Infrared
DN	Digital Numbers
ToA	Top of Atmosphere
DOS	Dark Object Subtraction
AOI	Area of Interest
SC	Single Channel
RTE	Radiative Transfer Equation
MW	Mono-Window
GSC	Generalized Single-Channel
AWV	Atmospheric Water Vapor
NSAT	Near Surface Air Temperature
SLA	The Smallest Parts of Lands
VCR	Variable Rate of Change
SSI	Simulated Single Image

# List of Symbols

$\alpha$	Alpha
$^{\circ}\text{C}$	Celsius
CO	Carbon Monoxide
H <sub>2</sub>	Hydrogen
SO <sub>2</sub>	Sulphur Dioxide
NO	Nitrogen Oxide
CO	Carbon Monoxide
CO <sub>2</sub>	Carbon Dioxide
CH <sub>4</sub>	Methane
$\mu\text{m}$	Micrometer
$L\lambda$	Top of Atmospheric Spectral Radiance
$\rho$	Reflectance
$T_{\text{sensor}}$	Brightness Temperature
F	Force [N]
m	Mass [kg]
$\varepsilon$	Emissivity

# Chapter 1

## Introduction

Coal is a sedimentary rock composed of organic and inorganic components that are formed as a result of the compression and solidification of plant residues and inorganic minerals under high pressure and temperature [1]. The accumulation of plants and trees remains in the swamps. Physical (pressure, precipitation, etc.) and chemical events (heat, degradation and transformation) occur for the carbonization process to take place. Eventually, the precipitation, alteration with chemical matters and physical effects over millions of years create coal. Geological time is one of the important parameters in the coalization process.

The carboniferous, permian and crater-tertiary periods are the periods of the carbonization. The formation process of coal can be briefly summarized as follows:

- The first phase is the accumulation and precipitation of plants,
- The second phase is the biochemical and geochemical degradation, and
- In the third phase, the physical, petrographic and chemical properties are formed by thermochemical transformations.

The energy that plants absorbed from the Sun a very long time ago is derived from coal [2]. Coal has many different application areas and it is a beneficial energy source for many industrial sectors. The mining industry, which contributes to the economy of many countries, unfortunately leads to the onset of environmental degradation due to various reasons such as coal fires. Mining activities cause friction and heat generation. The friction and heat make a coal fire, which is caused by the coal itself burning on its own [3].

## 1.1 Coal Fires

Coal fires have become a phenomenon seen in plenty of coal mine areas where coal reserves are extracted. Coal fires, which are also referred to as coal seam fires, can form in underground habitats on the surface of the Earth [4]. The cause of coal fires is that coal oxidizes as a result of contact with oxygen and starts to burn spontaneously. It has been claimed that the spontaneous combustion potential of coal is effective in increasing the oxidation of coal at ambient temperatures [5]. The ignition or flash point of the coal takes place at the threshold temperature. Thus, coal starts to burn and coal fires materialize [6]. With coal emerging to the surface and oxygen absorption, the threshold temperature rises from 230 °C to 280 °C. Therefore, the reaction that occurs when coal reacts with oxygen is considered as an exothermic reaction. It is a great advantage that the high temperature difference caused by the presence of coal fires in coal mine areas can be used in determining the locations of coal fires [7]. Figure 1.1 is an image about coal combustion.



Figure 1.1: Coal oxidizes as a result of contact with oxygen and starts to burn [8]

Coal fires can cause higher temperatures on the land surface than the surrounding background. If the amount of heat which is released as a result of the reaction of coal with oxygen is not sufficiently dispersed, the coal temperature increases. When the increasing temperature reaches a certain value (threshold temperature interval), which is between 80°C-130 °C, the coal starts to burn [9-13]. The total temperature of a pixel varies according to the location, spread, surface type, and temperature of the coal fire

area and its surroundings. The temperature caused by surface coal fires is normally 400°C higher than the background. The temperature change caused by underground coal fires varies depending on e.g. location, measuring time, weather conditions, etc.

## 1.2 Spontaneous Combustion of Coal Fires

Coal has a structure that can be easily ignited. It should not be forgotten that coal material is flammable. Coal fires are a type of event that occurs very frequently and should be taken seriously. One of the elements that contribute to the formation of coal fires is the spontaneous combustion of coal. The occurrence of coal fires depends on the presence of the following three factors in the same environment: temperature, fuel (in this case, coal), and, oxygen.

The spontaneous combustion of coal can be examined on three different headings. These are coal properties, coal seam properties and external impacts. In addition, there are other factors that can be examined under subheadings which affect the spontaneous combustion of coal depending on these three main factors. Coal rank, inherent moisture content, sulfur content, ash content and maceral composition are among the factors that affect the properties of coal. The depth and thickness of the coal seam can cause the coal seam properties to change. Rainfall, wind, ambient temperature and humidity level are included in external factors affecting the spontaneous combustion of coal [13].

Coal fires gradually expand and sprawl on the land surface of coal dumps or coal seams as a result of spontaneous combustion over time. Such seriously spreading coal fires should be detected and controlled immediately [14,15]. The spontaneous combustion of coal can be natural (lightning, forest fires and peat fires) or human-induced (mining and domestic fires) [16]. This is especially valid for those arising in the underground coal seam.

The contact of the coal material with oxygen triggers the spontaneous combustion of the coal. This is the main reason why the coal oxidation started. The formula of the coal oxidation (Equation 1.1) is given as follows [17]:



Fires caused by the spontaneous combustion of coal often start with massive temperature increases, which are referred as "hot spots" in the deepest parts of the coal beds. Herewith, the temperature of the coal tends to stay above the ambient temperature. The temperature of the coal gradually rises to a threshold temperature range of 80 °C to 130 °C. In this temperature range, carbon monoxide (CO) and hydrogen (H<sub>2</sub>) are produced. Eventually, a stable reaction occurs. This reaction is exothermic due to the temperature released as a result of the reaction. Once the threshold temperature is reached, the heat that is generated by the reaction rises at a rapid rate. The temperature of the coal continues to increase until it reaches the interval from 230 °C to 280 °C. The temperature of the coal rises until combustion starts. The combustion and self-ignition of the coal ensue in flames. In a sense, the coal starts to burn. Figure 1.2 summarizes the process of spontaneous coal combustion.

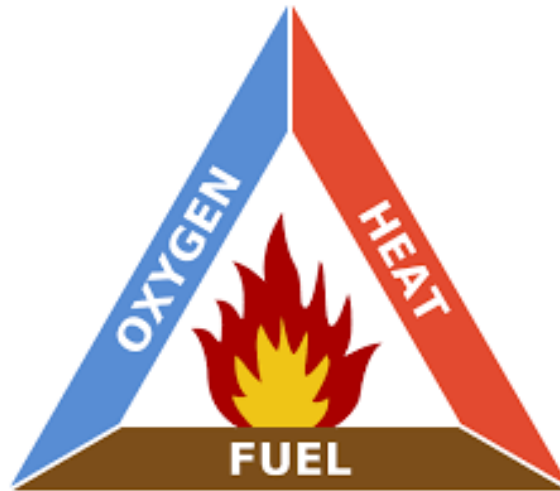


Figure Hata! Belgede belirtilen stilde metne rastlanmadı..2: Visual expression of spontaneous combustion of coal [18]

The quality of the coal and the size of the particles affect the spontaneous combustion of the coal. For example, high ranking coals with high carbon content are very susceptible to burning [13]. The large surface areas of the coal particles also allow the combustion reaction to spread easily and quickly [19].



Coal mining methods applied to extract coal cause cracks and fissures in the coal mine area. In this way, the air passes through these cracks and fissures to the coal seams and underground coal. Thus, coal fires occur. Local climatic conditions are another important factor that can change the balance in the reaction of coal with oxygen. These are some of the environmental factors that may come to mind in the oxidation reaction of coal [13].

### 1.3 Impacts of Coal Fires

The spread of coal fires to the environment poses a great danger to people and other creatures living in the vicinity. Land subsidence, one of the adverse effects of coal fires, causes the land and vegetation cover to deteriorate. Besides, it causes noticeable damage to buildings, roads, railways and similar infrastructures. Figure 1.3 shows an example of coal fire incidents.



Figure 1.3: Coal fires may cause serious problems to living life and nature [20]

The impacts of coal fires have been determined by several studies, and it has been revealed that these impacts change the dynamics of nature, global and local environment, human health, the economy, social life and many other factors in many ways. Sulphur dioxide ( $\text{SO}_2$ ), nitrogen oxide ( $\text{NO}$ ), carbon monoxide ( $\text{CO}$ ), carbon dioxide ( $\text{CO}_2$ ), methane ( $\text{CH}_4$ ) [21] and similar greenhouse gases, windblown ash, smoke and dust could be released to nature through cracks and fissures in the coal mine

area. As a result of the burning of excess coal, land subsidence and collapse can be seen. Even desertification may occur after land subsidence, vegetation loss and even because of heat. Aside from the significant impact on an area and its surroundings where a coal fire broke out, the coal reserves in the coal mine area are greatly reduced and their economic contribution decreases. In the light of this information, it should be taken into account that coal fires adversely affect environment and may cause climate change, global warming, and similar horrible disasters that should be taken seriously depending on the increase in the temperature of the coal fire area.

It is a fact that mining activities make economic contributions to the region where they operate. However, these activities also have negative effects on the environment in which they are located. Other than those mentioned above, there are also some other negative effects such as dust, noise, vibration, explosion, displacement and loss of water resources in open pits. In underground pits, negative effects such as the formation of degradation and the drainage of groundwater out of the pit occur. The negativities arising from coal preparation and washing activities are the effects of solid and liquid wastes to disrupting the ecological balance. Acid rain occurs as a result of the mixing of poisonous gases and other particles with the use of coal as fuel.

Surface mining is an extremely prevalent type of mining that can be done in large areas. Examples of surface mining techniques are open-pit mining, mountain top removal mining, strip mining, etc. By applying surface mining procedures, soil and rock layers on a shallow ore deposit are removed from their places, thus providing access to the ore deposit. The disposal of unnecessary material removed during the excavation of the coal mine surface in surrounding areas leads to undesirable changes in the entire land cover and land use. For this reason, it is necessary to determine the areas where surface mining is applied to understand whether land cover and land use in the coal mine area and its surroundings have undergone any change. Determination of coal surface mining areas with satellite imagery also incorporates land use and land cover changes in mining areas; coal mine area monitoring; mine wastewater management; detection and monitoring of coal seams; reclamation of mined areas; and so on.

Surface mining is considered to be very advantageous for mining industry. Nevertheless, it should not be widely used due to its negative effect to the vegetation

cover and the freshwater bodies and the damage in the ecological environment. The desertification of coal mine soil is another negative effect of surface mining [22,23]. Surface mining, which is applied in very large areas, causes a decrease in the yield of the mineral soil and a decrease in biological diversity [24]. In addition, forests are inevitably destroyed by open pit mining activities. In Figure 1.4, surface coal mining activities are shown.

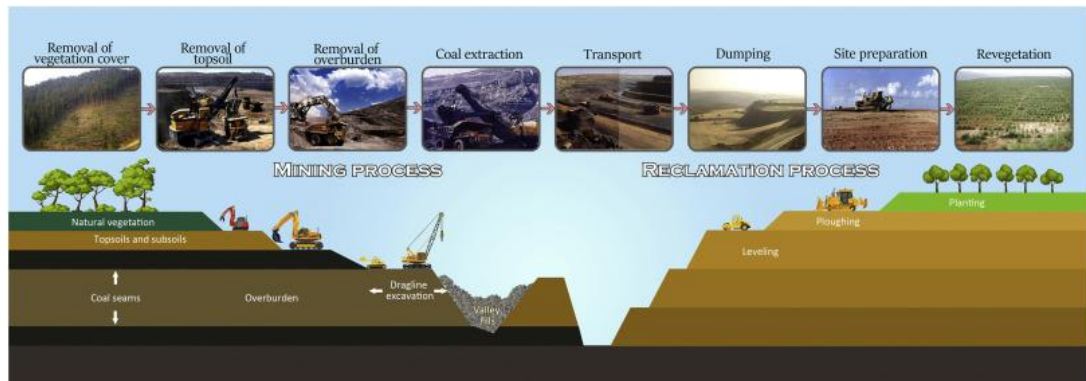


Figure 1.4: Surface Coal Mining Activities [25]

Surface coal fires and underground coal fires are dangerous hazards that can occur in underground coal seams, stored coal piles, and on damaged surface dumps of many coal mine areas. Coal surface fires originating from open cast mining could cause a great disaster if not controlled. The continually burning coal fire in coal seams interrupts environmental, ecological, and social welfare activities. Surface temperature anomalies develop as a result of the release of heat and gases through cracks and fissures in the surface of the coal mine area.

Surface coal fires can be detected from radiant temperature with derivation of a cut-off temperature which is used for separating coal mine fire pixels from non-coal mine fire pixels when thermal imagery is used. The cut-off temperature is controlled by temperature contrast between coal fire and several other elements such as rocks, vegetation, etc. This temperature contrast can be influenced by many related factors in the coal mine area, and these factors can be reproduced by giving examples such as variability of rock types, proportion of vegetation, intensity of coal fires. Figure 1.5 shows an example of underground coal mine area.



Figure 1.5: Underground Coal Mining [26]

In cases where surface coal mining methods are inadequate, underground mining methods come into play. Underground mining is a method carried out by opening one or more portals or shafts that reach deep coal seams, and thus extracting coal from underground. Underground coal mine fires are ignited by natural means or human error. These fires play an active role in the pollution of the atmosphere, acid rains, and the increase of coronary and respiratory diseases. Depletion of valuable and non-renewable energy resources and destruction of floral and fauna habitats are due to these fires, and living life is threatened by temperature changes, landslide, land subsidence and pollution.

## 1.4 Detection of Coal Fires by Remote Sensing

Identification of coal fires is possible by detecting changes in land surface temperature values [16] because of the thermal anomalies. The surface emissivity of the land should be known so that more reliable land surface temperatures can be obtained from thermal infrared data. When coal fires do not dominate the coal mine and its surroundings, the land surface temperature is lower, so that high land surface temperatures indicate coal fires in coal mines and their surrounding areas.

The use of remote sensing techniques for the detection of coal fires was first seen in the 1960s [27]. Spatial data has been collected with airborne and spaceborne techniques since the 1960s, thus this advancement has enabled us to identify and monitor coal fires in a quick way. Detection and monitoring of coal fires by remote

sensing data has gradually started to improve and develop with the contribution of research and studies over time. Black & white and color aerial photographs are used to identify coal fires by using airborne remote sensing techniques [27]. Spaceborne remote sensing utilizes spatial information from Landsat TM (Thematic Mapper), SPOT (Satellite Pour l'Observation de la Terre), CBERS (China–Brazil Earth Resources Satellite program), IKONOS, NOAA (National Oceanic and Atmospheric Administration), Quickbird and similar satellite and radar systems to detect and monitor coal fires [28-34]. The main reasons why remote sensing images have been mostly preferred in recent years are that satellite images can efficiently cover large-scale areas and easily collect information about coal fires caused by spontaneous combustion in a large-scale mine area. In these ways, the remote sensing-based methods are better than traditional point-based geophysical exploration methods, and the remote sensing-based methods can be used to make up for the flaws in the traditional point-based geophysical exploration methods.

Apart from remote sensing, many methods are used to detect coal fires in coal mines: Radon measurement technique, borehole temperature measurement technique, gas measurement technique, and so on. These methods are effectively implemented to determine the location, scope and trend of coal fire areas.

Generally, three main methods are used to detect coal fires in coal mines:

- borehole temperature measurements,
- airborne remote sensing techniques, and
- spaceborne remote sensing techniques.

The borehole temperature measurement method is quite useful for detecting coal fires because the measured abnormally high temperatures helps to locate coal fires at close range. In order to detect the high temperatures caused by the fire, temperature measurements are made with a cabled thermocouple or thermometer in the borehole. In addition, this method allows direct measurement of coal fires. Unfortunately, the method of borehole temperature measurements is designed to collect the necessary amount of data for investigations in very small areas. Also, this method is very expensive when it is compared with image-based other coal fire detection methods.

The radioactive and resistivity methods are some of the several variants of the geophysical method. High temperatures are detected as a result of the alpha ( $\alpha$ ) particle being measured if the radioactive method is preferred. The presence of a large majority of alpha particles indicates where there are high temperatures, that is, where coal fires occur. In the resistivity method, the electrical resistance of the burned rocks is calculated by the electric poles. Thus, the obtained electrical resistance values can be compared with the electrical resistance of the rocks in the unburned state, and coal fires can be traced. Thermo-composition studies are also carried out in order to obtain information about the status of coal fires in areas where mines are concentrated. For this, thermal infrared cameras are acquired, and each pixel detected from the ground gives the temperature value of that place.

The main weaknesses of the methods other than the remote sensing techniques, which were briefly introduced above, are that they prolong the data collection process, make it difficult to search for repetitive procedures, are not suitable for large areas, and so on. For this reason, remote sensing methods are among the most preferred methods in the investigation of coal fires, as they provide data entry for both narrow and large areas, which can be repeated in a short time.

Airborne remote sensing is another method used in the detection of coal fires. The first use of these techniques took place in the United States around the 1960s [35]. The way that airborne remote sensing works is by using photographs to find things like coal fires.

In the 1980s, with developing technology, coal fires began to be detected using space-based remote sensing [36]. The advantages of this method are many and they can be sorted as follows: detecting the coal fires using multi-spectral and multi-temporal data is eligible, it gives opportunity to detect and monitor larger areas, and relatively more affordable. This study is focused on the space-based remote sensing techniques. In this study, satellite data is used as primary data to detect coal fires.

Several types of image-based data have been used to locate and monitor coal fires in coal mines. A few examples of these types of data and their resolution qualities can be given as follows:

- low spatial resolution satellite images: the Advanced Very High Resolution Radiometer (AVHRR) and the Moderate Resolution Imaging Spectroradiometer (MODIS),
- higher spatial resolution satellite images: Landsat TM, Landsat ETM+, Landsat 8 OLI/TIRS (Operational Land Imager/Thermal Infrared Sensor) and the Advanced Spaceborne Thermal Emission and Reflection Radiometer (ASTER),
- high spatial resolution satellite images: the experimental Bi-spectral Infrared Detection (BIRD).

There are many studies on coal fires detection and analysis. Mishra et al. [37] used a threshold technique to extract the thermal anomalies in Jharia Coalfield to detect and analyze coal fires. The Landsat data were used to estimate temperatures of coal fires by comparing them to threshold temperatures that were found by using an iterative method to separate coal fire areas from other areas. They indicated that the most coal fire-affected areas lied in proximity to mapped fault zones; spatial distribution and extent of fire changed over time. Xue et al. [38] used an exclusion method and a multiple-factor analysis method involving land surface temperature (LST), burnt rocks and land use and land cover (LULC), for the purpose of detecting spontaneous combustion of coal. This combined method was applied to identify distribution of coal fire areas by using spatial overlay analysis in the ArcGIS program. Biswal and Gorai [39] indicated that the implementation of threshold temperature resulting from the sampling of radiant temperature data helped to detect the high-temperature fire zones indicative of coal fire pixels over the Jharia coalfield. Mishra et al. [40] used Landsat 7 ETM+ thermal band (band 6) data to derive the coal fire map and classify it into surface and subsurface fires. They indicated that the temperatures obtained with satellite images gave a scaled temperature variation as compared to the results obtained by thermal image cameras, indicating the surface and subsurface coal fires.

Trinh and Zablotskii [41] used multi-temporal Landsat TM, ETM+ and Landsat 8 thermal band data which were captured between 2007 and 2014. The spectral radiance and the brightness temperature were calculated. The emissivity of surface was determined to retrieve the land surface temperature (LST) by using normalized

difference vegetation index (NDVI) method which was developed by Valor and Caselles [42,43]. Gangopadhyay et al. [44] stated that the Landsat 5 TM thermal band (band 6) data could clearly reveal the investigated surface temperature anomalies which were developed because of coal fires. However, due to the lack of very high resolution of the Landsat 5 TM satellite image data, some high temperature areas not formed by coal fires may also be included in coal fires areas. The use of NDVI-induced emissivity can provide a more accurate and reliable land surface temperature (LST) calculation for all land cover types, given the effects of plant species, leaf water content, and viewing angle. Huo et al. [45] used Landsat TM and Landsat ETM+ thermal band (band 6) data to detect coal fires. According to the researchers, the pixel aggregated temperatures of surface coal fires sometimes do not reach the saturation temperature of the Landsat thermal channel (approximately 70 °C) and this situation causes difficulties on the subject of surface coal fires detection. Cracknell and Mansor [46] determined the sub-surface high temperature sources in Jharia coalfields by using medium resolution Landsat 5 TM data. The Landsat 5 TM thermal band (band 6) was used to find out where and how strong thermal anomalies were caused by coal fires in coal mines.

Jiang et al. [47] reclaimed that remote sensing was a practical method for monitoring and studying areas of surface coal fires and coal fires that are very close to the surface. They also added that the geophysical exploration methods were the best choose for detecting deep and hidden coal fire areas. Mishra et al. [37] stated that China and India have studied coal fires with the application of airborne multispectral remote sensing methods since the 1980s. In addition, daytime airborne thermal infrared (TIR) and multispectral data were used to detect and map coal fires from the Jharia coalfield in India between 1984 and 1987 [48-51]. In airborne thermal remote sensing, the content of the data collected for the detection of coal fires is very valuable because it is not dependent on time, height and temperature. Therefore, the optimal image can be obtained with the highly distinguished areas of coal fire and other features and can be used to identify small coal fire ares. Besides, it has high spatial resolution due to positive effects of independence of flying height. Prakash et al. [52] used the Landsat 5 TM thermal band (band 6) night-time data to detect surface and subsurface fires in Jharia coal mines of India. Prasun et al. [53] analyzed Landsat 5 TM thermal band (band 6) data for retrieval of land surface temperature (LST) along with the normalized



difference vegetation index (NDVI) to identify coal fires in the Raniganj coalbelt, India. Chen et al. [54] processed multi-temporal thermal infrared data, high spatial resolution remote sensing data, and field measurements to detect coal mine fire areas in the Inner Mongolia Autonomous region in northern China.

## 1.5 Objectives of The Thesis

An important part of Turkey's coal reserves are located in Manisa's Soma district. The objectives of this thesis are given as follows:

- to detect and monitor the areas of coal fires using multi-temporal Landsat 5 TM thermal band (band 6) data and Landsat 8 OLI/TIRS thermal band (band 10 and band 11) data;
- to obtain land surface emissivity (LSE) from normalized difference vegetation index (NDVI);
- to get information about land surface temperature (LST) of the study area;
- to obtain temporal thermal maps of the coal fire areas in yearly intervals;
- to investigate accuracy of Landsat 5 TM and Landsat 8 OLI/TIRS satellite data for identifying locations of coal fire areas.

# Chapter 2

## MATERIALS AND METHODS

The main purpose of this study is to detect and monitor coal fires that occur in the coal mine areas in Soma district of Manisa province. These fires threaten both the environment and daily life by causing drastic changes on the land surface. Thus, as a result of the effective use of remote sensing materials (spaceborne remote sensing products such as multitemporal Landsat 5 TM and Landsat 8 OLI/TIRS satellite data) and data processing programs (ERDAS Imagine, ArcGIS and, Google Earth), the land surface temperatures (LST) of the study area will be retrieved and the locations of thermal anomalies will be determined. Finally, the coal fires in Soma coal mine areas will be revealed. In addition, accuracies of the study results will be validated by applying a number of methods. The study consists of three stages:

- Data acquisition
- Data preprocessing
- Data processing

### 2.1 Study Area

#### 2.1.1 Geographic Location of Soma

The study area is covered the region within the borders of Soma district of Manisa province. Soma is located in the north of the Aegean Region. Kırkağaç is in the east, Bergama in the west, Savaştepe (Balıkesir) and İvrindi in the north and Palamut subdistrict in the south of Soma. Soma, located in the northwest of the province, neighbors Kırkağaç in the east, Kınık and Bergama districts of İzmir in the west, Savaştepe and İvrindi districts of Balıkesir in the north and Akhisar in the south. Soma

is in the North Aegean Region, on the Akhisar-Bergama highway and on the Ankara-İzmir railway. The district was established in Bakırçay valley, which is 160 meters above sea level. Soma is between 27.37 east longitude and 39.11 north latitude (39°11'N 27°37'E). The district has an average altitude of 175 meters and an area of about 826 km<sup>2</sup>. In Figure 2.1, geographic map of Soma is presented.

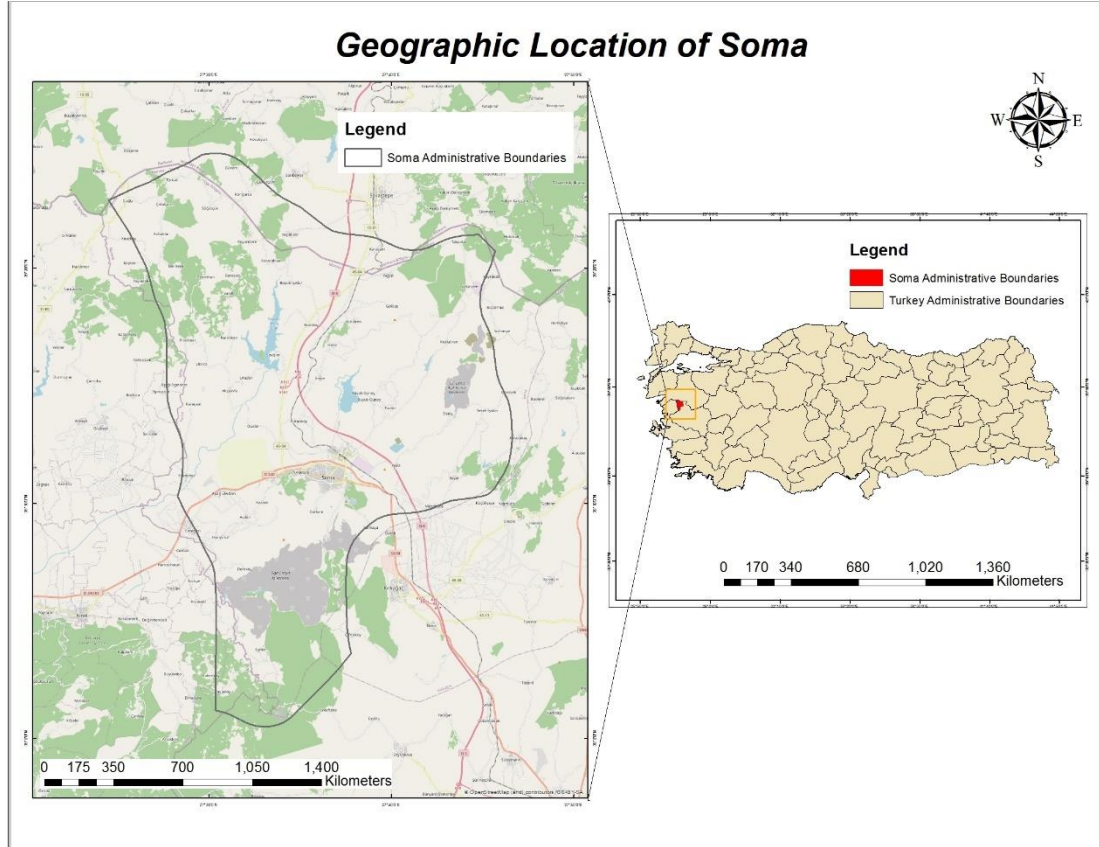


Figure 2.1: Geographic Location of Soma

More than half of Soma's land structure is mountainous. The district is covered with dense, steep hills and high mountains to the south. In the east of Soma, there are high mountains, a few plateaus and some ridges suitable for settlement over time. There is Bakırçay in the west of Soma. With the effect of the streams fed by Bakırçay and the branches of these streams, the lands were divided, valleys and plains were formed at several points. The district is surrounded by mountains from the south, east, north and north east. The main plain of the district is Bakırçay plain, which is one of the numbered plains of the Aegean Region. This plain is located between Marda Mountain and Yunt Mountain. The most productive area of the district is Bakırçay plain. There are many large and small valleys in the district. The valleys with Maden and Sarıkaya creeks and Türkali Kovuk Creek can be given as examples of these valleys.

Characteristic Inner Aegean climate is observed in the basin. Summers are hot and dry, winters are cold and rainy. The temperature ranges from 25°C to 35 °C in summer and from -3°C to 10°C in winter. It is rainy in spring and autumn. It snows from time to time during the winter months. Soma is included in the Semi-humid Mediterranean climate zone. In this region, the winter season is the rainy season with an increase of frontal rain and the summer is the least rainy season. The warmest month is July. The average temperature of the region is around 23°C-24°C, and the temperature is low because it is frequently exposed to cold air currents from the Balkans in winter. The coldest month is January and has an average temperature of 3°C-5°C. Snowfalls are normal and frequent frost events are encountered in the region. A mediterranean climate effect is seen on flora. High places are usually covered with pine forests. There are cultivated and planted agricultural areas in low places and plains.

### 2.1.2 Geological Structure of Soma

The bedrock of the Soma Basin consists of paleozoic graywacke and mesozoic crystallized limestones. Neogene deposits overlie the foundation in a disharmonic way. These deposits are myocene basement series (M1), marl series (M2), limestone series (M3) and pliocene aged sandstone, mottled clay (P1) and marl-tuff (P2) series. Coal horizon has been formed in three layers. These layers are called main layer (KM1-2), middle layer (KM3) and upper layer (KP1).

The thickness of the M1 layer is between 50-200 meters. The thickness of the M2 layer is 100 meters and the thickness of the M3 layer is 50-60 meters. The thickness of the P1 layer is between 120-150 meters, the thickness of the P2 layer is 300-500 meters. The thickness of the KM2 layer varies between 15-22 meters. The thickness of the KM3 layers is between 6-10 meters. In addition, the thickness of the KP1 layer is around 7-8 meters.

- Main layer; M1 is among the M2 formations. It is the most important coal layer of the basin. It has an average thickness of 20 meters and contains exploitable coal. It has a black bright color, conchoidal diffraction and a hard structure. The analysis values of coal can be specified as 12-14% water (humidity), 26-28% ash, and 0.8-0.9% Sulphur (S). According to its location and level, the lower heating value ranges between approximately 3500-4500 K.Cal/Kg.

- The middle layer was formed in the upper levels of the M3 formation. It is not fertile because it has plenty of interruptions and is not continuous. It is partially produced in open pits.
- The upper layer is located between the P1-P2 formations of the pliocene. It is rich in clay and low in calories. It is produced for thermal power plant in Deniz. The analysis values of the coal were measured as 20-25% water (humidity) 45-50% ash. The lower heating value ranges between approximately 3500-4500 K.Cal/Kg. In Figure 2.2, geological structure of Soma is given in sections.

System	Series	Formation	Thickness (m)	Rock Type	EXPLANATION	Symbol
Quaternary	Holocene				Alluvium	Qal/Ym
	Pleistocene				Nodular Limestone	?
					Young Coaly level	
					Sandstone Gravel Erosion	Pltv
			Tuff Agglomera			
NEOGENE	Pliocene	Deniz Formation	200-300		Cherty Limestone	P3
			300-500		Tuff - Marl series	P2ab/P2c
			7-8		Upper Coal Layer	KP1
			120-150		Clay - sand series	P1
					Limestone	?
					Middle coal series	KM3
	Miocene	Soma Formation	50-60		Limestone series	M3
			100		Marl series	M2
			15-22		Lover coal series	KM2
			50-200		Coaly claystone Sandstone Conglomerate	M1
					Paleozoic Mesozoic Limestone	
			Basement Formation			

Figure 2.2: General Stratigraphic Sections for The Soma Coal Basin [55]

### 2.1.3 Coal Mining In Soma

Soma is a town made famous for coal mining in Turkey. The basis of the district's economy is lignite management and the developed sectors depend on this management. In the district, electrical energy is obtained from coal and coal takes the first place in the district's economy. Lignite coal mining were started in Soma with the discovery of coal in 1913. There are Aegean Lignite Enterprise Regional Directorate (Ege Linyit İşletmeleri Genel Müdürlüğü) and TEAŞ (Türkiye Elektrik Üretim Şirketi) power plants in the district. Soma Thermal Power Plant (SEAS) (Soma Termik Santrali) meets the electricity needs of West and Northwest Anatolia from the shortest distance, thereby ensuring economic and social development in the region. There are not many agricultural areas due to the coal basins in Soma.

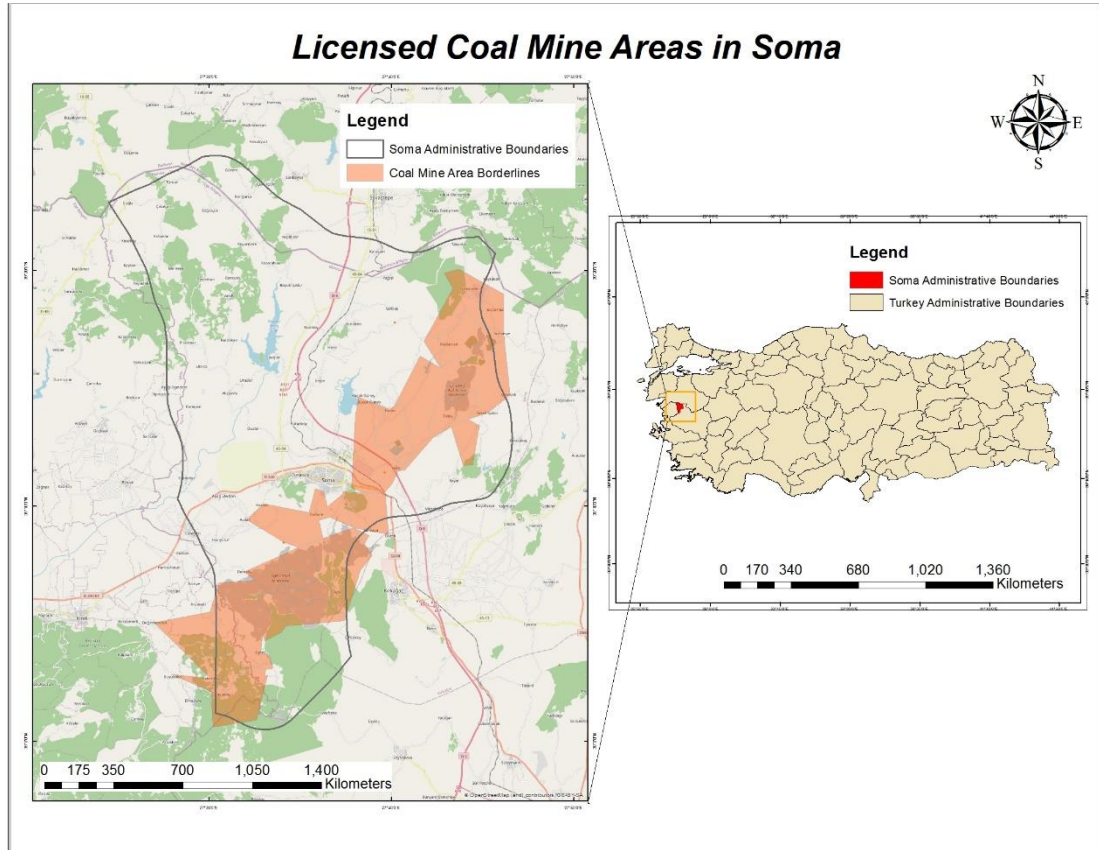


Figure 2.3: Licensed Coal Mine Areas in Soma

The licensed coal mine areas can be listed as follows:

- Deniř: Open-pit mining activities are ongoing.
- Sarıkaya: In this field where open pit mining is carried out, underground management is also carried out with royalty method.
- Iřıklar: In this field where open pit mining is carried out, underground management is also carried out with royalty method.
- Darkale: The underground management studies with royalty method were terminated in 2013. There is no mining activity.
- Eynez: Open pit mining and underground mining operations are carried out with royalty method.
- Delimamlar: Underground management has been done with royalty method. Studies in this field have been terminated. There is no mining activity.

In Figure 2.4-2.8, a number of photographs of Soma coal mine areas are presented [56].

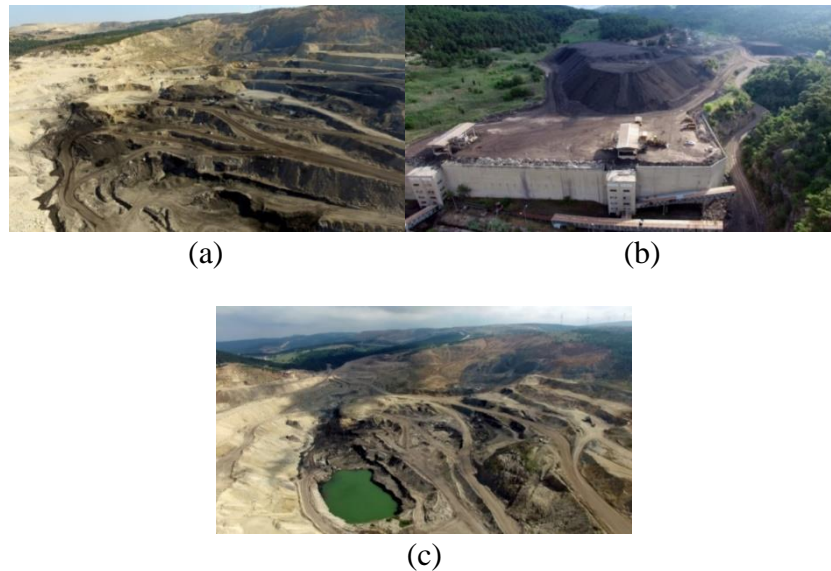


Figure 2.4: (a) Deniř Bunker Area, (b) Deniř Open Pit Mining Area 1, (c) Deniř Open Pit Mining Area 2



Figure 2.5: (a) Soma Sarıkaya Telsiz Open Pit Mining Area 1, (b) Soma Sarıkaya Telsiz Open Pit Mining Area 2

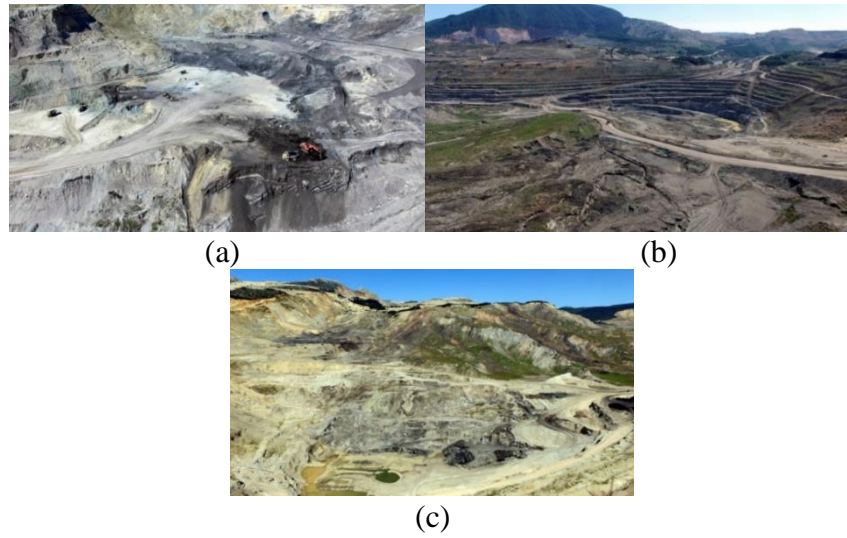


Figure 2.6: Soma Kısırkdere Işıklar Open Pit Mining Management, Soma Kısırkdere Işıklar Open Pit Mining Area 1, Soma Kısırkdere Işıklar Open Pit Mining Area 2



Figure 2.7: (a) Soma Eynez Open Pit Mining Area 1, (b) Soma Eynez Open Pit Mining Area 2, (c) Soma Eynez Open Pit Mining Area 3, (d) Soma Eynez Open Pit Mining Area 4



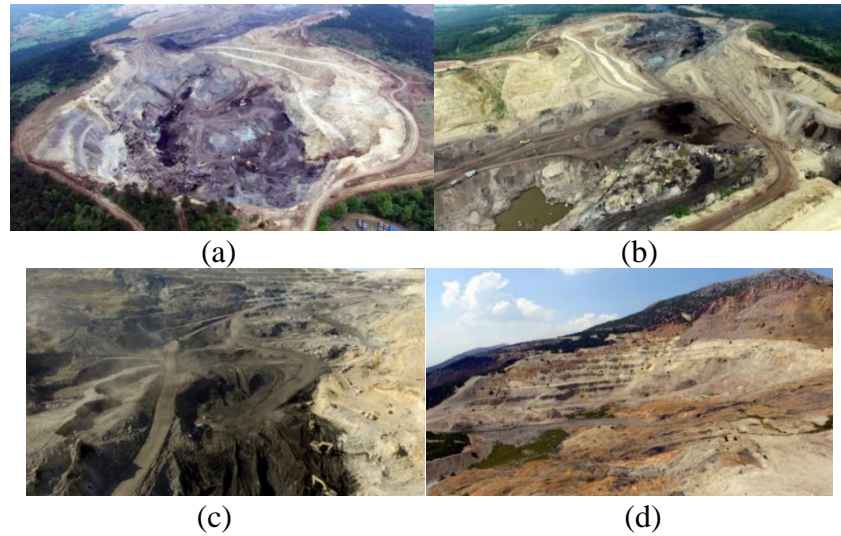


Figure 2.8: (a) Deniz Dedetaşı C Panel Open Pit Mining Area 1, (b) Deniz Dedetaşı C Panel Open Pit Mining Area 2, (c) Deniz Dedetaşı C Panel Open Pit Mining Area 3, (d) Soma Elmalı Mining Area

## 2.2 DATA

Thanks to remote sensing technology through sensors on the satellites, it has been possible to quickly and effectively map the dangers caused by a host of abnormally high temperatures such as coal fires, forest fires, oil well fires and volcanic eruptions. Various satellite images can be obtained for mapping processes of these events by using such as Landsat 4-5 TM, Landsat 7 ETM+, ASTER and MODIS satellite data without being on the event sites, which is generally extremely dangerous.

The datasets used in this study were downloaded from the United States Geological Survey (USGS) website. The USGS website is a data resource website that provides free spatial data for remote sensing and similar scientific disciplines. In this study, Landsat 5 TM and Landsat 8 OLI/TIRS satellite images were used as primary data. Additionally, a map that gives information about the locations of coal mines and the institutions and organizations operating these mines is an important resource that can be looked at in the detection of coal fires that occur in coal mines. The data collected for this study given as follows:

- Landsat 5 TM Satellite Data
- Landsat 8 OLI/TIRS Satellite Data

- Spatial Distribution Map of Coal Mines in Soma Region as ancillary data in Portable Document Format (PDF) and Keyhole Markup Language (KMZ) format

## 2.2.1 Landsat 5 TM

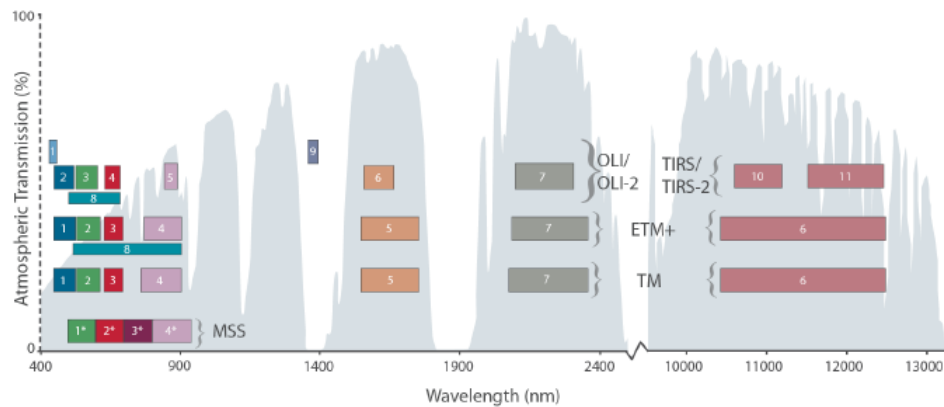


Figure 2.9: Spectral Bands and Wavelengths of the Landsat 5 TM Satellite Sensor  
 Landsat sensors, spectral channels and band-passes, superimposed on atmospheric transmission percentage (grey background). MSS: Landsat-1 through -5; TM: Landsat-4 and -5; ETM+: Landsat-7; OLI and TIRS: Landsat-8 [57]

Landsat 5 TM satellite images are collected via the sensors on the Landsat 5 TM satellite, taking advantage of the technological privileges offered by remote sensing science. As it is seen Figure 2.9, Landsat 5 TM satellite images consist of six spectral reflection bands in total, respectively:

- Band 1: 0.45  $\mu\text{m}$  – 0.52  $\mu\text{m}$ ,
- Band 2: 0.52  $\mu\text{m}$  – 0.60  $\mu\text{m}$ ,
- Band 3: 0.63  $\mu\text{m}$  – 0.69  $\mu\text{m}$ ,
- Band 4: 0.76  $\mu\text{m}$  – 0.90  $\mu\text{m}$ ,
- Band 5: 1.55  $\mu\text{m}$  – 1.75  $\mu\text{m}$ , and
- Band 7: 2.08  $\mu\text{m}$  – 2.35  $\mu\text{m}$ .

They also contain a thermal infrared (TIR) band (band 6): 10.40  $\mu\text{m}$  – 12.50  $\mu\text{m}$  with a spatial resolution of 120 meters. Nevertheless, all the Landsat 5 TM products are resampled to 30 meters resolution.

In most of wild fire studies on land surface, mostly SWIR (Shortwave Infrared) bands (band 5 and band 7) and TIR band (Band 6) data have been used as the main source for retrieving land surface temperature (LST) information [48,50,51,58,59,60,62]. As additional information, Landsat 5 TM sensors, which detect band 6 (10.40  $\mu\text{m}$  – 12.50  $\mu\text{m}$ ) and Band 7 (2.08  $\mu\text{m}$  – 2.35  $\mu\text{m}$ ) wavelengths, can be particularly useful when working on areas where the possibility of fire is suspected.

It can be said that the surface temperature above underground coal fires is less high due to the relatively low thermal conductivity of materials such as sandstone, shale, coal [52], which are frequently encountered in the coal mine area, compared to other materials in nature. Even if this is the fact, these low temperature values can easily be determined with thermal band (band 6) of Landsat 5 TM [60].

For the measurements of higher temperature surface fires, especially if fires caused by volcanic eruptions in volcanic terrains are investigated, SWIR bands should be preferred because thermal band (band 6) is not very good at sensing temperatures above 68.00°C [63-68].

The time interval of captured satellite images for the detection and mapping of coal fire areas is usually between 9.30 antimeridian (AM) and 10.30 antimeridian (AM) and were detected by sensors during daytime. In some studies, Landsat 5 TM thermal band (band 6) data which are detected at night have also been included in the detection of coal fires that continue to burn [69,17]. The presence of abnormally high temperature in an area without coal fire in the process of detecting land surface temperature (LST) with the effects of reflected sunlight in daytime satellite images may lead to deceptive results. Satellite images which are captured by sensors at night, on the other hand, provide an accurate detection of the radiation emitted by still burning coal fires, as they are independent of sunlight effects.

This satellite was taken out of service in January 2013. The Landsat Enhanced Thematic Mapper Plus (ETM+) was launched on LANDSAT 7 as next LANDSAT mission's satellite at 1999 after 15 years of LANDSAT 5 launch and the satellite data

collection has been being continued since 2013 with this satellite and even with LANDSAT 8.

It has been acknowledged that Landsat TM thermal band (band 6) have been used in many studies to detect the traces of coal fires. The spatial resolution of the Landsat TM (band 6) data is 120 meters, and this resolution was believed to be difficult to detect small-scale coal fires in the depths of the ground [28]. Nevertheless, Landsat 6 TM data makes it easy to research large, sloping and rocky (hard to reach) areas where fieldwork is often subtle and monitor burning rocks, sparse vegetation, vents, and fissures in coal mine areas [44].

### 2.2.2 Landsat 8 OLI/TIRS

The Landsat 8 OLI/TIRS satellite is also called as Landsat Data Continuity Mission (LDCM). The basic difference of Landsat 8 OLI/TIRS from Landsat 5 TM and Landsat 7 ETM+ is that Landsat 8 OLI/TIRS contains two thermal infrared bands (TIR) between 10  $\mu\text{m}$  and 12  $\mu\text{m}$ . Landsat 8 OLI and TIRS satellite have eleven spectral bands and the data capture process takes place through these spectral bands which are given as follows:

- Band 1: 0.43  $\mu\text{m}$  – 0.45  $\mu\text{m}$
- Band 2: 0.45  $\mu\text{m}$  – 0.51  $\mu\text{m}$
- Band 3: 0.53  $\mu\text{m}$  – 0.59  $\mu\text{m}$
- Band 4: 0.64  $\mu\text{m}$  – 0.67  $\mu\text{m}$
- Band 5: 0.85  $\mu\text{m}$  – 0.88  $\mu\text{m}$
- Band 6: 1.57  $\mu\text{m}$  – 1.65  $\mu\text{m}$
- Band 7: 2.11  $\mu\text{m}$  – 2.29  $\mu\text{m}$
- Band 8: 0.50  $\mu\text{m}$  – 0.68  $\mu\text{m}$
- Band 9: 1.36  $\mu\text{m}$  – 1.38  $\mu\text{m}$

- Band 10: 10.60  $\mu\text{m}$  – 11.19  $\mu\text{m}$
- Band 11: 11.50  $\mu\text{m}$  – 12.51  $\mu\text{m}$

The spatial resolutions of band 1, 2, 3, 4, 5, 6, 7 and 9 are 30 meters, the spatial resolution of band 8 is 15 meters. In addition, Landsat 8 satellite incorporates a thermal sensor other than Operational Land Imager (OLI) that is called Thermal Infrared Sensor (TIRS). The TIRS thermal sensor consists of two thermal bands: Band 10 (10.60  $\mu\text{m}$  – 11.19  $\mu\text{m}$ ) and Band 11 (11.50  $\mu\text{m}$  – 12.51  $\mu\text{m}$ ). In fact, TIRS thermal band images are stored in sensors with 100 meters of spatial resolution information, but images resampled to 30 meters are included in the data processing part.

Table 2.1: Characteristics of Landsat 8 Satellite Bands (This table is prepared with the contributions of the earth observing system website.) [70]

Sensor Type	Band name	Band number	Wavelength ( $\mu\text{m}$ )	Resolution (m)	Band Applications
OLI	Coastal	1	0.43 - 0.45	30	Coastal and aerosol studies
OLI	Blue	2	0.45 - 0.51	30	Bathymetric mapping, distinguishing soil from vegetation, and deciduous from coniferous vegetation
OLI	Green	3	0.53 - 0.59	30	Emphasizes peak vegetation, which is useful for assessing plant vigor
OLI	Red	4	0.63 - 0.67	30	Discriminates vegetation slopes
OLI	NIR	5	0.85 - 0.88	30	Emphasizes biomass content and shorelines
OLI	SWIR 1	6	1.57 - 1.65	30	Discriminates moisture content of soil and vegetation; penetrates thin clouds
OLI	SWIR 2	7	2.11 - 2.29	30	Improved ability to track moisture content of soil and vegetation and thin cloud penetration
OLI	Pan	8	0.50 - 0.68	15	15 meter resolution, sharper image definition
OLI	Cirrus	9	1.36 - 1.38	30	Improved detection of cirrus cloud contamination
TIRS	TIRS 1	10	10.60 - 11.19	30 (100)	100 meter resolution, thermal mapping and estimated soil moisture
TIRS	TIRS 2	11	11.50 - 12.51	30 (100)	100 meter resolution, thermal mapping and estimated soil moisture

Thermal bands (TIR) data have proven themselves in obtaining highly accurate land surface temperature data (LST) with approximate scene size 170000 m north-south and 183000 m east-west. Additionally, SWIR 1 band (band 7) data is a powerful alternative to interpret high temperature objects by making temperature estimates [71]. The usage areas of Landsat 8 OLI/TIRS satellite data include land surface temperature (LST) detection, which requires band 10 and/or band 11 thermal band data [72]. Landsat 8 OLI/TIRS satellite still actively continues to provide remote sensing data.

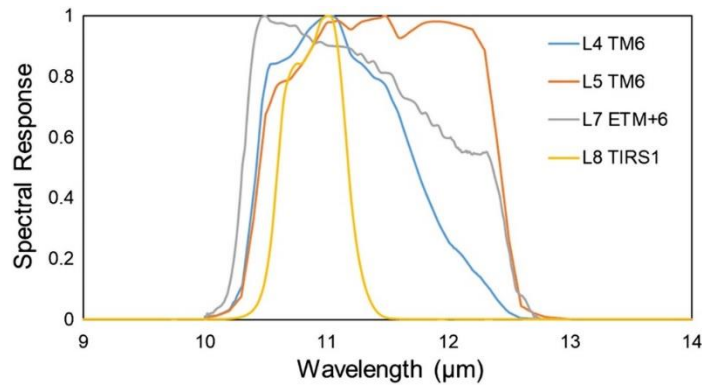


Figure 2.10: Spectral response for Landsat 4 TM6, Landsat 5 TM6, Landsat 7 ETM+ 6, and Landsat 8 TIRS1 [73]

The effective wavelengths are 11.154 μm for Landsat 4 TM6, 11.457 μm for Landsat 5 TM6, 11.269 μm for Landsat 7 ETM+ 6, and 10.904 μm for Landsat 8 TIRS1, respectively given in Figure 2.10.

## 2.3 Remote Sensing Techniques For Coal Fire Detection

Remote sensing techniques began to be used in the United States in the 1960s for the first time in history, and coal fires in coal mines were first studied during those dates with these techniques. These studies were conducted by Greene et al. [74]. Since the thermal anomalies on the surface were quite enormous, they were easily detected by thermal infrared satellite images. By 1972, Ellyett and Fleming revealed the coal fires that took place in the coal mine in Australia with the help of an optical-mechanical sensor that detects the infrared wavelength [75]. Since the 1980s, the use of airborne and spaceborne sensors has increased, and the detection of coal fires by applying remote sensing techniques has become widespread in coal producing countries such as China and India. In recent years, researchers have achieved results successfully in

studies using Landsat 5 TM, Landsat 7 ETM+, Landsat 8 OLI/TIRS, ASTER, MODIS, and similar satellite sensors to detect hot spots, surface and underground coal fires at abnormally high temperatures.

Electromagnetic energy is measured by means of airborne or spaceborne systems. The measured electromagnetic energy allows to define and classify land surface properties. Thus, the properties of the objects on the land surface that radiate and reflect electromagnetic energy are obtained and the information about these objects can be examined. Coal fires, which are actively continuing, cause many changes in the land where they are located and the surrounding areas [76]:

- the increase of temperature,
- emission of smoking,
- changes in colour of caprocks,
- formation and deposition of new materials on the surface,
- land cracking and subsidence at the surface.

The characteristics of the changes can be identified by satellite remote sensing data and the thermal anomalies can be analyzed using satellite thermal infrared images. In the optical satellite image method, some situations that address the effects of coal fires can be given as rock assemblies that have been scorched by coal fires have a different reflection pattern (and spectral signature) compared to their natural state, and thus their detection can be made. Besides, fog, smoke and sulfur dioxide clouds with high density can be noticed in places where coal fires are occurred.

The most important indication of coal fires in the matter of coal fire detection is the presence of abnormally high temperatures. The combustion heat of coal has the essential effect on the emergence of these thermal anomalies. The thermal anomalies provide answers to questions about the extent of the coal fire area, the intensity of the coal fire and the amount of coal loss. The thermal anomalies can be sensed by thermal infrared sensors of airborne/spaceborne platforms.

Waste materials in coal mines contain sufficient amount of coal and can react chemically with oxygen upon contact with air [17]. High heat transfer occurs due to heat conduction in untouched sections of coal seams and thermal anomalies ensue. Therefore, coal fires have the opportunity to spread over wider areas. The detection and monitoring of coal fires can be practised by a number of satellite sensors but it depends on several parameters:

- the size of coal fire areas,
- the spatial resolution of the satellite imagery,
- the depth of coal fires,
- the amount of difference between the temperature anomalies in the area of coal fires,
- the temperature in the surrounding background,
- the time of the satellite data acquisition (day, night, seasonal), and
- weather conditions of the coal fire areas, etc.

### 2.3.1 Optical Satellite Data

Information about the surface of the Earth can be determined according to the spectral features, and it can be mapped by examining the Earth's surface. If enough information about spectral features of the Earth's surface is mastered, acquired remote sensing data can be used accurately and effectively. For this reason, it is necessary to understand the spectral features of the Earth's surface and to know which factors affect these features.

Spectral responses, also named as spectral signatures, are measured by sensors depending on numerous attributes and provide an understanding of the states of the object properties, for instance, land surface temperatures (LST). Grasping the nature of the land with remote sensing satellite data is essential both to reduce spectral variability as much as possible and to increase this spectral variability when required for certain cases [77] such as coal fire detection.



Temporal and spatial effects are important elements that contribute to the process of analyzing remote sensing data. Temporal effects occur when the spectral features of an object change depending on the time factor. Enlightening results can be found in coal fires according to temporal effects. For example, thermal anomalies caused by coal fires in coal mines may not be the same condition at different periods of time. Those changes will be reflected on the spectral features of the land surface of the coal fire area.

Generally, when collecting data for coal fires in coal mines, care is taken to have satellite images obtained at night and/or during the winter, as thermal anomalies caused by coal fires are more pronounced at those times and this situation facilitates the detection of coal mine fires. The most suitable time interval for thermal temperature analysis is actually before dawn in the winter season since the effects of the Sun are more passive, the areas where coal fires are experienced are determined more accurately.

One of the data types used in the detection of coal fires by pointing changes in the land surface is satellite optical data. This change determination can be made indirectly or directly, and the changes that have happened can be listed as follows:

- the color changes of the caprocks,
- the changes in terrain and relief,
- the subsidences,
- the cracks,
- the fogs and smokes,
- sulphur dioxide gas, etc.

### 2.3.2 Thermal Satellite Data

In the electromagnetic spectrum, the range between 3  $\mu\text{m}$  and 60  $\mu\text{m}$  has been determined as thermal infrared region. The range from 3  $\mu\text{m}$  to 5  $\mu\text{m}$  and from 8  $\mu\text{m}$  to 12  $\mu\text{m}$  spectrum values are mostly studied regions in remote sensing satellite data

researches. The remote sensing of object features by using thermal infrared is based on the principle that every matter above absolute zero, which is  $-273$ , emits radiation in the thermal infrared region of the electromagnetic spectrum [78].

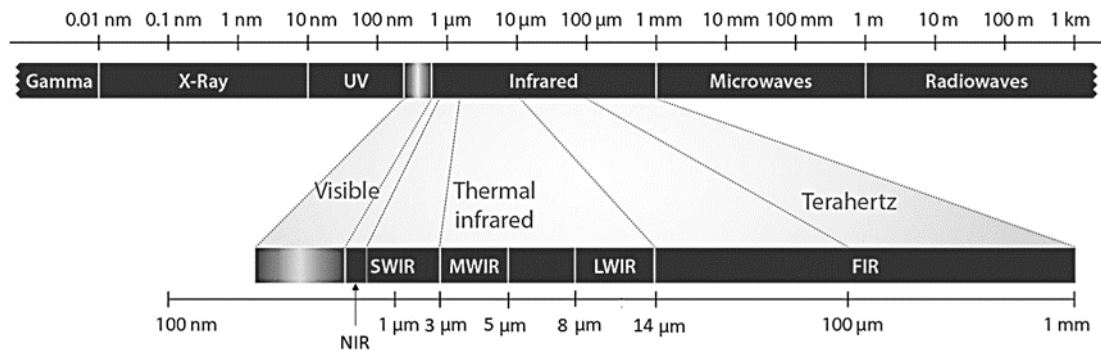


Figure 2.11: The Electromagnetic Spectrum [78]

The interaction of an object with thermal infrared rays differs according to the properties of the surface of that object. These properties are the emissivity, geometry and temperature of the object. There are several satellite systems with thermal infrared sensors are summarized as follows:

- NOAA with an Advanced Very High Resolution Radiometer (AVHRR): It has spectral bands in the thermal infrared region and these are channel 3 ( $3.55 \mu\text{m}$  -  $3.93 \mu\text{m}$ ), channel 4 ( $10.3 \mu\text{m}$  -  $11.3 \mu\text{m}$ ), and channel 5 ( $11.5 \mu\text{m}$  -  $12.5 \mu\text{m}$ ) on NOAA-7,9,11,12 & 14. The spatial resolution is 1.1 km at the lowest level. It varies to almost 8 km at the image border.
- The ATSR (Along Track Scanning Radiometer) sensor on board the ESA ERS-1 satellite: It has a spatial resolution of  $\approx 1$  km.
- The is EOS with the Advanced Spaceborne Thermal Emission and Reflectance Radiometer (ASTER): It was launched in 1999. It senses the region of  $8 \mu\text{m}$  and  $12 \mu\text{m}$  with its five thermal infrared bands at 90 m resolution.
- The Landsat 5 TM: It was launched on March 1, 1984. The  $10.4 \mu\text{m}$  -  $12.5 \mu\text{m}$  region of the electromagnetic spectrum is sensed by band 6 (thermal band) with the spatial resolution of 120 m.

- The Landsat 7 ETM+: It was launched on April 15, 1999. The band 6 Low and High gain (thermal band) senses the region between 10.40  $\mu\text{m}$  and 12.50  $\mu\text{m}$  of the electromagnetic spectrum with the spatial resolution of 60 meters.
- The Landsat 8 TIRS: It was launched on February 11, 2013 and has two thermal band 10 and band 11. The band 10 TIRS 1 senses the 10.6 $\mu\text{m}$ -11.19 $\mu\text{m}$  region of the electromagnetic spectrum with the spatial resolution of 100 m. Also, the band 11 TIRS 2 senses the 11.5 $\mu\text{m}$ -12.51 $\mu\text{m}$  region of the electromagnetic spectrum with the spatial resolution of 100 m.

The advantage of the spaceborne remote sensing for coal fire detection is that it is repeatable, cheaper, and provides processing of multi-band and multitemporal satellite data. The disadvantage is that the spatial resolution generally speaking is still very coarse.

Examination of the coal fires may be difficult for a number of reasons. Especially, the size of the coal mine area and the land surface structure can make it difficult to examine. Landsat satellite images make easier to investigate the coal fires due to their good spatial and spectral resolutions and abilities to reach large areas [79,40,33]. It is stated that thermal infrared bands are more successful than optical bands in matter of the coal fire detection [50,80,44].

### 2.3.3 Thermal Infrared Data Used For Detecting Coal Fire Areas

Thermal anomalies are the main symptoms in the detection of coal fires in coal mines, and these anomalies can be detected by analyzing thermal infrared data. The temperature values (extremely high temperatures) different from the underground air temperature normals are accepted as evidence for the presence of thermal anomalies, so the location of underground coal fires can be determined using thermal infrared remote sensing. In order to detect thermal anomalies on the land surface, some factors should be known. These factors can be listed as the resolution of the thermal infrared band images, the size of the area of thermal anomalies, and the difference between temperature anomalies in the area of coal fires and the temperature of the surrounding background [81]. It is recommended to learn some factors such as time of day,

time/date of year, weather conditions, slope directions and current surface types that are effective in determining the land surface temperatures (LST). The land surface temperatures of soils and rocks are low before dawn, at night, between night and morning, and in the early morning hours. Therefore, it is the best time to collect thermal data for analysis. Temporal, spatial and atmospheric factors affect the process of detecting thermal anomalies with thermal infrared images and the accuracy of this process.

# CHAPTER 3

## DATA ACQUISITION AND PREPROCESSING

As mentioned earlier, the data used in this study to investigate coal fires in coal mine areas of Soma region is as follows: Landsat 5 TM and Landsat 8 OLI/TIRS satellite images, coal mine distribution map of Soma region. Additionally, previous studies on the subject of coal fire detection in the literature are investigated in order to obtain sufficient information about the study.

The Landsat 5 TM and Landsat 8 OLI/TIRS satellite images were collected from the USGS website by the author of this thesis. The map of the distribution of coal mines in the Soma region was taken from Ankara Cadastre General Directorate. This map has greatly contributed to the location of the coal mines in Soma and the visual interpretation of the coal mine areas. The Google Earth program was used to view this map in .kmz format to determine the boundaries of coal mine areas of Soma.

In this study, the literature used to examine the fact that the coal that emerges in and around coal mines is spontaneously combusted. This literature information can be found in the references chapter. Erdas Imagine 2014, Arcmap 10.8 and Google Earth programs were used in this study to preprocess, process and analyze data and access the necessary information.

### 3.1 Landsat Data Acquisition

Landsat 5 TM was a satellite that was launched into space on March 1, 1984. The Landsat 5 TM satellite also contained Multispectral Scanner (MSS) and Thematic Mapper (TM) sensor devices. This satellite obtained remote sensing satellite images consisting of six spectral bands with a spatial resolution of 30 meters for bands 1,2,3,4,5 and 7, and one thermal band (band 6). The Landsat 5 TM satellite was used for satellite image data acquisition for a long time and was discontinued on June 5, 2013. The image data download form this site and used in the study is summarized in the Table 3.1 and Table 3.2.

Table 3.1: Qualifications of The Obtained Landsat 5 TM Satellite Data

Sensor	Spectral Bands	Acquisition Time
Landsat 5 TM	1,2,3,4,5,6,7	1985.08.02
Landsat 5 TM	1,2,3,4,5,6,7	1986.09.13
Landsat 5 TM	1,2,3,4,5,6,7	1987.08.08
Landsat 5 TM	1,2,3,4,5,6,7	1988.07.25
Landsat 5 TM	1,2,3,4,5,6,7	1989.08.29
Landsat 5 TM	1,2,3,4,5,6,7	1990.07.31
Landsat 5 TM	1,2,3,4,5,6,7	1991.07.18
Landsat 5 TM	1,2,3,4,5,6,7	1992.09.06
Landsat 5 TM	1,2,3,4,5,6,7	1993.08.24
Landsat 5 TM	1,2,3,4,5,6,7	1994.09.28
Landsat 5 TM	1,2,3,4,5,6,7	1995.07.29
Landsat 5 TM	1,2,3,4,5,6,7	1996.08.16
Landsat 5 TM	1,2,3,4,5,6,7	1997.09.04
Landsat 5 TM	1,2,3,4,5,6,7	1998.08.06
Landsat 5 TM	1,2,3,4,5,6,7	1999.07.24
Landsat 5 TM	1,2,3,4,5,6,7	2000.07.10
Landsat 5 TM	1,2,3,4,5,6,7	2001.07.29
Landsat 5 TM	1,2,3,4,5,6,7	2002.07.16
Landsat 5 TM	1,2,3,4,5,6,7	2003.08.20
Landsat 5 TM	1,2,3,4,5,6,7	2004.09.07
Landsat 5 TM	1,2,3,4,5,6,7	2005.07.08
Landsat 5 TM	1,2,3,4,5,6,7	2006.09.13
Landsat 5 TM	1,2,3,4,5,6,7	2007.08.31
Landsat 5 TM	1,2,3,4,5,6,7	2008.08.01
Landsat 5 TM	1,2,3,4,5,6,7	2009.07.19

Landsat 8 OLI/TIRS (Landsat Data Continuity Mission, LDCM) is a satellite launched on February 11, 2013 and developed as a collaboration between National Aeronautics and Space Administration (NASA) and the US Geological Survey (USGS). Landsat 8 OLI/TIRS has two sensor devices: the Operational Land Imager (OLI) and the Thermal Infrared Sensor (TIRS). These two sensors procure satellite image data acquisition at a spatial resolution of 30 meters (visible, NIR, SWIR) 100 meters (thermal) and 15 meters (panchromatic).

Table 3.2: Qualifications of The Obtained Landsat 8 OLI/TIRS Satellite Data

Sensor	Spectral Bands	Acquisition Time
Landsat 8 OLI/TIRS	1,2,3,4,5,6,7,8,9,10,11	2013.07.21
Landsat 8 OLI/TIRS	1,2,3,4,5,6,7,8,9,10,11	2013.07.30
Landsat 8 OLI/TIRS	1,2,3,4,5,6,7,8,9,10,11	2013.08.15
Landsat 8 OLI/TIRS	1,2,3,4,5,6,7,8,9,10,11	2014.07.08
Landsat 8 OLI/TIRS	1,2,3,4,5,6,7,8,9,10,11	2014.10.21
Landsat 8 OLI/TIRS	1,2,3,4,5,6,7,8,9,10,11	2014.11.06
Landsat 8 OLI/TIRS	1,2,3,4,5,6,7,8,9,10,11	2015.07.20
Landsat 8 OLI/TIRS	1,2,3,4,5,6,7,8,9,10,11	2015.07.27
Landsat 8 OLI/TIRS	1,2,3,4,5,6,7,8,9,10,11	2016.07.13
Landsat 8 OLI/TIRS	1,2,3,4,5,6,7,8,9,10,11	2016.07.22
Landsat 8 OLI/TIRS	1,2,3,4,5,6,7,8,9,10,11	2016.07.29
Landsat 8 OLI/TIRS	1,2,3,4,5,6,7,8,9,10,11	2016.08.07
Landsat 8 OLI/TIRS	1,2,3,4,5,6,7,8,9,10,11	2017.07.09
Landsat 8 OLI/TIRS	1,2,3,4,5,6,7,8,9,10,11	2017.07.25
Landsat 8 OLI/TIRS	1,2,3,4,5,6,7,8,9,10,11	2017.09.02
Landsat 8 OLI/TIRS	1,2,3,4,5,6,7,8,9,10,11	2018.07.03
Landsat 8 OLI/TIRS	1,2,3,4,5,6,7,8,9,10,11	2018.08.13
Landsat 8 OLI/TIRS	1,2,3,4,5,6,7,8,9,10,11	2019.07.06
Landsat 8 OLI/TIRS	1,2,3,4,5,6,7,8,9,10,11	2019.07.31
Landsat 8 OLI/TIRS	1,2,3,4,5,6,7,8,9,10,11	2020.07.01
Landsat 8 OLI/TIRS	1,2,3,4,5,6,7,8,9,10,11	2020.07.17
Landsat 8 OLI/TIRS	1,2,3,4,5,6,7,8,9,10,11	2020.07.24
Landsat 8 OLI/TIRS	1,2,3,4,5,6,7,8,9,10,11	2020.09.03

Remote sensing satellite images were collected as a result of the activities of Landsat 5 TM and Landsat 8 OLI/TIRS satellites. These images are used in this study to calculate values of reflections, brightness temperatures, the normalized difference vegetation indexes (NDVI), land surface emissivity (LSE), and land surface

temperature (LST). Ultimately, they are processed to detect coal fires that occur in coal mines of Soma.

### 3.1.1 Procedure For Downloading Landsat Data

There are many websites that provide the opportunity to download satellite images obtained by remote sensing methods using Landsat satellites. In this study, Landsat 5 TM and Landsat 8 OLI/TIRS satellite data to be used in the data processing phase were obtained freely from the USGS internet address (<https://earthexplorer.usgs.gov/>). In order to download data from this website, it is imperative to be a member of the website.

For this study, 25 Landsat 5 TM satellite data and 23 Landsat 8 OLI/TIRS satellite data were downloaded in total as seen in Table 3.1 and Table 3.2. All downloaded Landsat 5 TM and Landsat 8 OLI/TIRS satellite data are Landsat Collection Level 1 Tiers 1 (L1T1) data products.

## 3.2 Landsat Image Data Preprocessing

The main reason for preprocessing images using various data processing programs is to prepare the images for processing and to make the data manageable. Preprocessing of satellite images to be used in data processing is vital for determining and interpreting land surface features from satellite images. The flowchart of image preprocessing is shown in Figure 3.1. Image preprocessing procedure mainly consists of radiometric correction and subset. The radiometric correction and preprocessing have three parts:

- Conversion of Digital Numbers (DN) to Top of Atmospheric Spectral Radiance ( $L\lambda$ ),
- Conversion of Spectral Radiance ( $L\lambda$ ) to Reflectance ( $\rho$ ) for reflectance bands, and
- Conversion of Spectral Radiance ( $L\lambda$ ) to Brightness Temperature ( $T_{sensor}$ ).



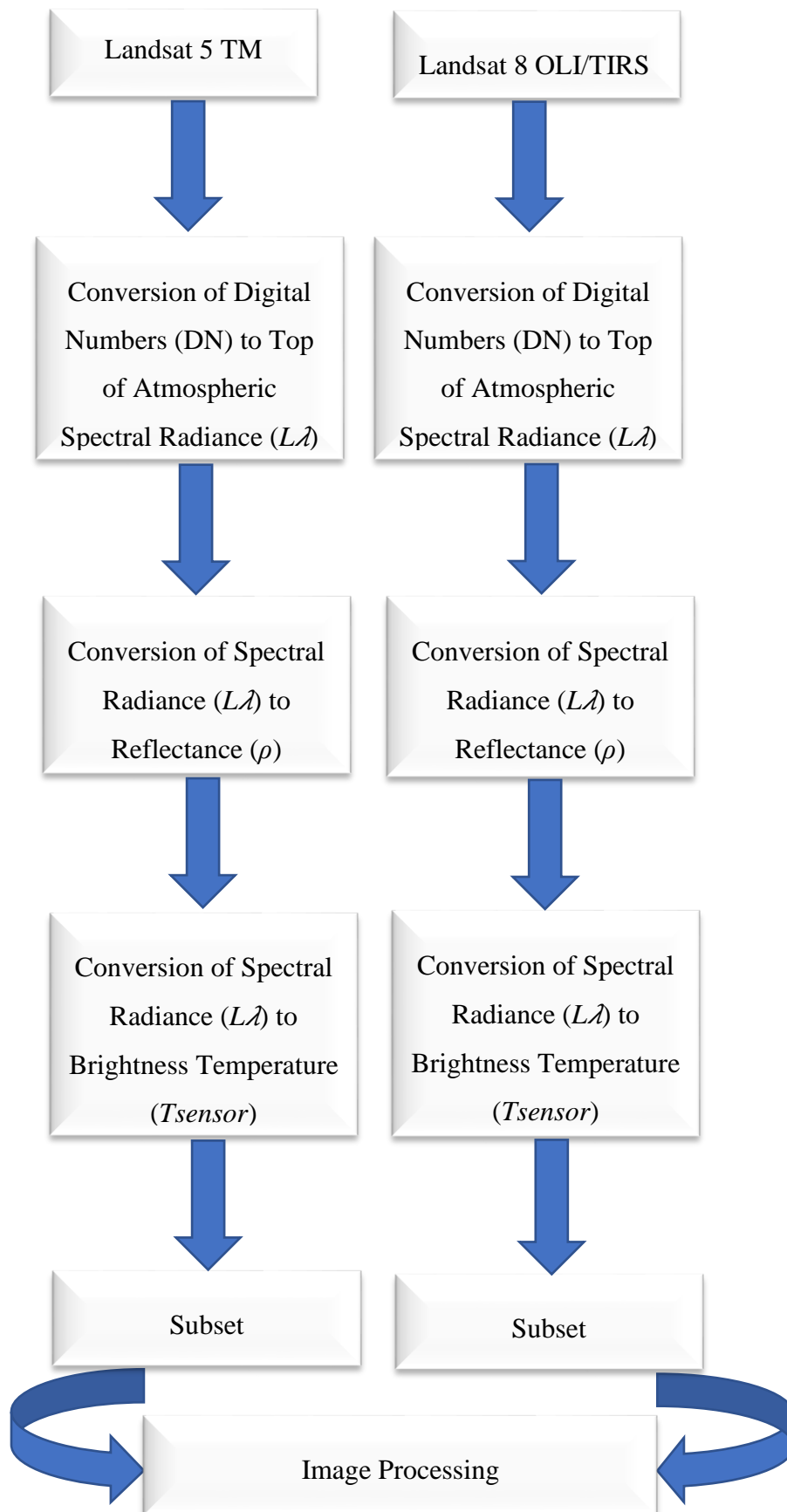


Figure 3.1: Flowchart of Image Preprocessing

### 3.2.1 Geometric Correction

It is very important to record remote sensing satellite images with geometric correction because combining the geometrically corrected remote sensing data with the geographic information system allows the information to be interpreted correctly. Further, before dynamic monitoring using time series remote sensing satellite images, the obtained satellite data should be geometrically corrected. Landsat satellite image data used in this study were collected geometrically corrected. The Landsat 5 TM and the Landsat 8 OLI/TIRS satellite images were georeferenced to the UTM Zone 35N WGS 84 coordinate system.

### 3.2.2 Radiometric Correction

The radiation detected by the radiometers in satellites is measured depending on both surface parameters such as temperature and emission, and atmospheric effects. For this reason, it is difficult to accurately predict the land surface temperature (LST) in its raw form over the thermal band without any processing. As a result, the procedures of radiometric corrections were needed.

The formulas of Conversion of Digital Numbers (DN) to Top of Atmospheric Spectral Radiance ( $L\lambda$ ), Conversion of Spectral Radiance ( $L\lambda$ ) to Reflectance ( $\rho$ ) and Conversion of Spectral Radiance ( $L\lambda$ ) to Brightness Temperature ( $T_{sensor}$ ), which are the steps of radiometric corrections were organized as a single spatial model. Thus, the radiometric corrections of Landsat 5 TM and Landsat 8 OLI/TIRS satellite images were achieved simultaneously. The ERDAS Imagine 2014 data processing program was preferred to apply radiometric corrections.

#### 3.2.2.1 Conversion of Digital Numbers (DN) to Top of Atmospheric Spectral Radiance ( $L\lambda$ )

The remote sensing satellite data are obtained by satellite sensors and stored in Digital Numbers (DN)s. Digital Numbers (DN) are used to represent uncalibrated pixels so that different brightness levels of any raster satellite image can be grouped.

Reflected solar rays are captured by the sensors of the Landsat 5 TM satellite. These solar rays are converted to radiance values and rescaled with 8-bit Digital Numbers (DN) from 0 to 255. Digital Numbers (DNs) can be converted into atmosphere reflectance values (Top of Atmosphere Reflectance) in two steps. The first step is converting the Digital Numbers (DNs) to radiance values and the second step is converting the radiance data to Top of Atmosphere (ToA) Reflectance. The formula of conversion of Digital Numbers (DN) to Top of Atmospheric Spectral Radiance ( $L_\lambda$ ) (Equation 3.1) is given as follows:

$$L_\lambda = \frac{L_{max\lambda} - L_{min\lambda}}{Q_{calmax} - Q_{calmin}} (Q_{cal} - Q_{calmin}) + L_{min\lambda} \quad (3.1)$$

where  $L_\lambda$  is spectral radiance at the sensor's aperture [ $W/(m^2 \cdot sr \cdot \mu m)$ ];  $Q_{cal}$  is quantized calibrated pixel value;  $Q_{calmax}$  is Maximum quantized calibrated pixel value corresponding to  $L_{max\lambda}$ ;  $Q_{calmin}$  is minimum quantized calibrated pixel value corresponding to  $L_{min\lambda}$ ;  $L_{max\lambda}$  is spectral radiance at sensor that is scaled to  $DN_{max}$  [ $W/(m^2 \cdot sr \cdot \mu m)$ ];  $L_{min\lambda}$  is spectral radiance at-sensor that is scaled to  $DN_{min}$  [ $W/(m^2 \cdot sr \cdot \mu m)$ ]. This formula was applied to the bands (from band 1 to band 7) of all Landsat 5 TM satellite image data. The radiance scaling factors were provided in the metadata file of the Landsat 5 TM (10.45  $\mu m$  - 12.42  $\mu m$ ).

The Landsat 8 OLI/TIRS satellite data products consist of quantized and calibrated scaled Digital Numbers (DNs) which represent multispectral images obtained by the Operational Land Imager (OLI) and the Thermal Infrared Sensor (TIRS). These satellite data are collected by the Landsat 8 sensors in 16-bit unsigned integer format and rescaled according to the Top of Atmosphere (ToA) Reflectance. The fact that the Landsat 8 OLI sensor is highly accurate is a significant improvement that allows Landsat 8 OLI/TIRS satellite data to be rescaled from 0 to 65536 with 16-bit Digital Numbers (DNs). It should not be forgotten that the Landsat 8 OLI/TIRS satellite images are processed in units of absolute radiance using 32-bit floating-point calculations. These data were converted to Top of Atmosphere (ToA) Reflectance, instead of radiance, thus Digital Numbers (DNs) can be converted to Reflectance in one step. Accordingly, the Digital Numbers (DNs) were converted to spectral radiance using the following formula (Equation 3.2):

$$L_{\lambda} = M_L \cdot Q_{cal} + A_L \quad (3.2)$$

where  $L_{\lambda}$  is the spectral radiance received by the sensor ( $W \cdot m^{-2} \cdot sr^{-1} \cdot \mu m^{-1}$ ),  $M_L$  represents the band-specific multiplicative rescaling factor from the metadata,  $Q_{cal}$  is the level 1 pixel value in DN (quantized and calibrated standard product pixel values in interger),  $A_L$  is the band-specific additive rescaling factor. This formula was applied to the bands (band 2,3,4,5,6,10,7) of all Landsat 8 OLI/TIRS satellite image data. The radiance scaling factors were provided in the metadata file of the Landsat 8 OLI/TIRS satellite (10.60  $\mu m$  – 11.19  $\mu m$ ) images.

### 3.2.2.2 Conversion of Spectral Radiance ( $L_{\lambda}$ ) to Reflectance ( $\rho_{\lambda}$ )

Each pixel in satellite images is represented by a Digital Number (DN). Digital Numbers (DNs) are required to be converted into the Top of Atmosphere (ToA) Radiance values for the reflectance bands so that the satellite images can be readably interpreted. Another reason for the Top of Atmosphere (ToA) Radiance conversion of Digital Numbers (DNs) is to be able to reduce and correct errors in the numbers of digital images. Thus, the interpretability and quality of remotely sensed satellite data were improved. Also, this situation should be taken into consideration when analyzing and comparing data sets of different time over multiple time periods. Each pixel has only a unique value recorded and these values do not include only the radiation reflected or emitted from the land surface. Moreover, these values include the radiation scattered and emitted by the atmosphere. In many study cases, actual land surface temperature (LST) values are a source for obtaining information about the temperature of the land surface and acting on many conclusions obtained using the information learned. Therefore, the conversion process of Digital Numbers (DNs) to the Top of Atmosphere (ToA) Radiance was implemented in order to reach real land surface values. The radiance rescaling coefficients were provided in the product metadata file (MTL file) of the Landsat images. The Landsat 5 TM band data were then converted from Spectral Radiance to Reflectance by using this formula (Equation 3.3) [82]:

$$\rho_{\lambda} = \frac{\pi \cdot L_{\lambda} \cdot d^2}{E_{sun_{\lambda}} \cdot \cos_{\theta_s}} \quad (3.3)$$

where  $\rho_\lambda$  is the reflectance measured at the satellite level (dimensionless),  $\pi$  is a mathematical constant approximately equal to 3.141592 (dimensionless),  $L_\lambda$  is the spectral radiance of the sensor ( $W.m^{-2}.sr^{-1}.\mu m^{-1}$ ),  $d$  is the Earth-Sun distance (astronomical units),  $E_{sun_\lambda}$  is exoatmospheric average solar irradiance ( $W.cm^{-2}.sr^{-1}.\mu m^{-1}$ ), and  $\cos_{\theta_s}$  is solar zenith angle (degrees).

### 3.2.2.3 Conversion of Spectral Radiance ( $L_\lambda$ ) to Brightness Temperature (BT)

After the Digital Numbers (DNs) are converted to Radiance values, the Landsat 5 TM thermal band (band 6) and Landsat 8 OLI/TIRS thermal band (band 10) data should be converted from spectral radiance to Brightness Temperature (BT). The following formula (Equation 3.4) was used to convert Spectral Radiance to Brightness Temperature (BT) [83]:

$$BT = \frac{K_2}{\ln \left[ \left( \frac{K_1}{L_\lambda} \right) + 1 \right]} - 273.15 \quad (3.4)$$

where BT is top of atmosphere brightness temperature (K),  $L_\lambda$  is the spectral radiance at the sensor ( $W.m^{-2}.sr^{-1}.\mu m^{-1}$ ),  $K_1$  and  $K_2$  stand for the band-specific thermal conversion constants from the metadata. The radiant temperature was revised by adding the absolute zero (approximately  $-273.15^\circ C$ ) to get the results in Celsius.

### 3.2.2.4 Dark Object Subtraction (Histogram Minimum Method)

The Dark Object Subtraction (DOS) method is an image-based atmospheric correction technique which depends on characteristics of satellite data. In addition, it has proven to be an effective method for correcting light distribution in remote sensing satellite data [84]. The steps of the Dark Object Subtraction (DOS) method were followed to eliminate the haze components [85]. Generally, physically-based atmospheric corrections are more successful than image-based atmospheric corrections and give more accurate results. Even so, the image-based atmospheric correction techniques are among the preferred correction techniques because they can also enhance the measurement of land surface reflection. The logic of the Dark Object Subtraction

(DOS) method can be summarized as follows [86]: It is known that very small amounts of matter on the Earth's surface are absolute black, so it can be said that increasing the reflectance rate from zero to one minimum percent improves the image quality. As a result of the shadowing of some pixels that make up the satellite data images, the information in those pixels cannot be fully perceived and atmospheric scattering (path radiance) is experienced while receiving data from the satellite in the process of remote sensing. The path radiance formula (Equation 3.5) is given as follows [87]:

$$L_p = L_{min} - L_{1\%} \quad (3.5)$$

where  $L_{min}$  is the total number of pixels that contain the same digital number as this value or have a lower digital number is 0.01% of the total number of pixels in the satellite image used. The radiance value represents the digital value corresponding to this percentage [88].  $L_{1\%}$  (radiance of dark object) is the radiance obtained with this digital value ( $DN_{min}$ ). Its reflectance value is 0.01.

Reflectances of geographic objects in satellite image data created using remote sensing technology may be distorted due to atmospheric scattering and absorption and similar elements. Atmospheric correction is a kind of data preprocessing procedure that works with the drive to reverse the real reflectances of objects in nature. The presence of the atmosphere causes the radiant energy to be distributed among the detectors. However, the radiant energy cannot come into contact with the surfaces of geographic objects (the path radiance) Figure 3.2. The interaction of radiant energy with less shiny surfaces such as water bodies and vegetation [89] becomes more significant.

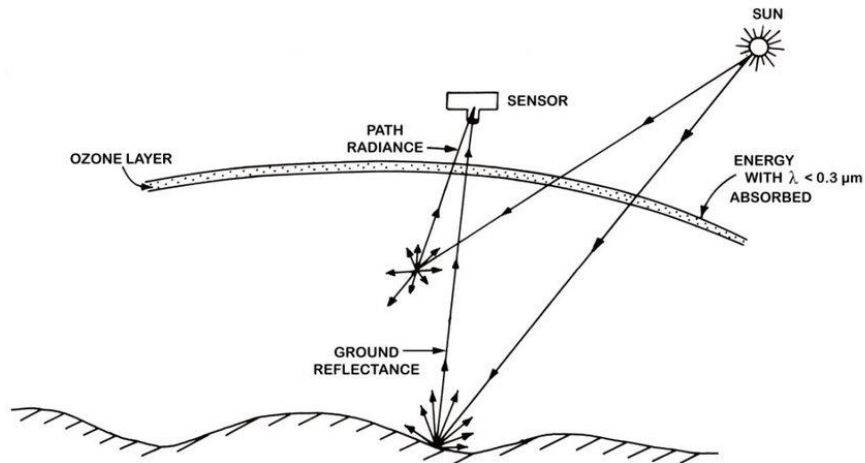


Figure 3.2: Illustration of the path radiance of the geographical objects [90]

The substances called the haze component in the literature are formed by additive scattering in remotely sensed satellite image data. Atmospheric effects increase the haze values due to the atmospheric path radiation. The haze error prevent the satellite images from being analyzed correctly and must be eliminated before the satellite image can be processed. On the other hand, correcting the haze error precludes data loss. Atmospheric effects can be of a very pronounced or not obvious type. Examples of these atmospheric effects can be given as follows:

- color shifts,
- changes in overall scene brightness and,
- losses in contrast.

The most important atmospheric effects, which should be taken very seriously, do not affect all spectral regions to the same extent. Therefore, the interrelationships between spectral channels differ. This situation conceives critical problems in the application of vegetation indices and band ratios.

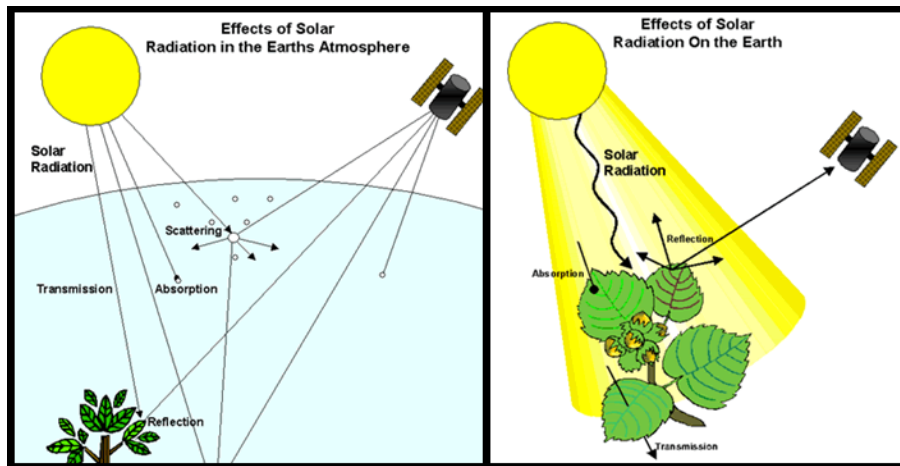


Figure 3.3: An illustration of solar radiation to explain atmospheric effects [91]

In addition, atmospheric scattering beclouds responding illumination difference induced by irregular land surface topography. Consequently, the process of normalizing satellite data cannot be applied. Standardization of satellite data is important for issues such as mosaic construction and analysis of multi-temporal satellite image data. However, the standardization of satellite image data is also hampered by atmospheric influences.

The Dark Object Subtraction (DOS) 1% method hypothesizes that for the dark objects such as deep water and shadows, the lowest reflectance value throughout a scene will be 1%. In this way, the variation between this value and the actual Digital Numbers (DN)s measured for these dark objects could be attached to the additive effects of haze. For that reason, the haze error should be dissolved by subtracting this value from all layerstacked bands of the Landsat satellite images. By applying the Dark Object Subtraction (DOS) 1% method, the effects of additive path glare in all Landsat satellite images used for the study were eliminated [84].

The Dark Object Subtraction (DOS) 1% method is deemed necessary because it helps to prevent the relatively constant error, and the degrading or masking of the small brightness changes between pixels due to real differences [85]. The constant errors cause distortion in the ratio indices for the sensor and illumination differences. The degrading or masking of small brightness changes between pixels due to real differences is a factor that would adversely affect the biophysical modeling of satellite images [92]. The pixel values of the output images obtained after the application of the Dark Object Subtraction (DOS) 1% method drew near to the reflection values on



the land surface. After the Dark Object Subtraction procedure, the histogram values of Landsat 5 TM and Landsat 8 OLI/TIRS images were examined.

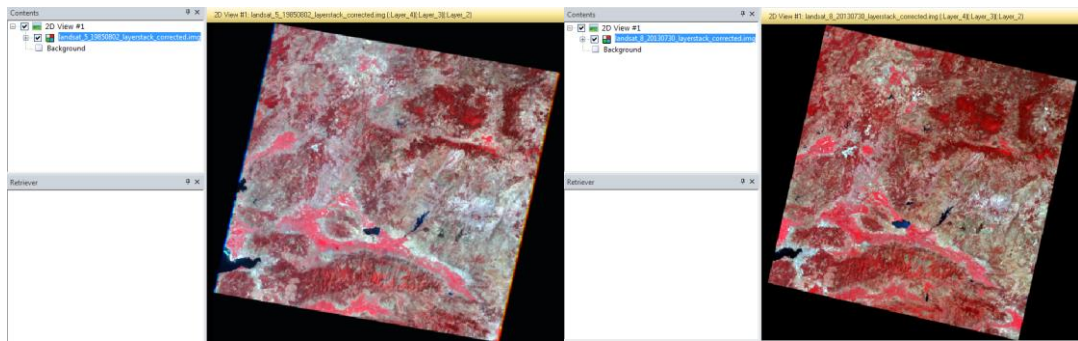


Figure 3.4: An example image of the radiometrically corrected Landsat 5 TM and Landsat 8 OLI/TIRS satellite images

When the radiometric corrections were completed, Landsat 5 TM and Landsat 8 OLI/TIRS satellite images were sub-clustered using area of interest data (AOI) to limit the study area and extract administrative boundaries of Soma district.

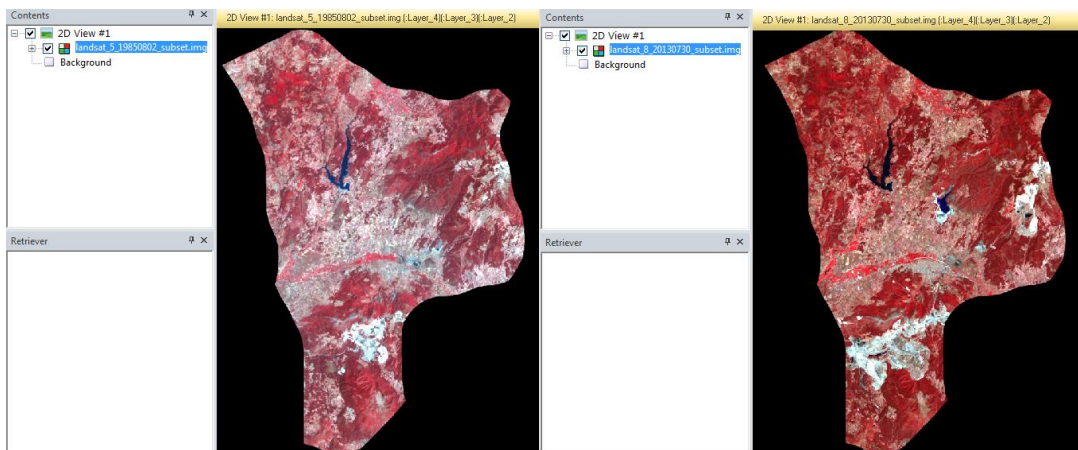


Figure 3.5: An subset image of the radiometrically corrected Landsat 5 TM and Landsat 8 OLI/TIRS satellite images

# CHAPTER 4

## DATA PROCESSING

The processing is the essential part of the study. Coal fires which are formed in the mine areas of Soma become detectable by retrieving land surface temperatures (LST). It can be said that places with higher temperature values w.r.t. the surrounding places with normal surface temperature values indicate coal fire areas. Therefore, the main purpose of the study is to locate the places with highest temperature values in the study area by analysing land surface temperatures (LST). The processed Landsat satellite images are examined and the areas where the coal fires take place and features are interpreted. The parts of the data processing are summarized in Figure 4.1:

- Calculation of the Normalized Difference Vegetation Index (NDVI),
- Estimation of Emissivity (LSE),
- Retrieving the Land Surface Temperature (LST).

### 4.1 Estimation of Land Surface Emissivity by Using Normalized Difference Vegetation Index (NDVI)

As the vegetation cover and the amount of green plants in the region increase, the thermal emissivity of the surface objects in the region also increases. Due to this connection between land surface emissivity (LSE) and normalized vegetation index (NDVI), it is necessary to have information about the normalized vegetation index (NDVI) for estimating the land surface emissivity (LSE).

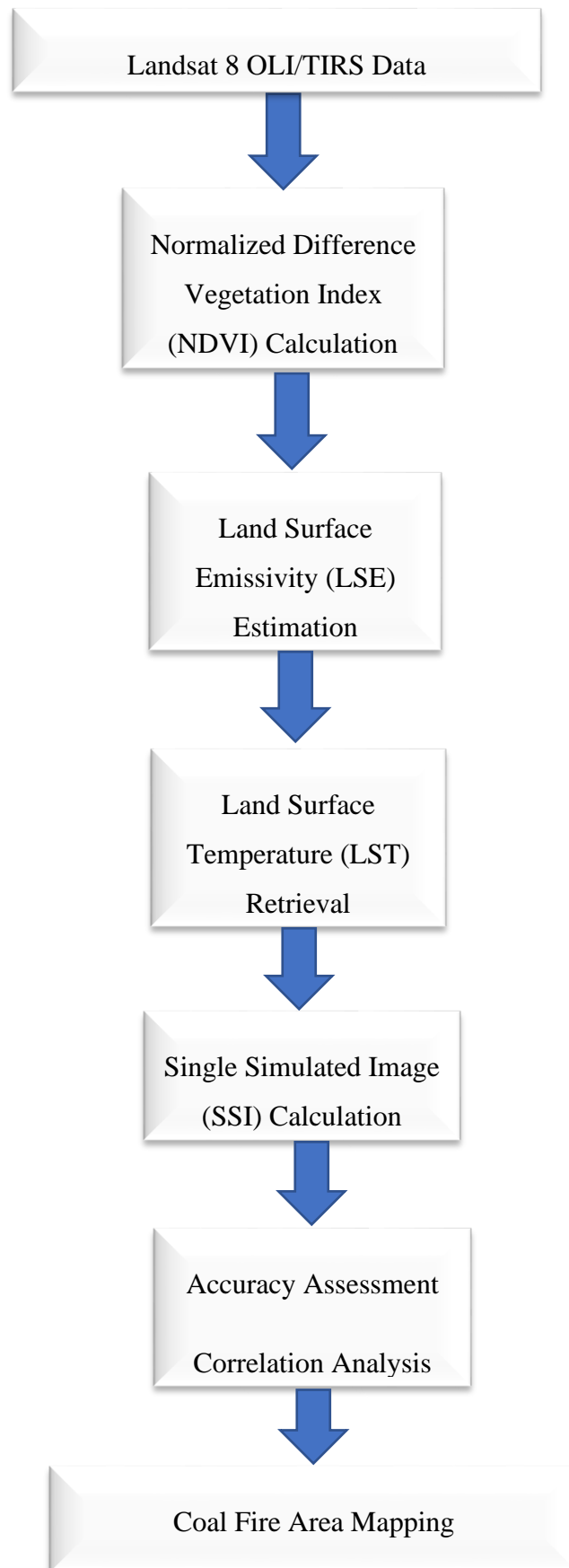


Figure 4.1: Flowchart of image processing

### 4.1.1 The Normalized Difference Vegetation Index (NDVI)

The normalized difference vegetation index (NDVI) is one of the most applied vegetation index among other vegetation indexes. It is possible to analyze the spatial-temporal changes of vegetation cover using the normalized difference vegetation index NDVI. According to several researchers, the normalized difference vegetation index (NDVI) is one of the main components that can be used to learn about the vegetation cover of a particular region by processing data obtained by remote sensing methods [93]. Vegetation indexes are frequently preferred concepts in researching the vegetation characteristics of a certain region. Therefore, these indexes have been used in many studies and applications to improve vegetation characteristics.

A number of vegetation indexes have interested with low red and high near infrared reflectance qualifications, especially the normalized difference vegetation index (NDVI) [94]. The relationship between the obtained energy and emitted energy by surface objects is estimated using the red and near infrared (NIR) bands within the scope of vegetation indexes [95]. The variations between the normalized difference vegetation index (NDVI) values depend on their relative reflectances in the red and NIR bands. The Landsat visible (red band) and near-infrared (NIR band) bands were necessary to investigate the Normal Difference Vegetation Index (NDVI). The red and near infrared (NIR) bands take non-identical reflectance values, so the estimated normalized difference vegetation index (NDVI) values differ according to characteristics of the landcover they are in. Surface water bodies and deep water areas have a higher reflectance rate in the visible region than the near infrared (NIR) region, so the normalized difference vegetation index (NDVI) value gets negative value in these kind of areas. The normalized difference vegetation index (NDVI) reflects similarly in the red and near infrared (NIR) zones in areas where rock fragments are common in flat areas of land and in soils where vegetation is weak. Hence, the normalized difference vegetation index (NDVI) is measured from a value that is very close to zero. Formula (4.1) is the formula used to calculate the normalized difference vegetation index (NDVI) values and is given below:

$$NDVI = \frac{NIR - RED}{NIR + RED} \quad (4.1)$$

where RED and NIR are the spectral reflectance in red and near infrared band, respectively.

The lowest normalized difference vegetation index (NDVI) value is -1 and the highest normalized difference vegetation index value is +1. Negative normalized difference vegetation index (NDVI) values could be the areas of water bodies, manmade (unnatural) structures, rocks, clouds, snow. The areas with bare soil generally fall within the 0.1-0.2 normalized difference vegetation index (NDVI) value interval. Also, plants have positive values between 0.2 and 1 values. NDVImax, NDVImin the normalized difference vegetation index NDVI values of vegetation and open soil. In general, a positive value for the normalized difference vegetation index (NDVI) is found to indicate green vegetation. Vegetation classification using the normalized difference vegetation index (NDVI) index is made according to certain criteria. These criteria are briefly summarized in the Table 4.1 below.

Table 4.1: The Interval of NDVI Values According to The Type of Land Cover

<b>Vegetation Types</b>	<b>Class Definition</b>	<b>NDVI Value</b>
<b>Non-vegetation</b>	Barren areas	-1 to 0.199
	Built-up areas	
	Road networks	
<b>Low vegetation</b>	Scrubs	0.2 to 0.5
	Grassland	
<b>High vegetation</b>	Forest	0.501 to 1.0

In this table, the normalized difference vegetation index (NDVI) value ranges of low density vegetation areas, medium density vegetation areas and high density vegetation areas are clearly indicated. The normalized difference vegetation index (NDVI) index can also be applied to differentiate vegetation cover and soil class materials and to investigate whether plants are healthy [96]. In Figure 4.2, the correlation between plant health and bands of visible red and near-infrared that used for obtaining NDVI values is denoted.

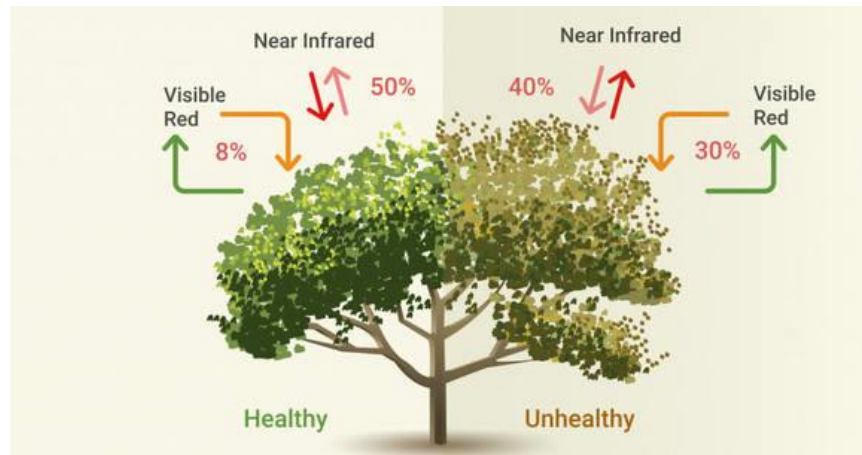


Figure 4.2: Correlation of plant health and bands of visible red and near-infrared that used for obtaining NDVI values [97]

Estimation of the land surface emissivity (LSE) by applying the normalized difference vegetation index (NDVI) information in the study of retrieving the land surface temperature (LST) has been examined by many researchers [43,42,88]. Assessment of land surface emissivity (LSE) extraction from the normalized difference vegetation index (NDVI) data is linked to five different conditions. These conditions can be explained as follows:

- NDVI < 0 condition: If the normalized difference vegetation index (NDVI) value are less than 0, the pixels are considered to be water pixels.
- NDVI < 0.2 condition: If the normalized difference vegetation index (NDVI) value is less than 0.2, the pixels are considered to be bare soil or built-up area pixels.
- NDVI > 0.2 condition: If the normalized difference vegetation index (NDVI) value is greater than 0.2, the pixels are considered to be green plants pixels.
- $0.2 < \text{NDVI} < 0.5$  condition: If the normalized difference vegetation index (NDVI) pixels are between 0.2 and 0.5, the pixels consist of a mixture of bare soil and vegetation pixels.
- NDVI > 0.5 condition: If the normalized difference vegetation index (NDVI) value is greater than 0.5, the pixels are generally considered to be dense vegetation pixels.

The normalized difference vegetation index (NDVI) has been used frequently both to conduct studies on land use and land cover (LULC) and to provide calculation of land surface temperature (LST) [98-101] because the normalized difference vegetation index (NDVI) individuates healthy vegetation pixels from dead vegetation pixels based on the chlorophyll aspect present in the plants and this fact makes the normalized difference vegetation index (NDVI) important. Estimating thermal emissivity on the land by averaging a series of point measurements has been found to be less reliable than satellite-based NDVI measurements [43]. Satellite-based NDVI measurements are more successful on finding actual thermal emissivity at a pixel level.

In this study, the normalized difference vegetation index (NDVI) values of 25 Landsat 5 TM and 23 Landsat 8 OLI/TIRS subset images, which were geometrically and radiometrically corrected, were calculated using the above-mentioned the normalized difference vegetation index (NDVI) formula (Equation 4.1). ERDAS Imagine 2014 program was used for this calculation process and the normalized difference vegetation index (NDVI) formula was created and run as a model in model maker tool. The normalized difference vegetation index (NDVI) values calculated from Landsat 5 TM and Landsat 8 OLI/TIRS subset images are used in the estimation of land surface emissivity (LSE) in the next step.

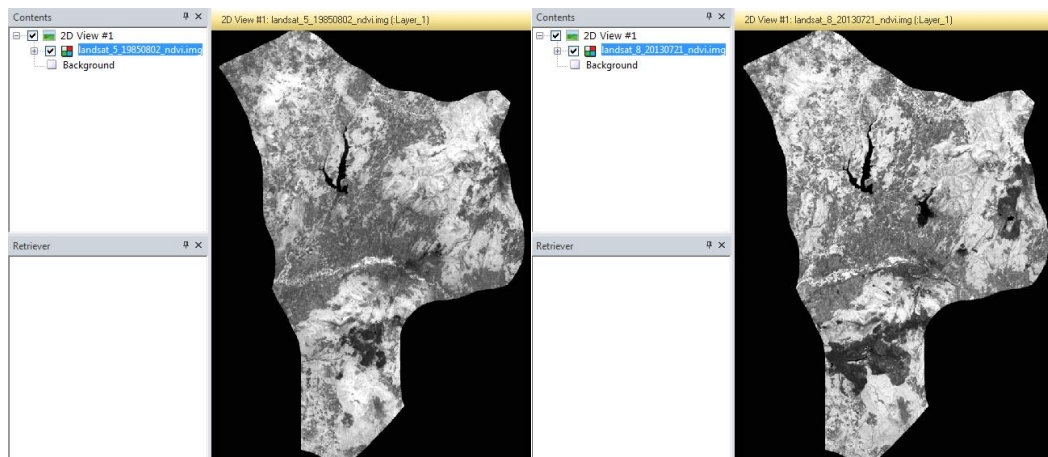


Figure 4.3: An example NDVI image which were generated by implementing Landsat 5 TM and Landsat 8 OLI/TIRS satellite images

### 4.1.2 The Land Surface Emissivity (LSE)

Kinetic temperature of an object can be acquired from the thermal radiation data, if thermal emissivity of the object is known. The calculation of the land surface emissivity (LSE) enables higher accuracy temperature estimation with its thermal data. The thermal emissivity of the Earth's surface depends on three elements:

- Water content of the surface materials,
- Albedo of the surface materials, and
- Vegetation cover.

There is a relationship between the average value of thermal emissivity ( $\epsilon$ ) and the normalized difference vegetation index (NDVI) which was found by Van de Griend and Owe (1993). According to this relationship between the thermal emissivity and the normalized difference vegetation index (NDVI), the formula for estimating the land surface emissivity (LSE) (Equation 4.2) can be given as follows:

$$\epsilon = (1.0094 + 0.047) * \ln (NDVI) \quad (4.2)$$

The normalized difference vegetation index (NDVI) values calculated from 25 Landsat 5 TM and 23 Landsat 8 OLI/TIRS subset images are used in the estimation of land surface emissivity (LSE). ERDAS Imagine 2014 program was used for this estimation process and the formula for estimating the land surface emissivity (LSE) was created and run as a model in model maker tool.

## 4.2 Retrieval of The Land Surface Temperature (LST)

Land surface temperature (LST) can be defined in the simplest way as the hotness of the Earth's surface. In the past studies, a group of sample points belonging to a particular area was calculated for the land surface temperature (LST) data. These points would then be interpolated into isotherms to get the field data. It was difficult to make the land surface temperature (LST) retrieval of a certain area those days, but



with the invention of satellites and their high resolution sensors, the land surface temperature (LST) calculations using remote sensing methods and thermal band data started to be made easier and faster spatially.

The surface temperature of the land (LST) can be measured by processing the data received by the satellites from the Earth's surface within the possibilities provided by remote sensing science. The land surface temperature (LST) data is important because it enables the temporal and spatial properties of the land surface balance to be known and contributes to the realization of the change of this balance.

The land surface temperature (LST) is emitted by the surface of the Earth. The land surface temperature (LST) is also a type of temperature usually measured in Kelvin but in this study, temperature measurements are made in Celcius. The increasing presence of greenhouse gases in the atmosphere in recent years is a fact that should be taken into account in the land surface temperature (LST) measurements. The negative effects of the increase of land surface temperature (LST) values on nature and life can be exemplified by a few examples:

- the melting of glaciers and ice sheets in the polar region and the rise in sea levels and the increase in the frequency of natural disasters such as floods and tsunamis,
- the rainfall above seasonal normals in places of monsoons,
- the local climate changes,
- the land use and land cover (LULC) change as a result of the influence of the vegetation cover of the land for natural and anthropogenic reasons, etc.

All of the negative effects mentioned above are the consequences of an unacceptable increase in the land surface temperature (LST) values, but if it is to be interpreted from a different perspective, it is certain that these results will affect irreversibly the land surface temperature (LST) values in the long term. As a result of which, the land surface temperature (LST) is an essential phenomenon that needs to be examined at regular intervals.

Various algorithms have been used to retrieve the land surface temperature (LST) as a result of processing satellite images obtained by remote sensing techniques. These algorithms can be listed as follows:

- the single-channel algorithm
  - ✓ single-window algorithm
  - ✓ universal single-channel algorithm
- mono-window algorithm
- split-window algorithm
- multi-channel algorithm

In this study, the land surface temperature (LST) values of the 25 Landsat 5 TM and 23 Landsat 8 OLI/TIRS images were retrieved by implementing the single-channel algorithm. The land surface temperature (LST) retrieval process was executed in ERDAS Imagine 2014 program and the formula that was applied to retrieve the land surface temperature (LST) was created and run as a model in Erdas model maker tool.

#### 4.2.1 The Single Channel Algorithm for The Retrieval of Land Surface Temperature (LST)

Thermal band data is preferred in retrieving the temperature of the land surface because the maximum emission data from the Earth's surface is provided in the range of the thermal infrared (TIR) band [102]. The top of atmosphere (TOA) radiation is the radiance that leaves the Earth's surface after being modified due to the atmospheric effects. The thermal infrared (TIR) sensors measure the top of atmosphere (TOA) radiation to obtain thermal data. It is essential that two major issues are solved during the acquisition of the land surface temperature (LST) with sensors that collect thermal infrared data in satellites in terms of the accurate results of the data [103]: Atmospheric corrections to avoid effects caused by the atmosphere, and retrieving the land surface emissivity (LSE).

A lot of researches have been done to improve the acquisition of land surface temperature (LST) from satellite-based thermal infrared (TIR) data and significant progress has been made in this regard over past years. The three main land surface temperature (LST) retrieval methods can be given as follows [102]:

- The single channel (SC) methods,
- The multi channel methods, and
- The multi angle methods.

Different theories have been examined for each of the methods mentioned above and designed to generate the land surface temperature (LST) data, and different thermal band (TIR) data have been used according to the sensor properties. The single channel (SC) method uses a set of predictive atmospheric parameters to correct disturbances in a single thermal band (a single channel) due to atmospheric effects to retrieve the land surface temperature (LST) [104-106]. Unlike the single channel method, the multi-channel method aims to reach the land surface temperature (LST) data by using various absorption in two different thermal infrared (TIR) channels [107,108,109,110,111,62]. The split window algorithm can be given as an example of the multi-channel methods. The multi-angle method, on the other hand, observes the Earth's surface differently than other methods, so the atmospheric absorption of this method varies due to its observing techniques [112].

Land surface temperature can be estimated using multifold time satellite images of Landsat datasets, which have medium resolution and are quite sufficient to provide data for long time intervals. In this way, many useful studies can arise on various environmentally focused topics such as spatial-temporal analysis of evapotranspiration and urban heat island development [113,114]. The single channel (SC) algorithm is a type of algorithm developed for calculating the temperature of the land surface. The basic functioning of the single channel (SC) algorithm is that the land surface temperature (LST) is retrieved by using a single thermal band data. The single channel (SC) algorithm is an algorithm which has an extremely simple structure and this algorithm provides results with good accuracy. The reason why the single channel (SC) algorithm is so widely used is that the algorithm requires a single thermal band to

retrieve the land surface temperature (LST) from a number of satellite images such as Landsat, MODIS, ASTER, etc. The single channel (SC) methods commonly used nowadays can be given as follows:

- the radiative transfer equation (RTE) method,
- the mono-window (MW) method that were designed by Qin et al. (2001) [115], and
- the generalized single-channel (GSC) method proposed by Jiménez-Muñoz and Sobrino (2003) [106] and after that revised by Jiménez-Muñoz et al. (2009) [105].

It can be said that the fundamental difference between all three the above-mentioned LST retrieval methods is the atmospheric correction procedure. In the radiative transfer equation (RTE) method, corrections are made with the help of three different atmospheric parameters based on a particular radiative transfer model (for example MODTRAN) in order to eliminate the deterioration caused by atmospheric effects: atmospheric transmittance, downwelling atmospheric radiance and upwelling atmospheric radiance [116]. The mono-window algorithm (MW algorithm) is a kind of algorithm that can provide atmospheric correction using two different atmospheric parameters: atmospheric transmittance and effective mean atmospheric temperature. These two atmospheric parameters are adapted sequentially to atmospheric water vapor (AWV) content and near surface air temperature (NSAT) [117]. Three atmospheric functions are designed for the generalized single-channel (GSC) algorithm. These three atmospheric functions of the algorithm are thought to be due - in theory- only to the atmospheric water vapor (AWV) substance [118,106].

The atmospheric water vapor (AWV) and the near surface air temperature (NSAT) have an important role in atmospheric corrections as the determining factors in the radiative transfer equation (RTE), the mono-window (MW) and the generalized single-channel (GSC) methods. Also, the atmospheric water vapor (AWV) and the near surface air temperature (NSAT) make the atmospheric corrections with simple and useful land surface temperature (LST) estimation formulas. Thus, the single channel (SC) method is referred to as a more preferred useful and practical method of obtaining the land surface temperature (LST).

A single channel algorithm which was proposed by Artis and Carnahan (1982) [119] is used in this study. The single channel algorithm does not require large amount of parameters for land surface temperature (LST) retrieval in contrary to the mono-window algorithm [115] and the generalized single-channel method [106]. The formula of the single-channel algorithm (Equation 4.3) can be given as follows:

$$T_s = \frac{T_{sensor}}{1 + (\lambda * T_{sensor}/\rho) * \ln \varepsilon} \quad (4.3)$$

where  $\lambda$  is the wavelength of the emitted radiance which means the average wavelength. In this research,  $\lambda$  was accepted in the value of 11.45 $\mu\text{m}$  for Landsat 5 TM thermal band (band 6) data and 10.895 $\mu\text{m}$  for Landsat 8 OLI/TIRS thermal band (band 10) data as average wavelength.  $\rho = h \times c / j$  in m Kelvin, where  $h$  is Planck's constant ( $6.626 \times 10^{-34}$  J s), A commonly used approximation of Planck's function specific to Landsat is given by G. Chander and B. Markham (2003) [120],  $c$  is the velocity of light ( $2.998 \times 10^8$  m/s),  $j$  is Boltzmann constant ( $1.38 \times 10^{-23}$  J/K), and  $T_{sensor}$  is at-sensor brightness temperature in Kelvin.

The use of a single wavelength value to retrieve land surface temperature (LST) from radiance with one sensor with a exact channel width (bandpass effects) were adopted by several researchers [121,122]. The formula (Equation 4.4) that calculates brightness temperature is given as follows:

$$T_{sensor} = \frac{K_2}{\ln(1 + K_1/L_{sensor})} \quad (4.4)$$

where  $K_1$  is 607.76  $\text{W} \cdot \text{m}^{-2} \cdot \text{sr}^{-1} \cdot \mu\text{m}^{-1}$  and  $K_2 = 1260.56 \text{ W} \cdot \text{m}^{-2} \cdot \text{sr}^{-1} \cdot \mu\text{m}^{-1}$  for Landsat 5 thermal band (band 6) data.  $K_1$  is 774.8853  $\text{W} \cdot \text{m}^{-2} \cdot \text{sr}^{-1} \cdot \mu\text{m}^{-1}$  and  $K_2 = 1321.0789 \text{ W} \cdot \text{m}^{-2} \cdot \text{sr}^{-1} \cdot \mu\text{m}^{-1}$  for Landsat 8 thermal band (band 10) data. These  $K_1$  and  $K_2$  constants were used to solve the bandpass effect.

According to the results of some studies on land surface temperature (LST) retrieval, it was determined that when the consistency of Landsat 8 thermal bands (band 10 and band 11) was compared, band 11 showed more uncertainty than band 10 [71]. Therefore, one of the thermal band data used in this study, Landsat 8 OLI/TIRS images were studied with band 10 as the thermal band data.

#### 4.2.1.1 The Computation of Simulated Single Image (SSI) of Landsat 5 TM and Landsat 8 OLI/TIRS Land Surface Temperature (LST) Data

There is relationship between land cover and land surface temperature. Especially, in places where there is little or almost no land cover, easily noticeable changes are observed in the land surface temperatures belonging these places.

Objects are sampled as pixels in satellite image data of certain time series. To easily evaluate time series data as a single image without dealing the whole series of data, Çorumluoğlu [123] purposed a Simulated Single Image method. The pixels represent variability as the characteristics of the smallest parts of lands (SLA) in time. This representation therefore includes trend analyses. So, trend analysis is a type of linear regression analysis of a variable which is done depending on the time. All pixel values in the output image from the trend analysis allow observing the change trends over time in these smallest areas of lands (SLA). The changes are calculated for the entire study area using the pixel values in the satellite image data sets collected in different years (in this study, different data are used for each year). Variable Rate of Change (VCR) is described as the slope of a variable (here, LST) over time, which is found by using the values of the exact pixel in different satellite images and the linear regression equation. The least square method is implemented to calculate the regression slope. The trend/slope formula (Equation 4.5) is given as follows [123]:

$$Slope_k = \frac{n \sum_{i=1}^n i * V_{ki} - (\sum_{i=1}^n i) * (\sum_{i=1}^n V_{ki})}{n * \sum_{i=1}^n i^2 - (\sum_{i=1}^n i)^2}, \quad (4.5)$$

$k(1, \dots, l), i(1, 2, 3, \dots, n)$

where  $k$  is for variables,  $l$  is the total number of the variables (LST variable), LST, therefore  $k$  is 1 and  $Slope_k$  is for slope of  $k^{\text{th}}$  variable,  $V_{ki}$  stands for  $k^{\text{th}}$  variable's pixel value in the  $i^{\text{th}}$  time serious image and  $i$  stands for the number of sequential year and  $n$  is for the total number of years in the time series, in this study  $i$  is 25 for Landsat 5 TM and 18 for Landsat 8 OLI/TIRS data.

$$SD_k = \sqrt{\frac{\sum_{i=1}^n (V_{ki} - m_k)^2}{n - 1}} \quad (4.6)$$

$$m_k = \left( \sum_{i=1}^n V_{ki} \right) / n \quad (4.7)$$

where,  $m_k$  is the mean value for each SLA in the study region computed from the pixel values through the entire time series data for the LST variable.

The mean, standard deviation and trend images of all land surface temperature (LST) images in different time series are calculated as a single output image. Then, using a formula, the variation of the variable, in this case the land surface temperature (LST), is simulated into a single result image. The result image is called as a simulated single image (SSI) for whole land surface temperature (LST) images and it simulates all relevant time-related data [123]. This is explained by the fact that the single simulated image (SSI) includes the average (mean), trend, and range of variation of the time-related data for the land surface temperature (LST) variable in terms of statistical values. In short, an SSI pixel value for a variable (LST) represents the serious images of the variable for a given time interval in pixels and stands as a single value statistically estimated from the slope, standard deviation and mean values of all-time related data for individual smallest land areas (SLA). Thus, it enables to examine the distribution of the variable (LST) in terms of time as a single image and simulates the properties of the smallest areas of land practically. The standard deviation refers to the range of data change relative to the mean value. The slope corresponds to the tendency of a set of data to change.

$$SSI_k = Slope_k * SD_k + M_k \quad (4.8)$$

In this study, the land surface temperature (LST) images created by calculating from 25 annual Landsat 5 TM satellite images containing spatial data for 25 consecutive years (from 1985 to 2009) were used to acquire simulated single image (SSI) data. First of all, the average (mean) and standard deviation values of these 25 Landsat 5 TM land surface temperature (LST) images were found. Then, the slope of the 25 Landsat 5 TM land surface temperature (LST) images were calculated based on the formula for the slope calculation.

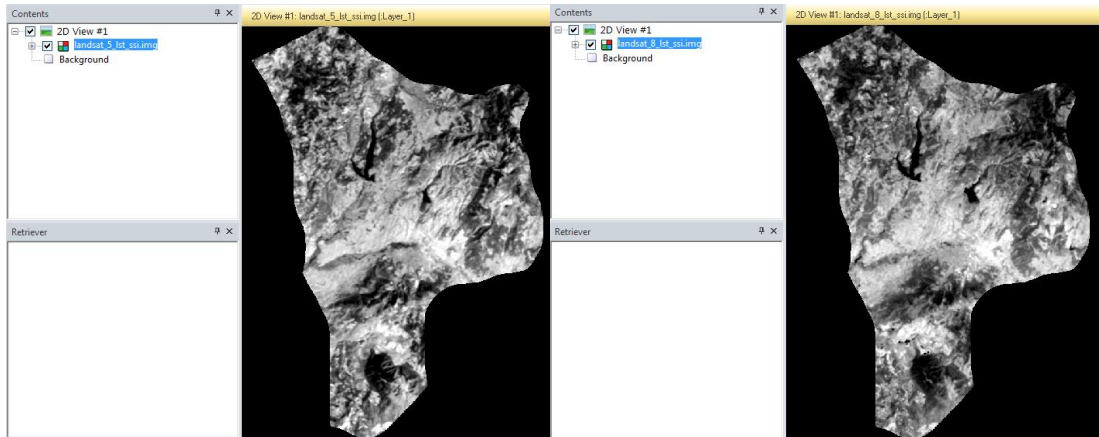


Figure 4.4: The Simulated Single Image (SSI) of 25 Landsat 5 TM land surface temperature images and 18 Landsat 8 OLI/TIRS land surface temperature (LST) images (Band 10)

The land surface temperature images were created by calculating from 18 annual Landsat 8 OLI/TIRS satellite images containing spatial data for 18 consecutive months of years (from 2013 to 2020) were used to acquire single simulated image (SSI) data. First of all, the average and standard deviation values of these 18 Landsat 8 OLI/TIRS land surface temperature (LST) images were found. Then, the slope of the 18 landsat 8 OLI/TIRS land surface temperature (LST) images were calculated based on the formula for the slope calculation. There is a reason why Landsat 8 OLI/TIRS land surface temperature (LST) images and the single simulated image (SSI) were formed with the Landsat 8 OLI/TIRS satellite images obtained from different months of the same years. This is because Landsat 8 OLI/TIRS satellite was put into operation in the recent past, in 2013, and therefore does not have much annual data.

The main reason for this process is to interpret the average (mean), standard deviation and slope (trend) of the images that contain the distribution information of the land surface temperatures (LST) of the satellite images collected by satellite sensors in different years by formed using single simulated image data. In this way, some kind of verification of the process can be made. In addition, the single simulated image (SSI) calculations were made for both Landsat 5 TM and Landsat 8 OLI/TIRS normalized LST images. However, the resulting output data were considered to be insufficient for other stages and were not included in the study.

As a result, the annual Variable Rate of Change (VCR) of 25 Landsat 5 TM and 18 Landsat 8 OLI/TIRS land surface temperatures (LST) were calculated. Each LST pixel value in the spatial images forming a pixel cube over the years specified in the study



simulated the trends of change, the standard deviation of change, and the average change of the LST variable for each LSA. Since the created Landsat 5 TM land surface temperature (LST) images did not meet the expected accuracy sensitivity, further operations were continued with Landsat 8 OLI/TIRS land surface temperature (LST) images and simulated single images (SSI) from time series data.

#### 4.2.1.2 Evaluation of Landsat 8 OLI/TIRS Simulated Single Image (SSI) by Creating Threshold Value

The lowest and highest temperature values of Landsat 8 OLI/TIRS single simulated images (SSI) were taken as basis and threshold values were determined in the range of 10-15% for both band 10 and band 11. In this way, the areas with the highest probability of coal fires were located with more accurately and it became easier to focus on the areas with high temperatures that appeared outside the coal mine areas in the land surface temperature (LST) images. This process was executed in ArcGIS 10.8. data processing program. The generated images were saved in .kmz format and transferred to the Google Earth program, and the data showing the mining licenses in Soma were evaluated visually in the .kmz format.

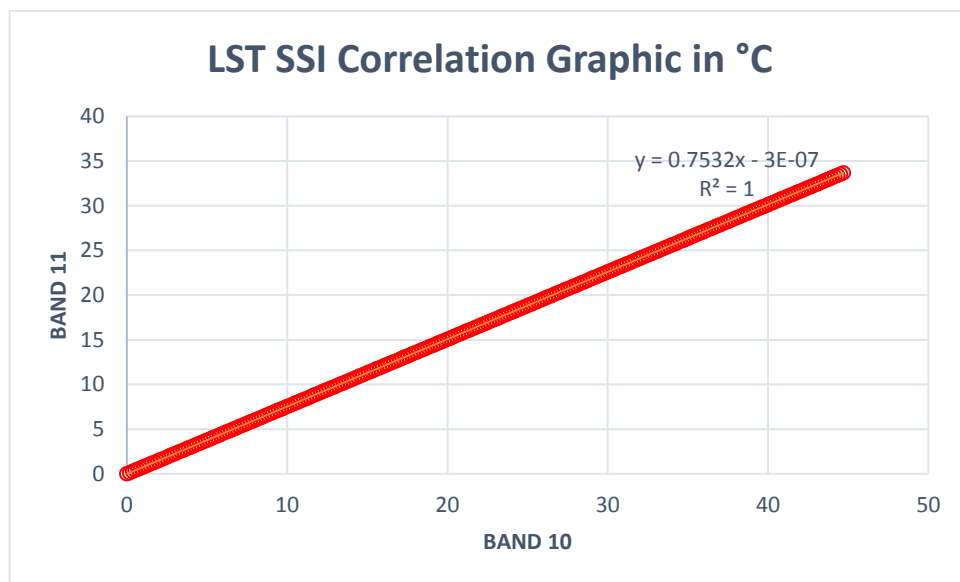


Figure 4.5: The LST SSI Band 10 and 11 Correlation

### 4.2.1.3 Normalized Land Surface Temperature Calculation

After the land surface temperatures (LST) of Landsat 5 TM and Landsat 8 OLI/TIRS satellite images were retrieved using a single channel algorithm, the global minimum and global maximum values of the retrieved land surface temperature (LST) data were computed. In this way, the normalized land surface temperature (LST) values were calculated by adapting the global minimum and global maximum data to a certain formula.

The normalization of the land surface temperatures means that the temperature values were scaled between the minimum values and maximum values in order to compare the land surface temperature (LST) data which were captured at different time intervals. The normalized land surface temperature (LST) (unitless) is estimated for each pixel of the land surface temperature (LST) data. The normalized land surface temperature formula (Equation 4.9) is defined as follows:

$$T^*_s = (T_s - T_{min}) / (T_{max} - T_{min}) \quad (4.9)$$

where  $T_{min}$  is global minimum of land surface temperature values,  $T_{max}$  is global maximum of land surface temperature values.

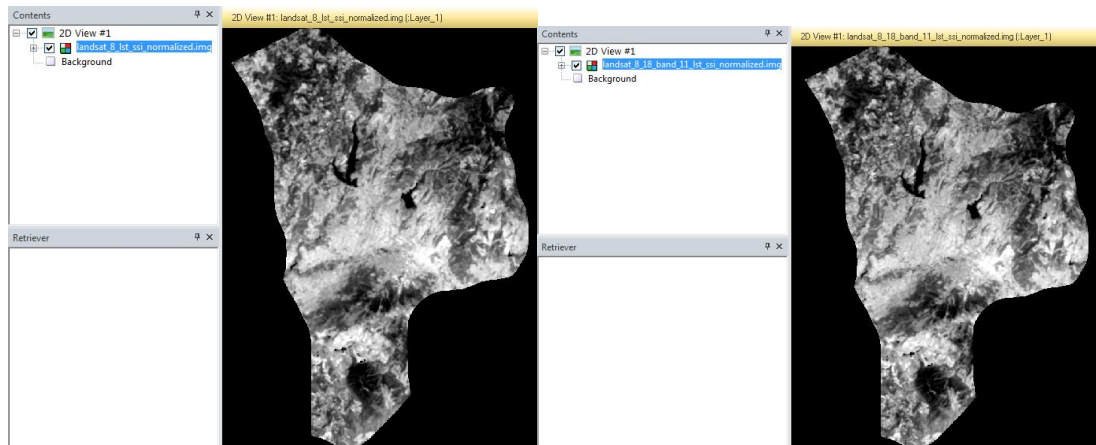


Figure 4.6: Normalized land surface temperature images of the Landsat 5 TM and Landsat 8 OLI/TIRS satellites

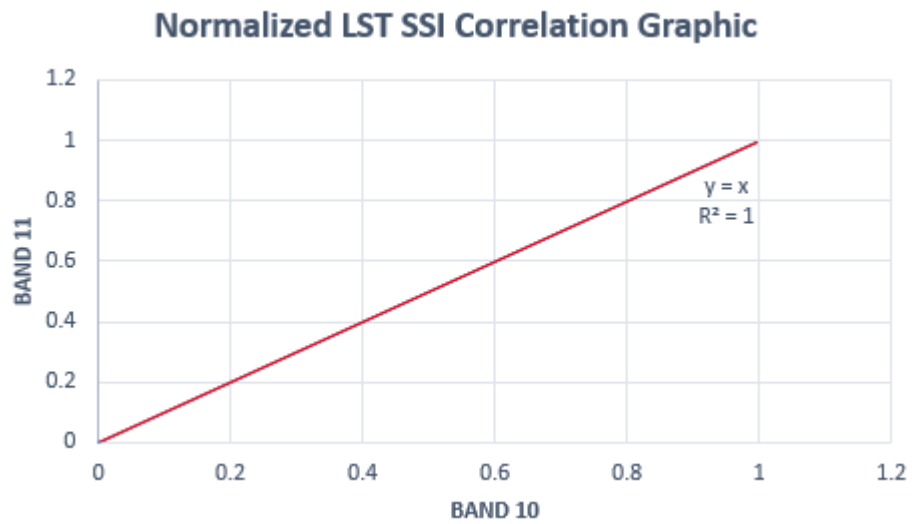


Figure 4.7: The Normalized LST SSI Band 10 and 11 Correlation of Landsat 8

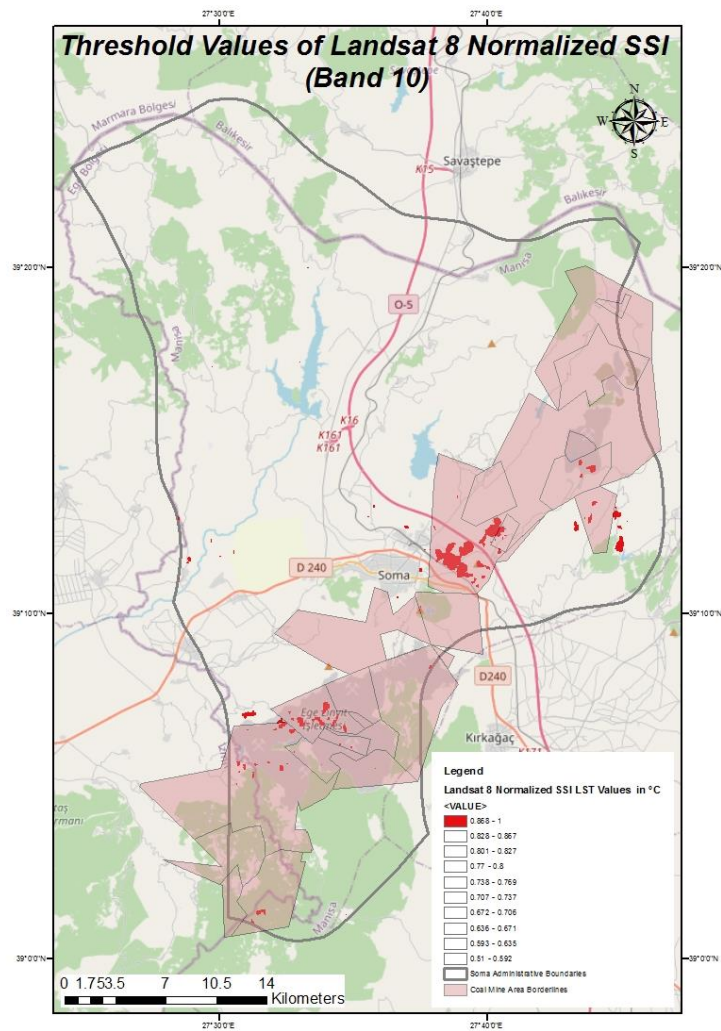


Figure 4.8: The Landsat 8 OLI/TIRS simulated single threshold LST image for Band 10

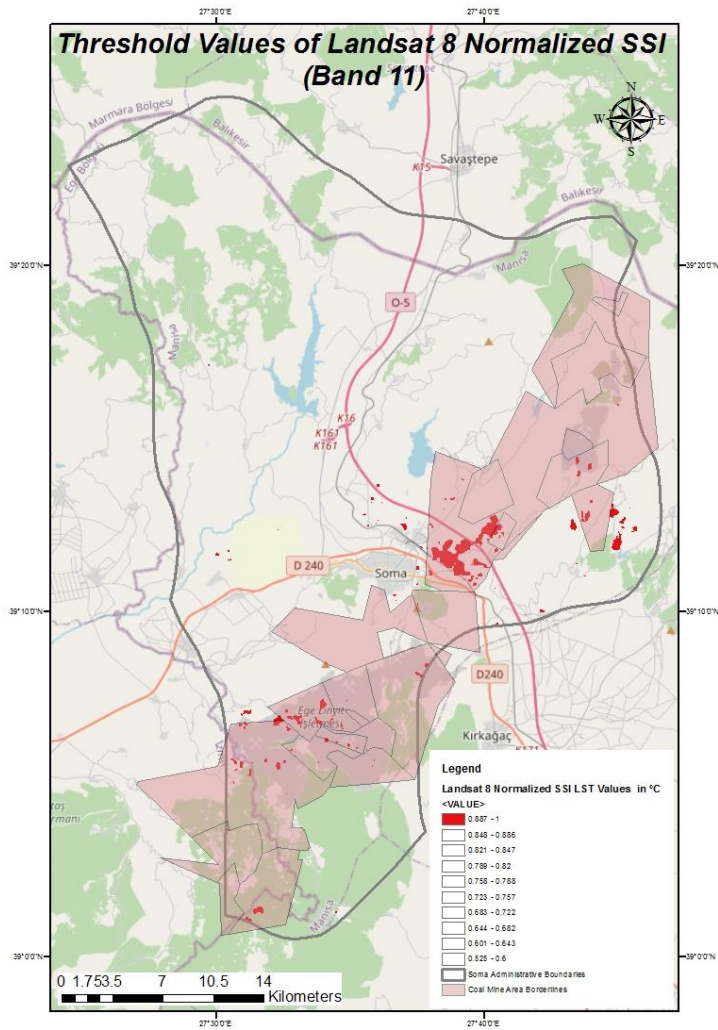


Figure 4.9: The Landsat 8 OLI/TIRS simulated single threshold LST image for Band 11

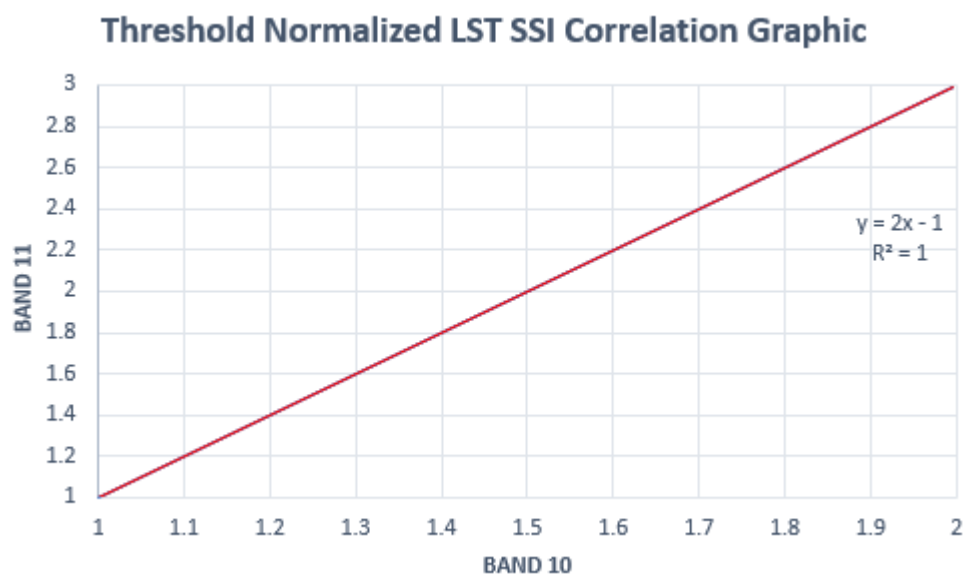


Figure 4.10: The Landsat 8 Threshold Normalized LST SSI Band Correlation Graphic

A total of 5522 common pixels were detected for both Landsat 8 LST SSI Band 10 threshold data and Landsat 8 LST SSI Band 11 threshold data. 911 pixels were located different from the Landsat 8 LST SSI Band 11 threshold data. In the Landsat 8 LST SSI Band 11 threshold value data, 2331 pixels are elsewhere than the pixels in Landsat 8 LST SSI Band 10 threshold data. A total of 5379 pixels of Landsat 8 LST SSI Band 10 threshold data and 6289 pixels of Landsat 8 LST SSI Band 11 threshold value data detected in the area covered by the coal mines. The Landsat 8 LST SSI Band 10 threshold data has an accuracy of about 83.62 percent, while the Landsat 8 LST SSI Band 11 threshold data has an accuracy of about 80.08 percent. Also, the non-overlap ratio of Landsat 8 LST SSI Band 10 threshold data and Landsat 8 LST SSI Band 11 threshold data has been calculated as approximately 67.39 percent. Therefore, the Landsat 8 LST SSI Band 10 threshold data which have higher accuracy value were preferred.

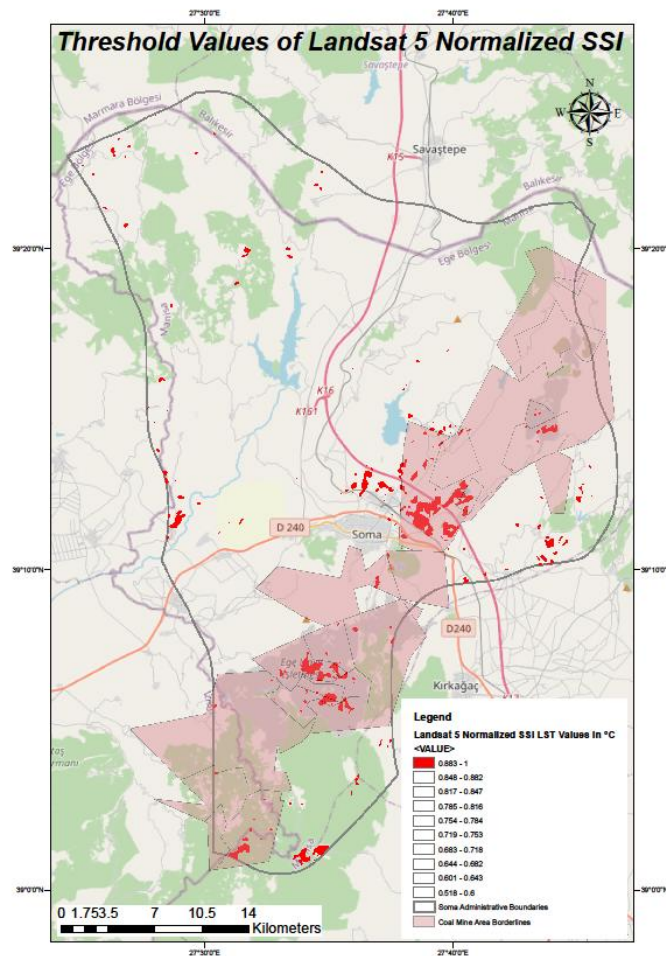


Figure 4.11: The Normalized threshold LST simulated single image of Landsat 5 TM

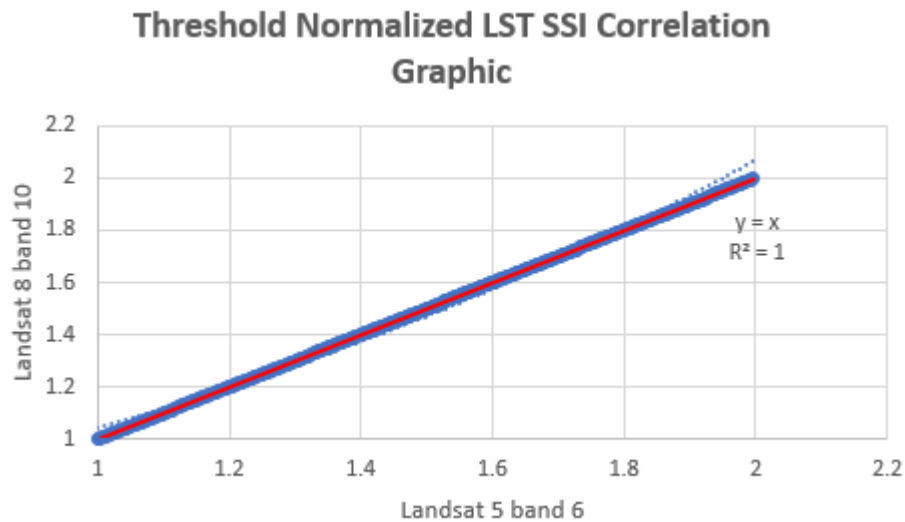


Figure 4.12: Landsat 5 Band 6 and Landsat 8 TIRS Band 10 Correlation Graph of Normalized Threshold LST SSI values

A number of 3178 common pixels were identified for both Landsat 5 TM LST SSI Band 10 threshold data and Landsat 8 LST SSI Band 10 threshold data. The correlation between the Normalized Landsat 5 TM LST SSI threshold image values and the Normalized Landsat 8 SSI LST Band 10 threshold image values is 97.03 percent.

#### 4.2.1.4 The Assessment of Hot Spots from The Landsat 8 OLI/TIRS SSI LST Data in the Licensed Coal Mine Areas in Soma

As a result of processing the main data source Landsat 8 OLI/TIRS satellite images used in this thesis, land surface temperature (LST) retrievals were made and coal fires were thought to be active in regions with extremely high temperatures. Before performing the data processing, one of the thermal bands (Band 10) was layered together with the other bands during the merging of the satellite bands (Band 2, Band 3, Band 4, Band 5, Band 6, Band 10 and Band 7). Thus, an analysis environment was created for the land surface temperatures (LST) obtained using a single thermal band algorithm and other bands.

As mentioned above sections, several analyses have been made to place land parts with highest LST values in the region and thus, to reveal coal fire areas and then to investigate the accuracy of the processes done for retrieving the places with highest land surface temperature (LST). After the processes for Band 10, Band 11, another

thermal band of the Landsat 8 OLI/TIRS satellite bands, was combined with other bands by layer stacking (Band 2, Band 3, Band 4, Band 5, Band 6, Band 11 and Band 7). Radiometric corrections were applied, NDVI, land surface emissivity (LSE), land surface temperature (LST) retrieval and SSI calculations were performed, respectively for 18 Landsat 8 OLI/TIRS satellite data as well.

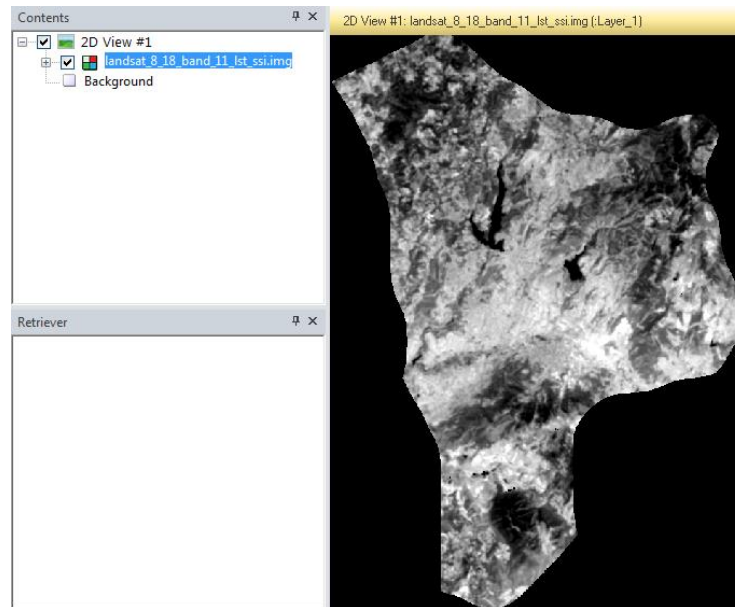
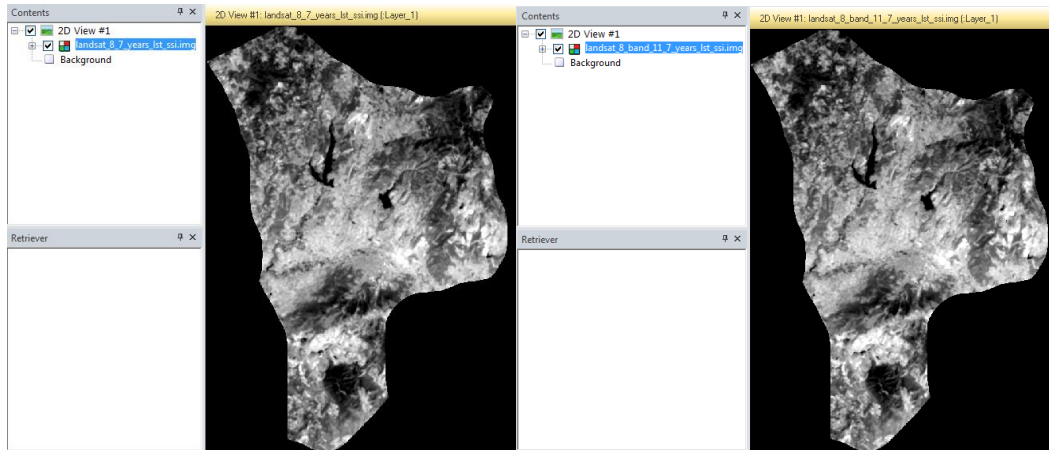


Figure 4.13: The SSI LST image from 18 Landsat 8 OLI/TIRS LST data using Band 11

In addition, the SSI values of the annual land surface temperature (LST) data for July, which have both Band 10 and Band 11 thermal bands, were calculated (Figure 4.14 a and b). Since the appropriate Landsat 8 satellite data for July 2014 could not be found, this year's data was not included in the data processing. In total, calculations were made for 7 years (2013, 2015, 2016, 2017, 2018, 2019 and 2020). The reason for choosing the same month is to question the accuracy of the results obtained by using data from different months. July was chosen because it is the common month for all data. Since there is no common month in the data of 2014 with other data, it was not included in the study.

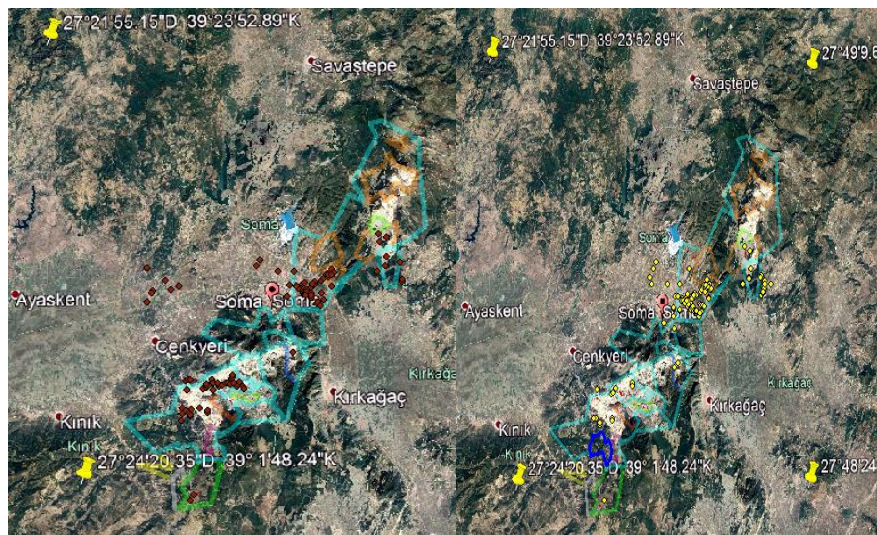


(a)

(b)

Figure 4.14: The SSI LST images from 7 years of Landsat 8 OLI/TIRS LST data using Band 10 (a) and Band 11 (b)

The next application in which the reliability of land surface temperature (LST) images is investigated is accuracy analysis, and it has been applied to SSI images obtained from 18 Landsat 8 OLI/TIRS land surface temperature (LST) data via ArcGIS data processing program. The results of the assessment analysis for hot spots falling in Licensed Coal Mine Areas in Soma were received as 87% for Band 10 and 89% for Band 11. These results show that some Licensed Coal Mine Areas are under coal fire threat. In Figure 4.15, red and yellow dots represent the threshold pixel distribution of Landsat 8 SSI LST values from Band 10 and Band 11.



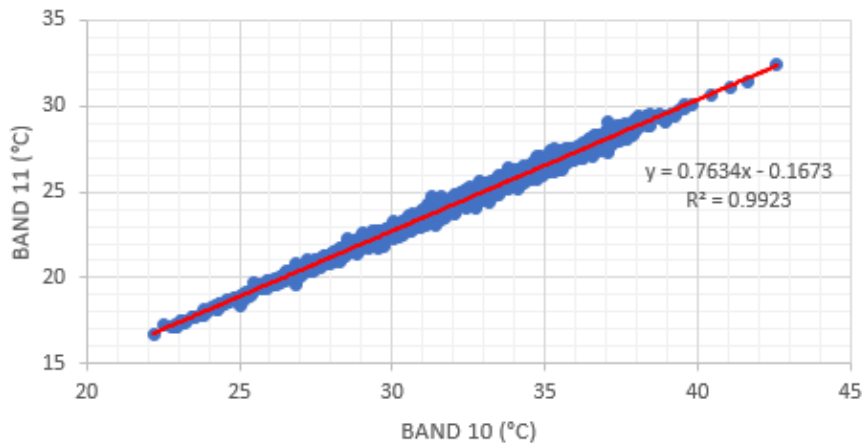
(a)

(b)

Figure 4.15: Assessment of licensed coal mine areas in Soma under coal fire threat by Landsat 8 OLI/TIRS SSI Data using Band 10 (red dots) (a) and Band 11 (yellow dots) (b)

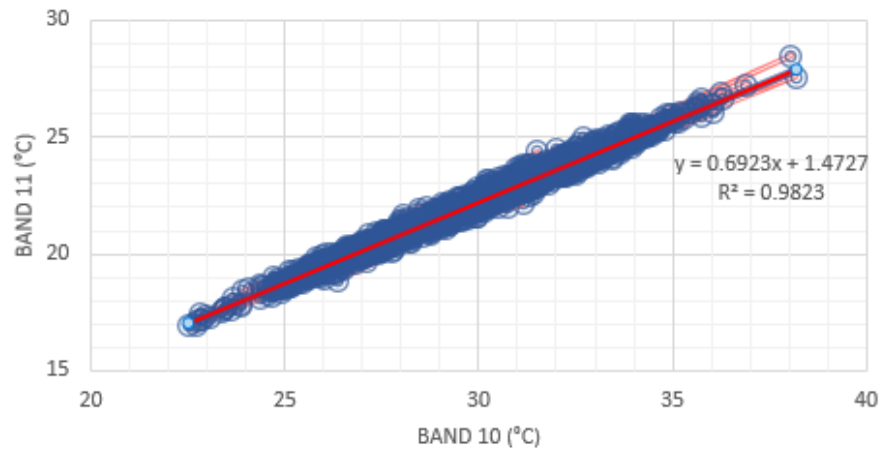


**Landsat 8 LST Correlation Graphic in °C**



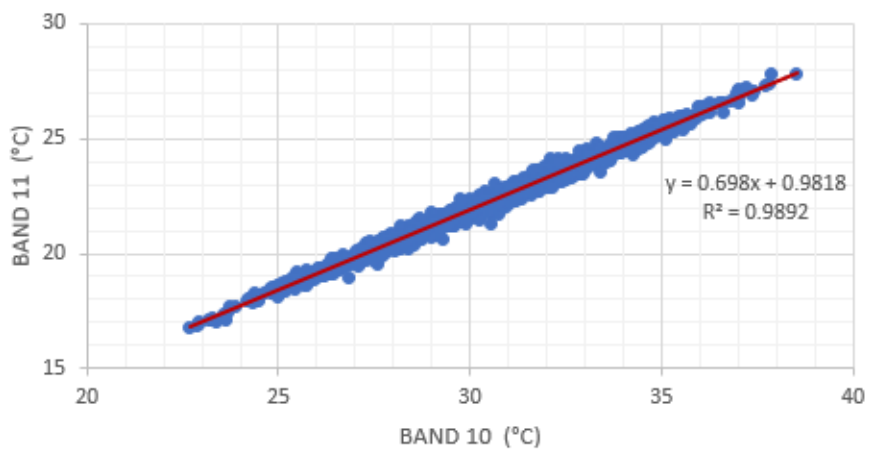
(a)

**Landsat 8 LST Correlation Graphic in °C**



(b)

**Landsat 8 LST Correlation Graphic in °C**



(c)

Figure 4.16: The Correlation Graphics of the 3 Landsat 8 OLI/TIRS Land Surface Temperature (LST) Data (a) 20130721, (b) 20160729 and (c) 20190731

Finally, for the accuracy analyses of the results above, the correlation between Landsat 8 OLI/TIRS land surface temperature (LST) data from Band 10 and Band 11 (Figure 4.15 a and b) were visualized by creating correlation graphics on excel. For this stage, 3 Landsat 8 OLI/TIRS land surface temperature (LST) data were selected. The root mean square values and correlation equations between the data were also modelled. These accuracy graphics have shown that there is a balanced distribution between the accuracy of the land surface temperature (LST) data obtained by processing the Landsat 8 OLI/TIRS Band 10 and Band 11 thermal bands data.

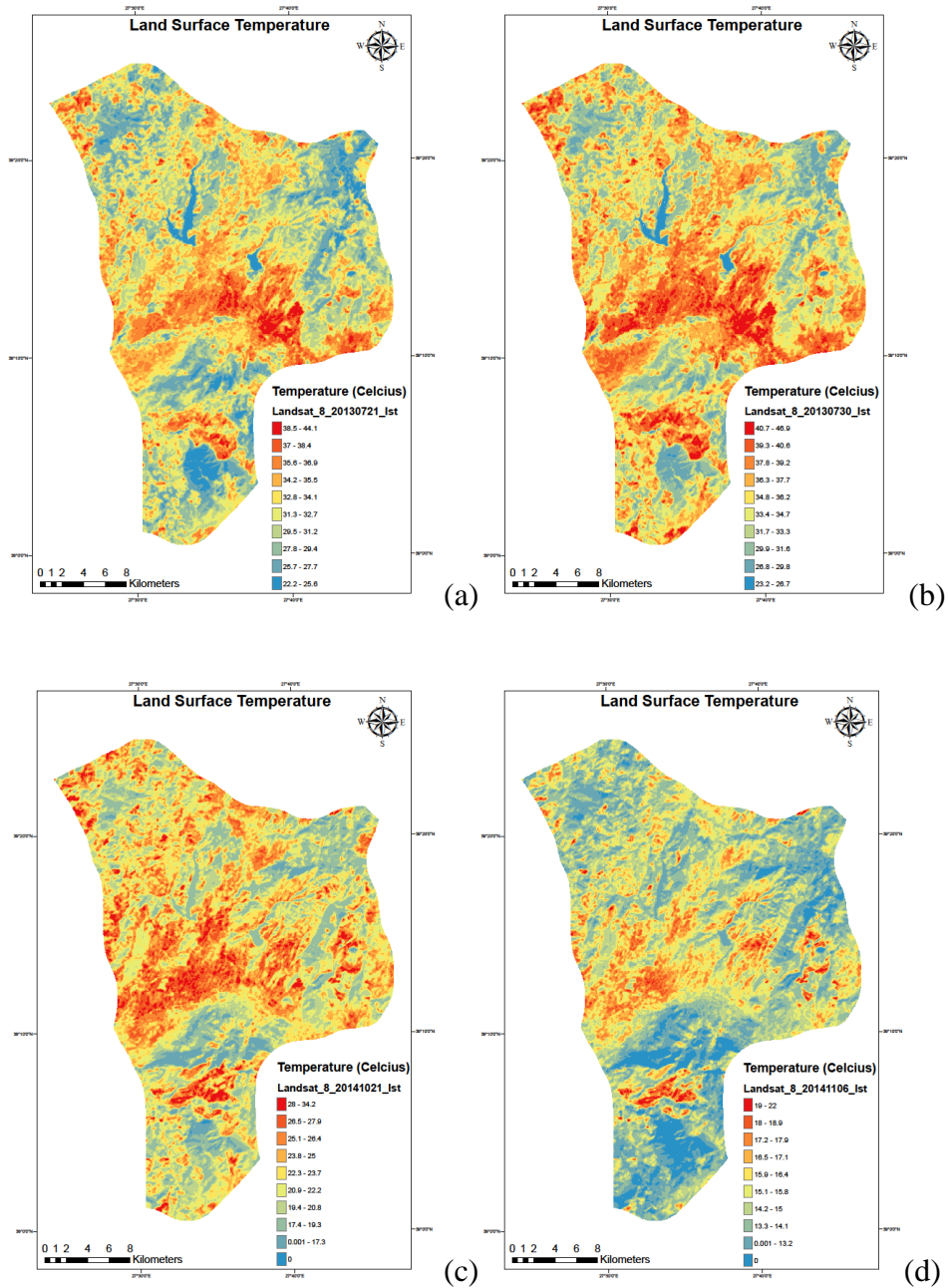
# Chapter 5

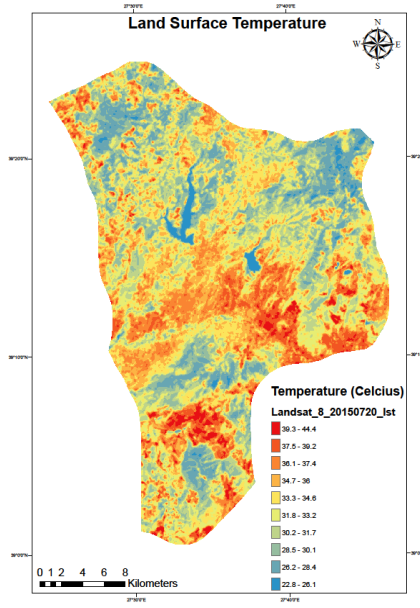
## Results and Discussions

The aim of this study was to determine and examine the coal fires that occur in the coal mines of Soma by using the Landsat satellite bands and especially thermal band data collected by remote sensing techniques. 25 Landsat 5 TM and 23 Landsat 8 OLI/TIRS satellite data were downloaded from USGS website as geometrically corrected. The downloaded Landsat satellite data were daytime data and these data were detected by Landsat satellite sensors between 08:00 and 10:00 time interval. Firstly, radiometric corrections were applied to the Landsat 5 TM and Landsat 8 OLI/TIRS satellite data to prepare these data to data processing. Thus, the data preparation process of this study was completed, the data was made processable and the data processing step started. A single channel algorithm was chosen for the retrieval of land surface temperatures (LST). This algorithm was modeled both for the Landsat 5 TM and Landsat 8 OLI/TIRS satellite data by using ERDAS Imagine 2014 data processing program. Normalized difference vegetation indexes (NDVI) of the Landsat 5 TM and Landsat 8 OLI/TIRS satellite data were calculated.

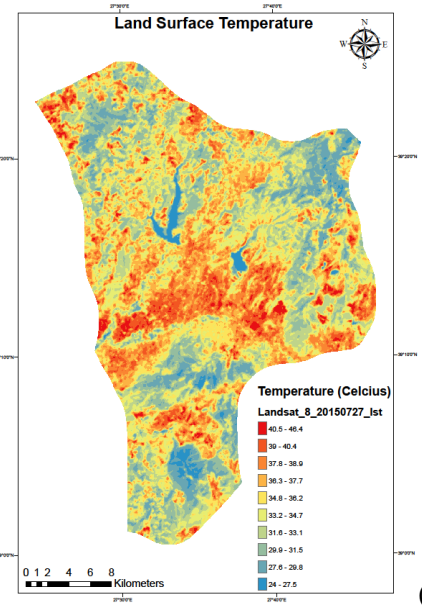
After that, land surface emissivities (LSE) of the Landsat 5 TM and Landsat 8 OLI/TIRS satellite data were estimated. Finally, the land surface temperatures (LST) were retrieved. The Landsat 5 TM land surface temperature (LST) data results were unworkable, so these data were eliminated from the study. The SSI images of Landsat 8 OLI/TIRS land surface temperature (LST) data were created for both Band 10 and Band 11 thermal band data. The accuracy of the created land surface temperature (LST) and SSI image values were evaluated with various analyzes. At the end of the study, the 3-period coal fire maps were made from Landsat 8 OLI/TIRS data with Band 10 to detect and monitor coal fires in the study area temporally.

The maps of 18 Landsat 8 OLI/TIRS land surface temperature (LST) data with Band 10 were prepared and shown in Figure 5.1 below. In Figure 5.2, the map of Landsat 8 OLI/TIRS SSI image, which were produced from 18 Landsat 8 OLI/TIRS land surface temperature (LST) data with Band 10, was presented. Besides, the map of Landsat 8 OLI/TIRS SSI image, which were formed from 7 Landsat 8 OLI/TIRS land surface temperature (LST) data with Band 10 was given in Figure 5.3.

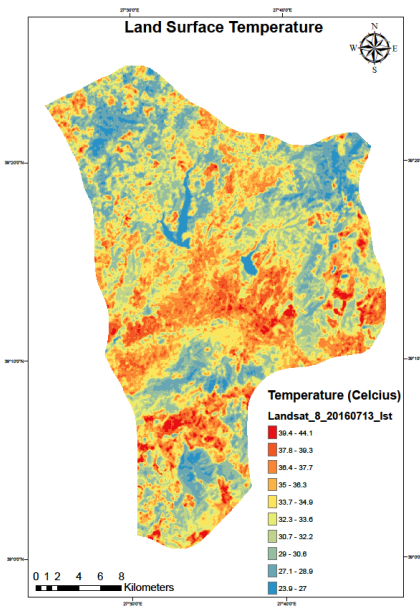




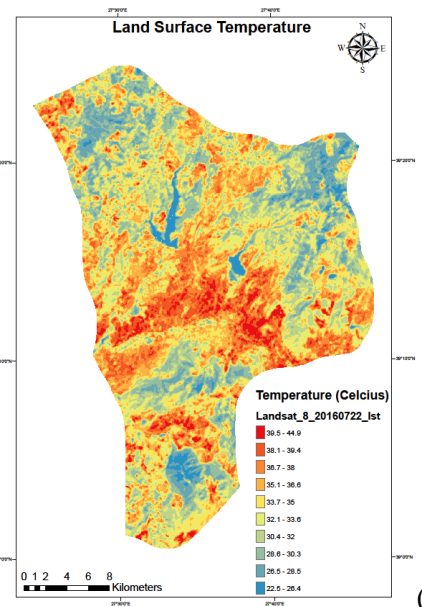
(e)



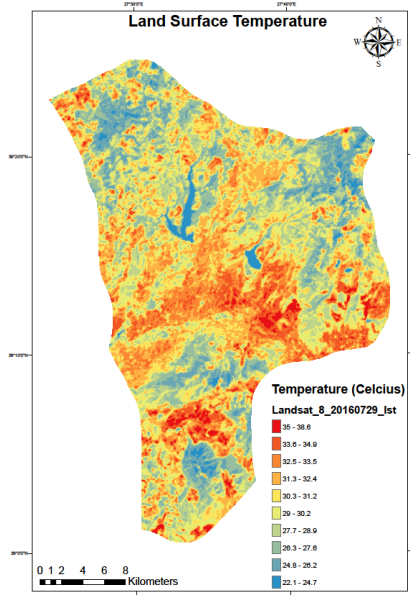
(f)



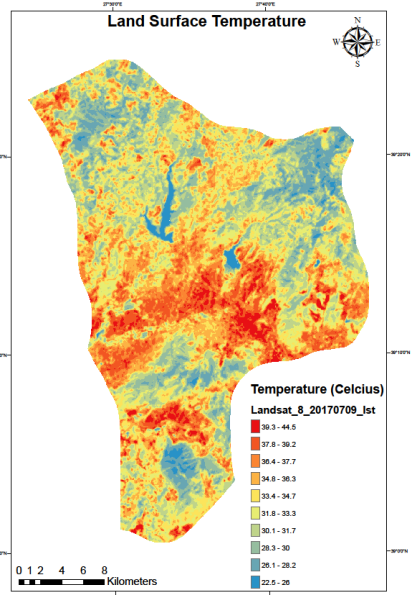
(g)



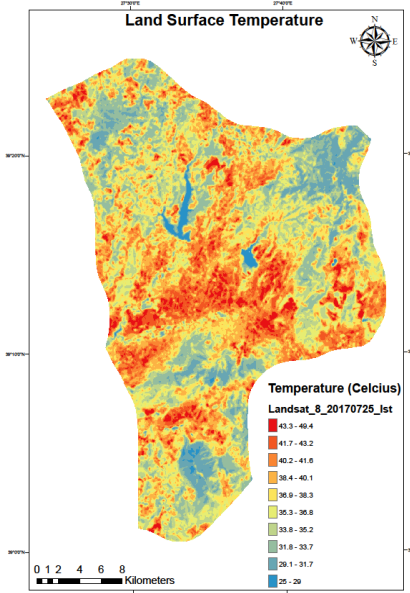
(h)



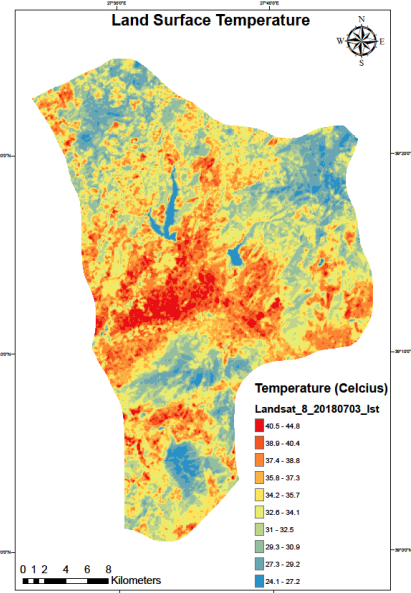
(i)



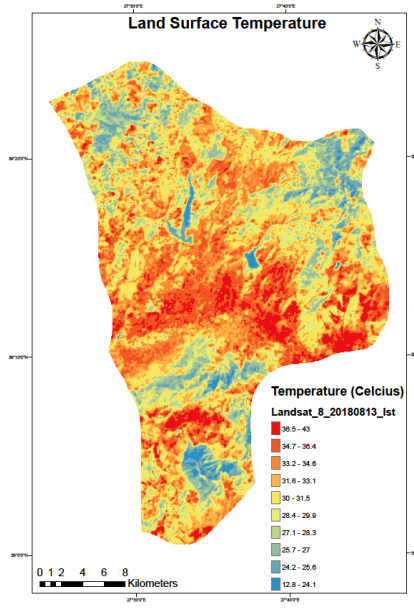
(j)



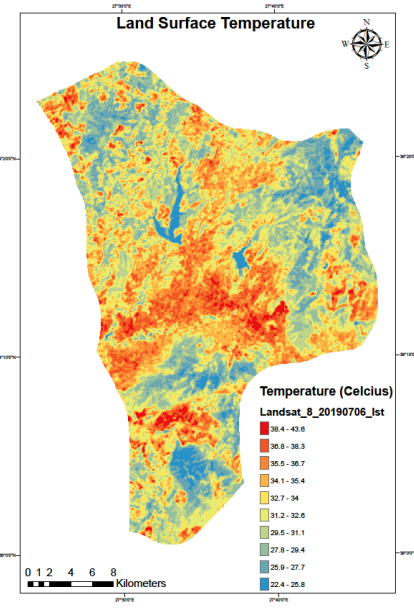
(k)



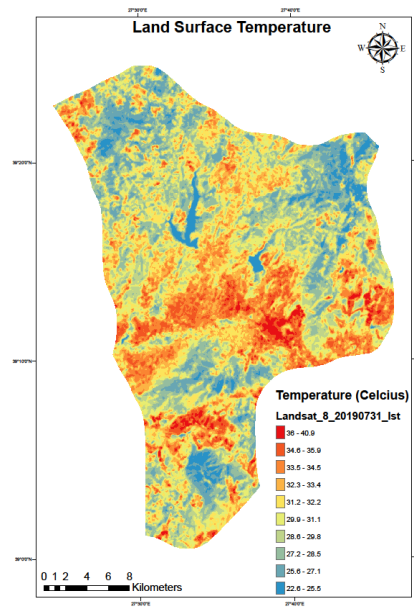
(l)



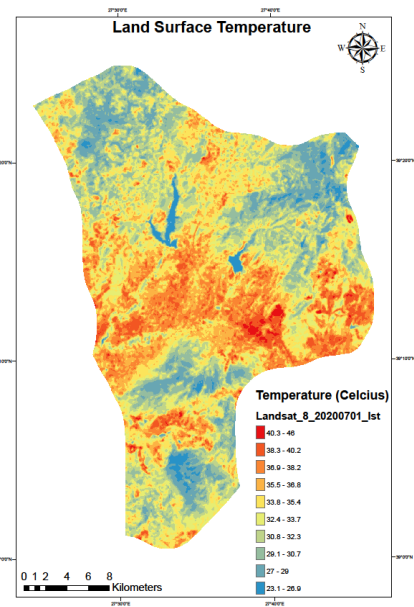
(m)



(n)



(o)



(p)

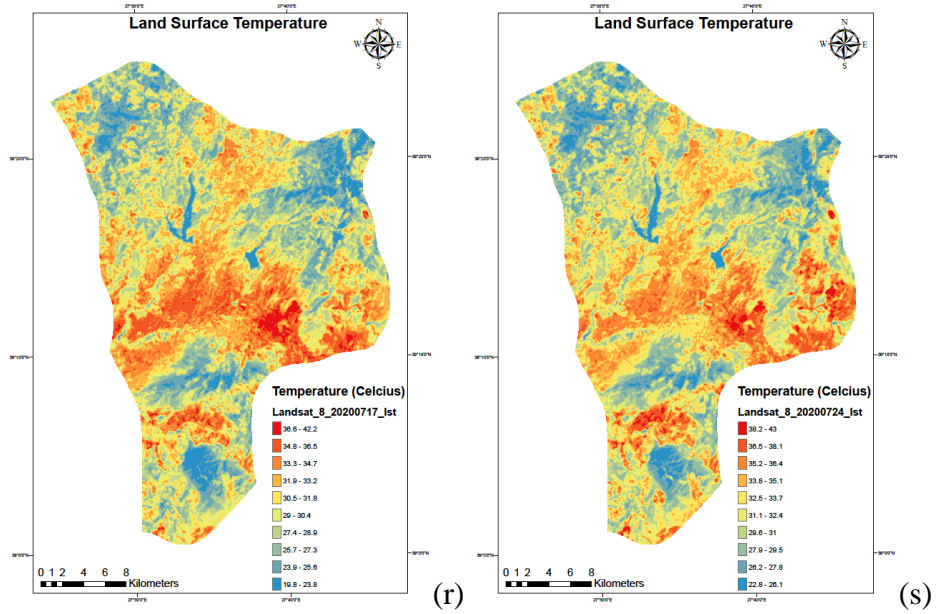


Figure 5.1: The land surface temperature (LST) maps of 18 Landsat 8 OLI/TIRS data with Band 10 (a) 2013.07.21, (b) 2013.07.30, (c) 2014.10.21, (d) 2014.11.06, (e) 2015.07.20, (f) 2015.07.27, (g) 2016.07.13, (h) 2016.07.22, (i) 2016.07.29 (j) 2017.07.09, (k) 2017.07.25, (l) 2018.07.03, (m) 2018.08.13, (n) 2019.07.06, (o) 2019.07.31, (p) 2020.07.01, (r) 2020.07.17, and (s) 2020.07.24

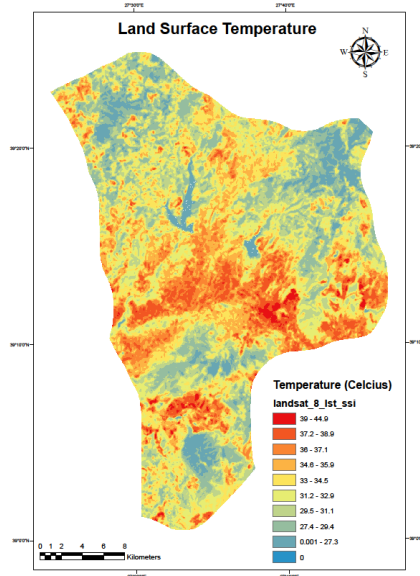


Figure 5.2: The map of Landsat 8 OLI/TIRS SSI image which were produced from 18 Landsat 8 OLI/TIRS land surface temperature (LST) data with Band 10



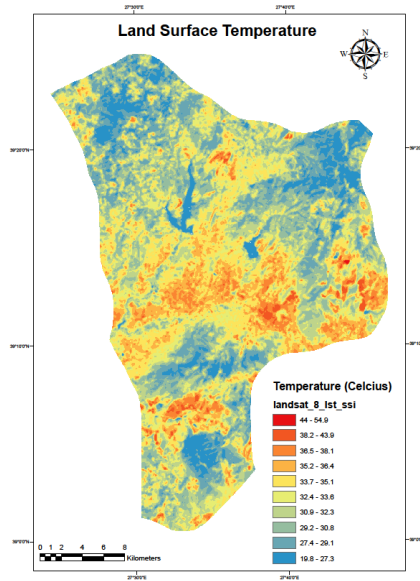
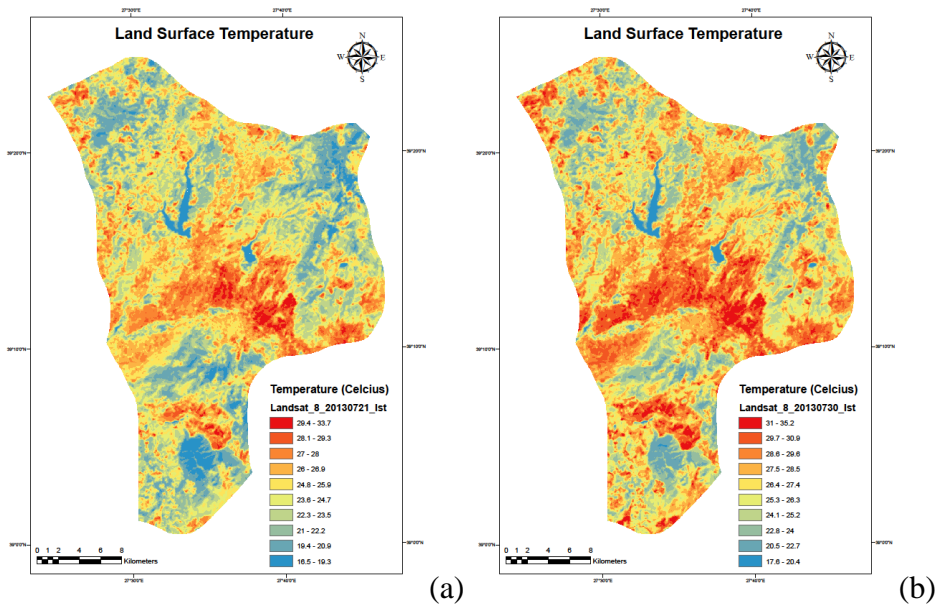
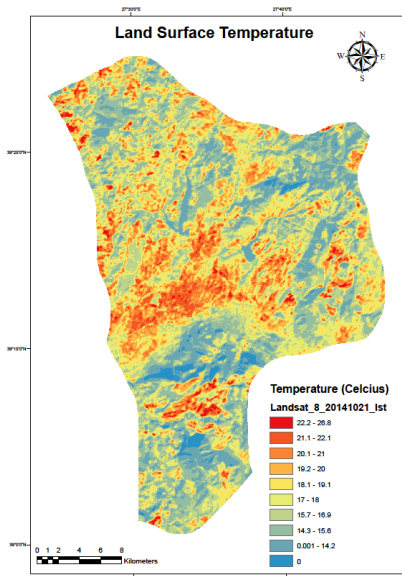


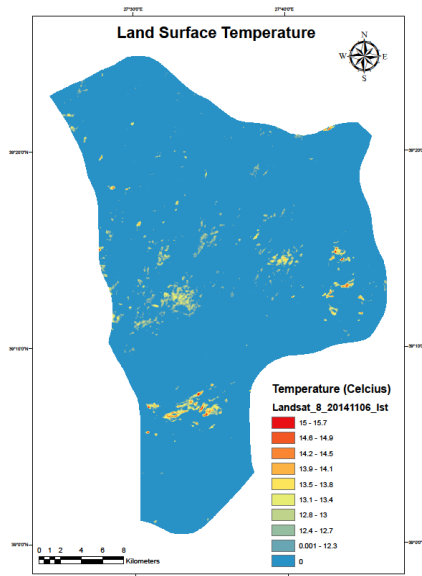
Figure 5.3: The map of Landsat 8 OLI/TIRS SSI image which were produced from 7 Landsat 8 OLI/TIRS land surface temperature (LST) data with Band 10

The maps of 18 Landsat 8 OLI/TIRS land surface temperature (LST) data with Band 11 were prepared and shown in Figure 5.4 below. In Figure 5.5, the map of Landsat 8 OLI/TIRS SSI image which were produced from 18 Landsat 8 OLI/TIRS land surface temperature (LST) data with Band 11 was presented. Also, the map of Landsat 8 OLI/TIRS SSI image which were formed from 7 Landsat 8 OLI/TIRS land surface temperature (LST) data with Band 11 was given in Figure 5.6.

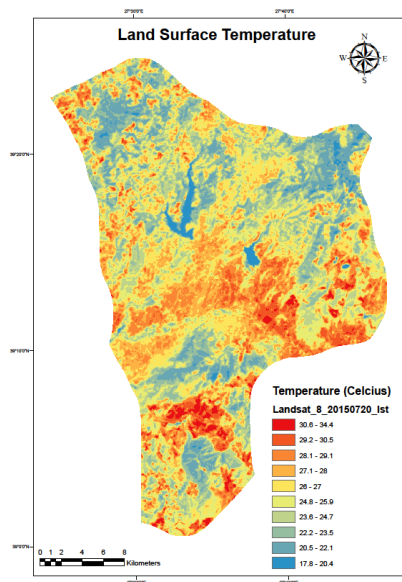




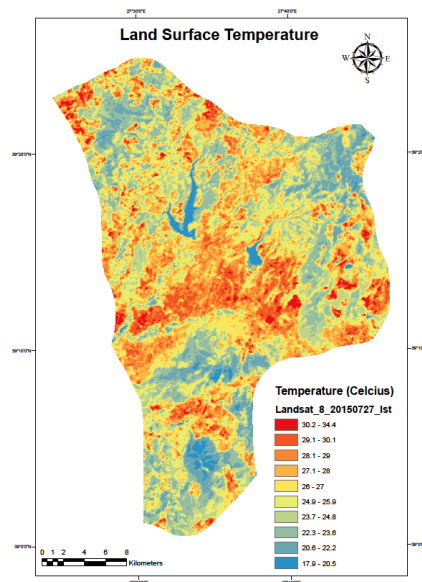
(c)



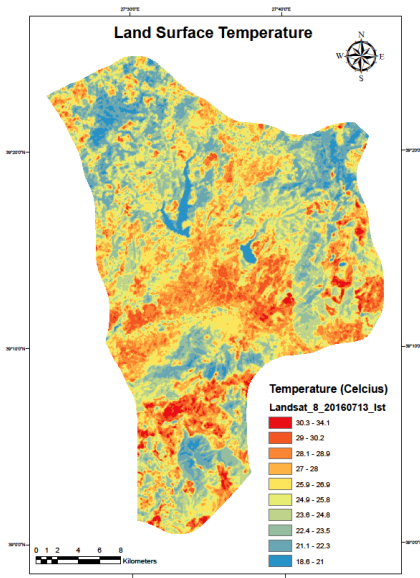
(d)



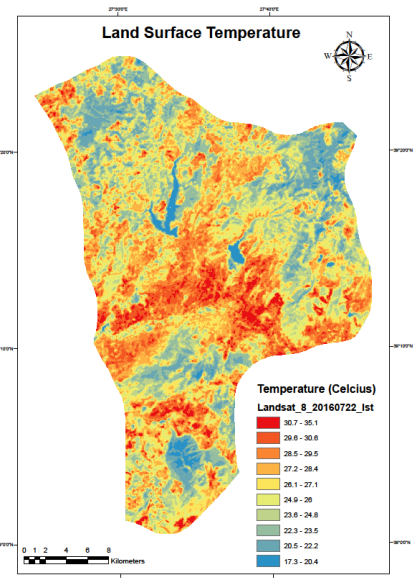
(e)



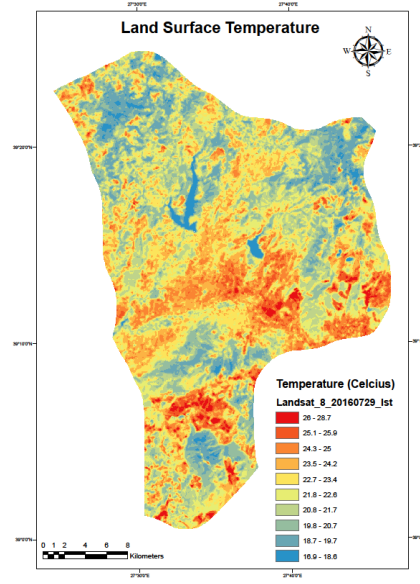
(f)



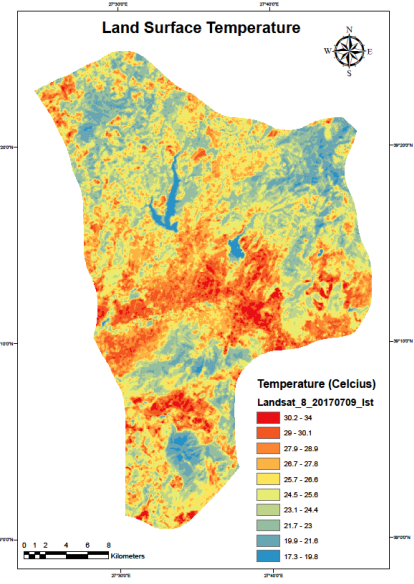
(g)



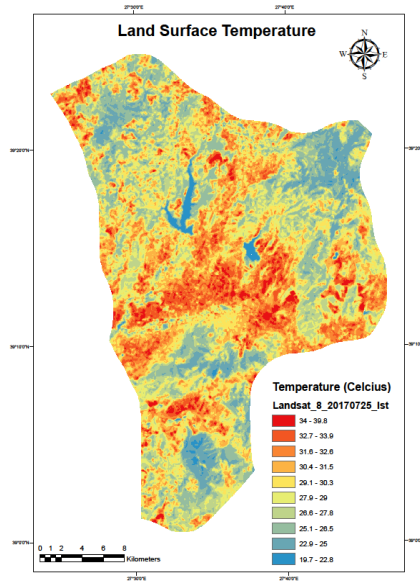
(h)



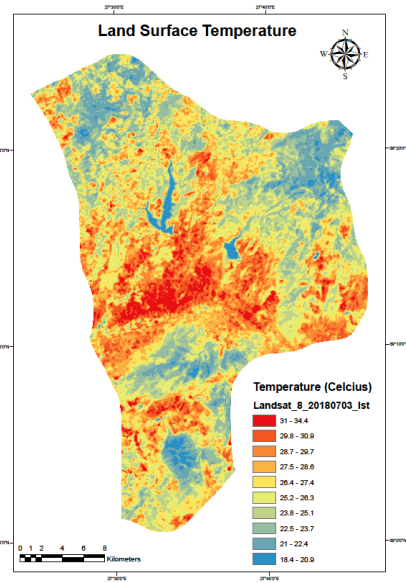
(i)



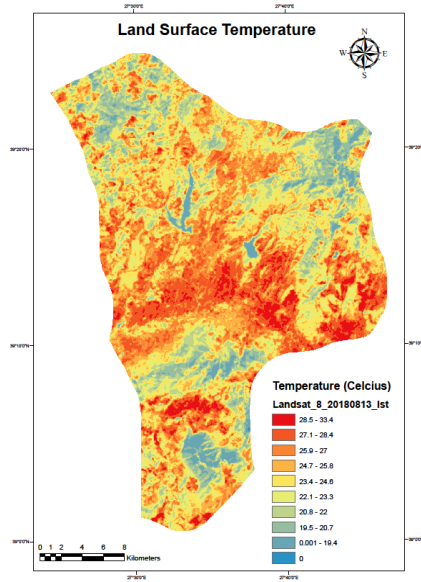
(j)



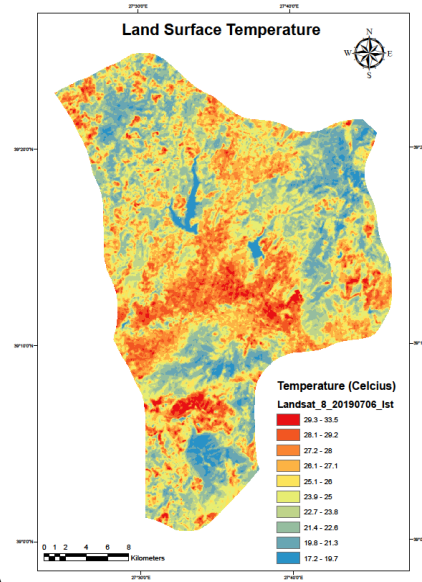
(k)



(l)



(m)



(n)

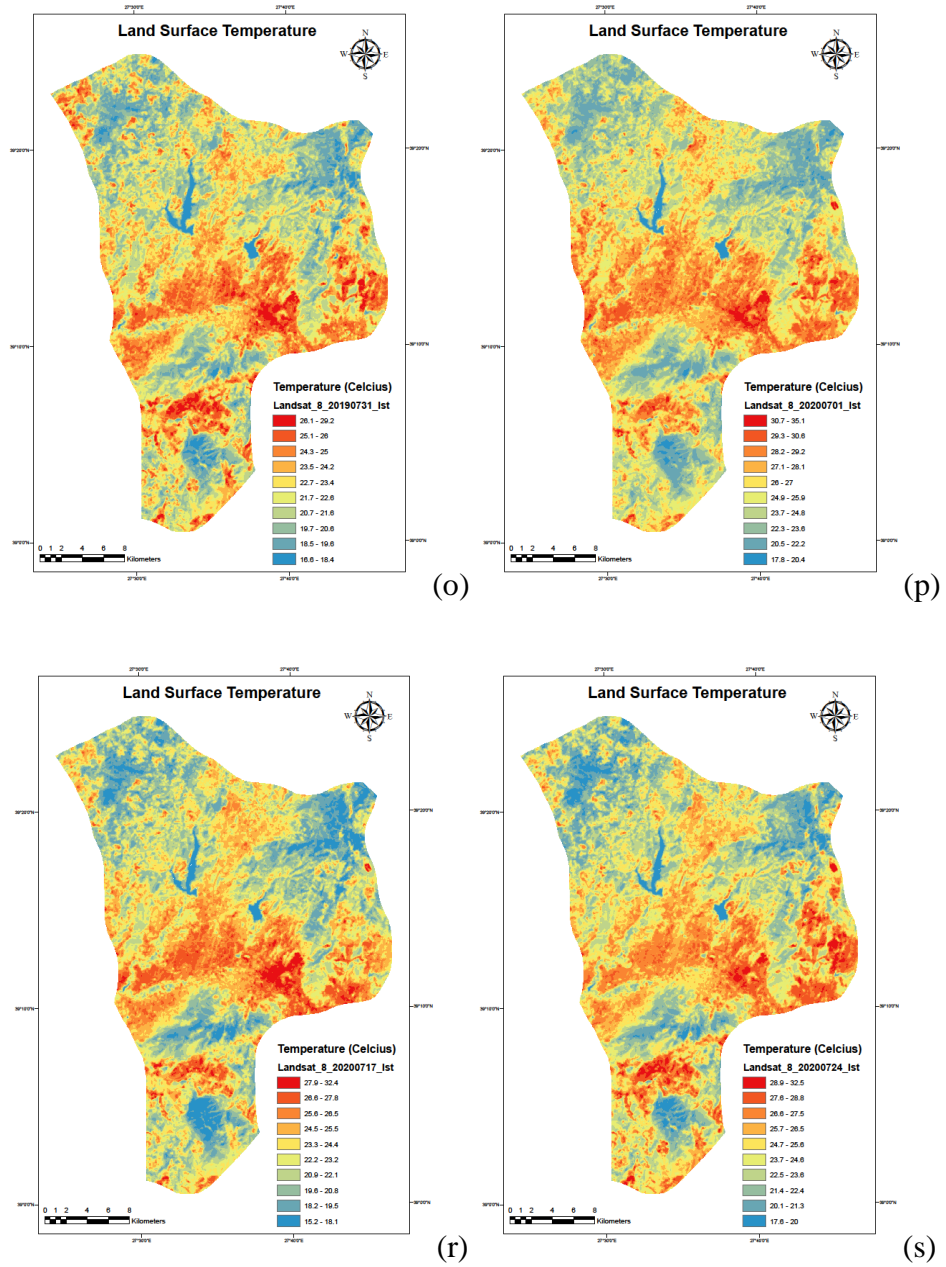


Figure 5.4: The land surface temperature (LST) maps of 18 Landsat 8 OLI/TIRS data with Band 11 (a) 2013.07.21, (b) 2013.07.30, (c) 2014.10.21, (d) 2014.11.06, (e) 2015.07.20, (f) 2015.07.27, (g) 2016.07.13, (h) 2016.07.22, (i) 2016.07.29 (j) 2017.07.09, (k) 2017.07.25, (l) 2018.07.03, (m) 2018.08.13, (n) 2019.07.06, (o) 2019.07.31, (p) 2020.07.01, (r) 2020.07.17, and (s) 2020.07.24

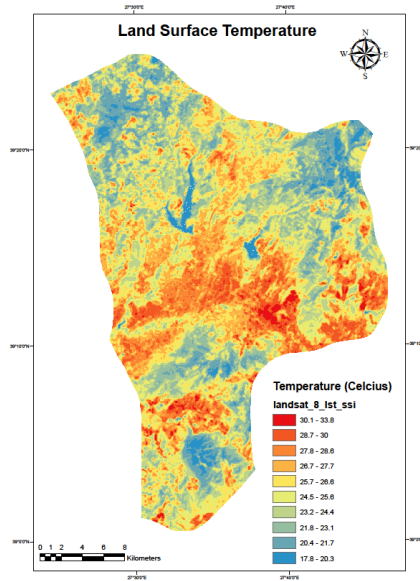


Figure 5.5: The map of Landsat 8 OLI/TIRS SSI image which were produced from 18 Landsat 8 OLI/TIRS land surface temperature (LST) data with Band 11

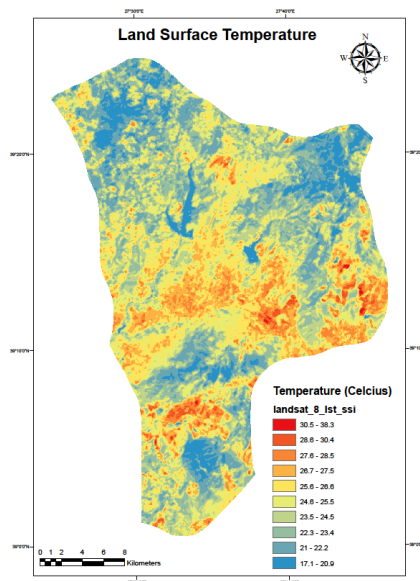
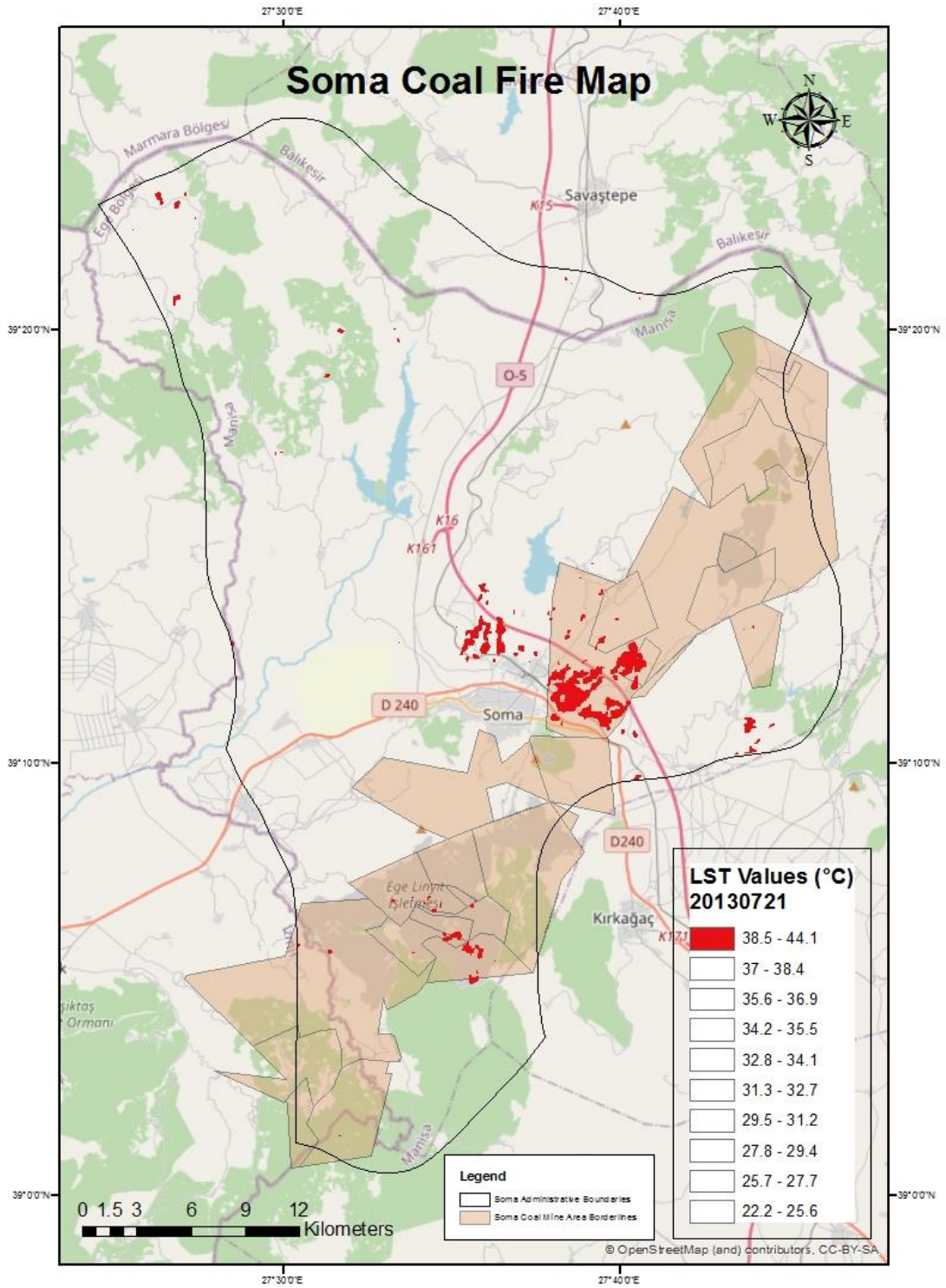
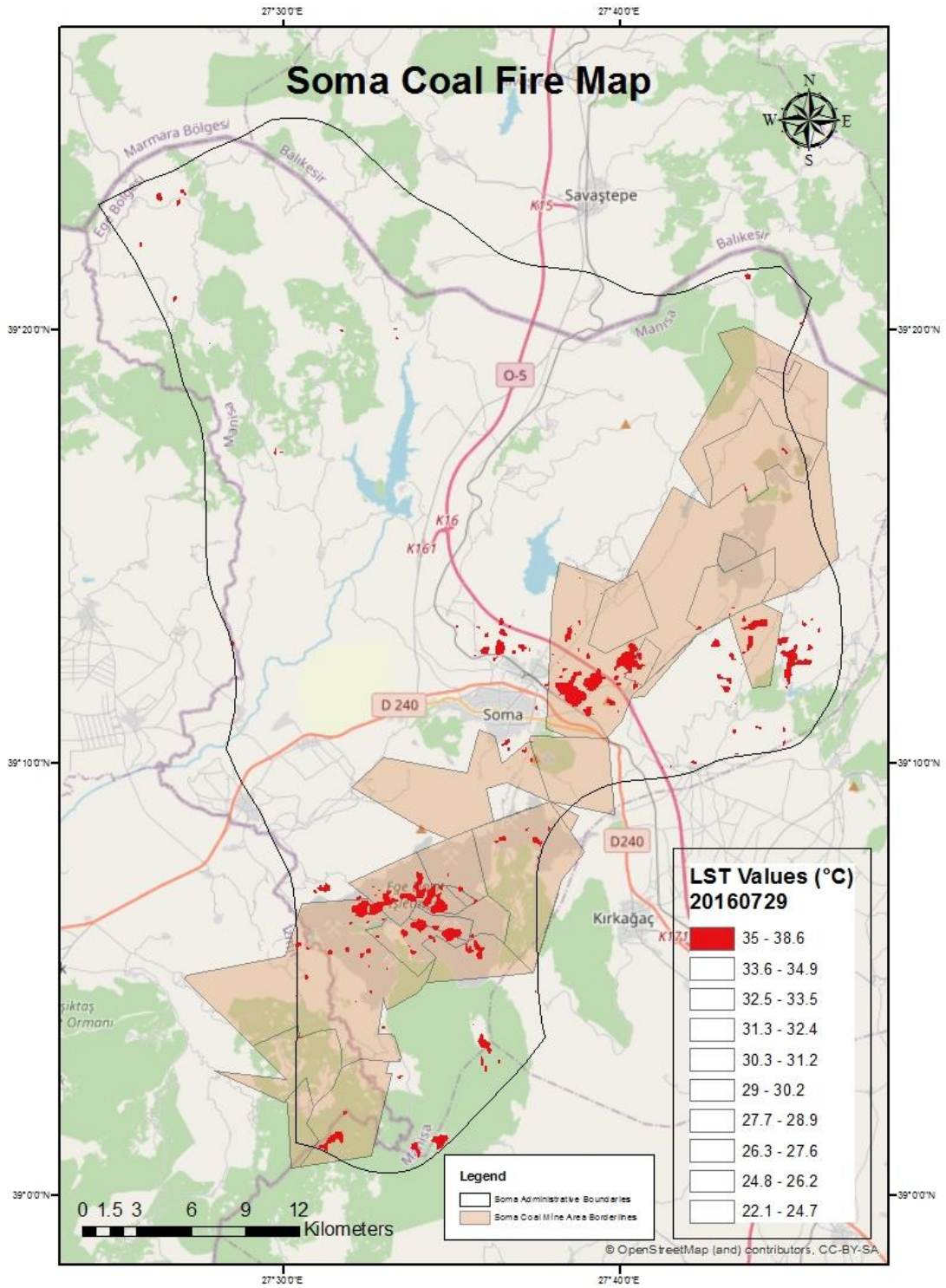


Figure 5.6: The map of Landsat 8 OLI/TIRS SSI image which were produced from 7 Landsat 8 OLI/TIRS land surface temperature (LST) data with Band 11

Finally, three different Landsat 8 OLI/TIRS land surface temperature (LST) data with Band 10 were chosen for analyzing the possibility of coal fires in the study area by depending on the time factor. These data were investigated according to 3-year intervals: 2013.07.21, 2016.07.29 and 2020.07.31 and coal fire maps were made by including the administrative boundaries of Soma and the licenced coal mine extraction area borders. The coal fire maps are shown in Figure 5.7 below.

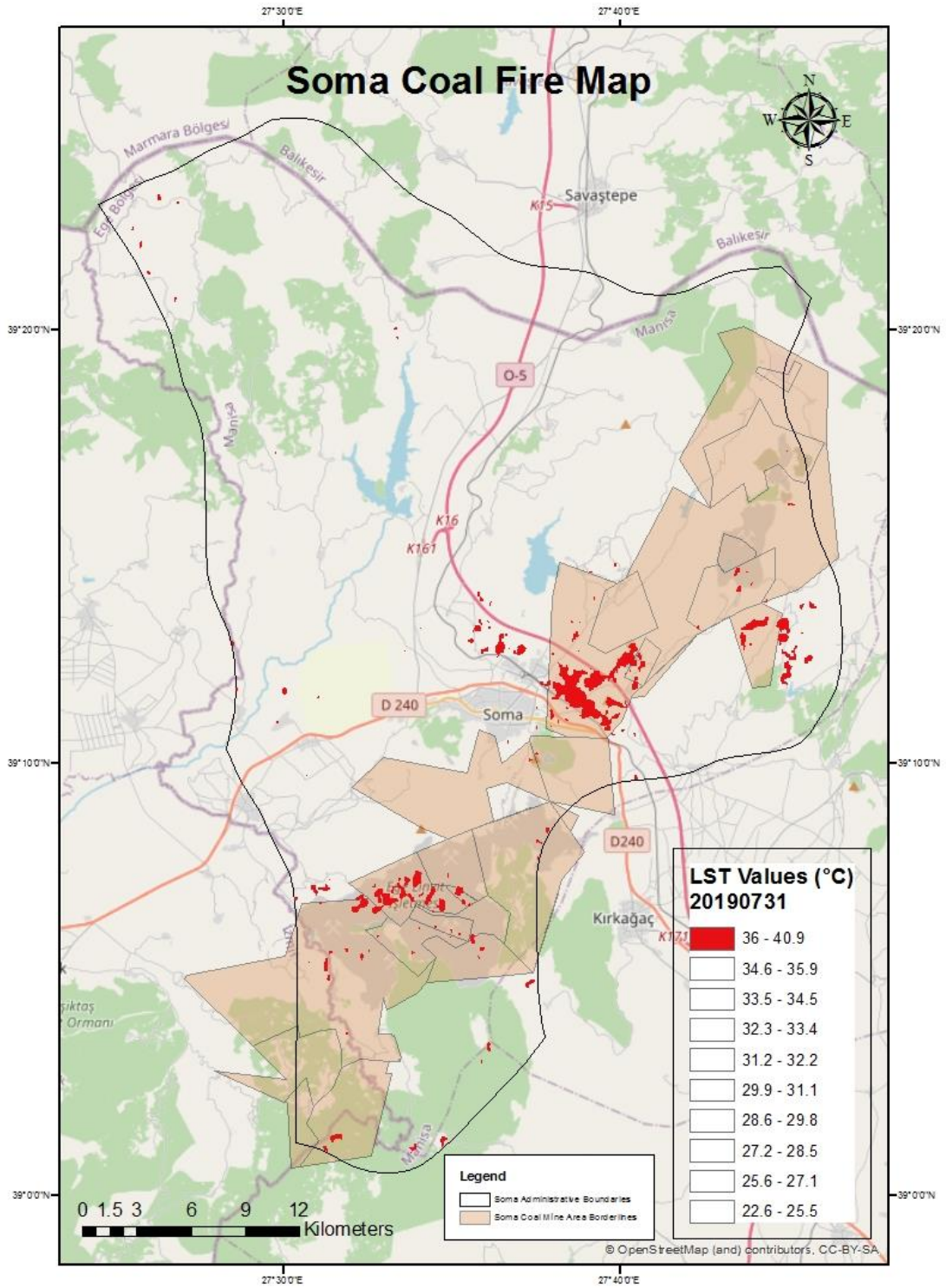


(a)



(b)





(c)

Figure 5.7: The three coal fire maps of Soma (a) 20130721, (b) 20160729 and (c) 20190731

The relationship between the pixels obtained from The Landsat 8 SSI LST Band 10 threshold value analysis (10-15%) and the threshold value pixels in the Landsat 8 LST Band 10 images belonging to three different years (2013.07.21, 2016.07.29 and 2019.07.31) was examined. The following results were found:

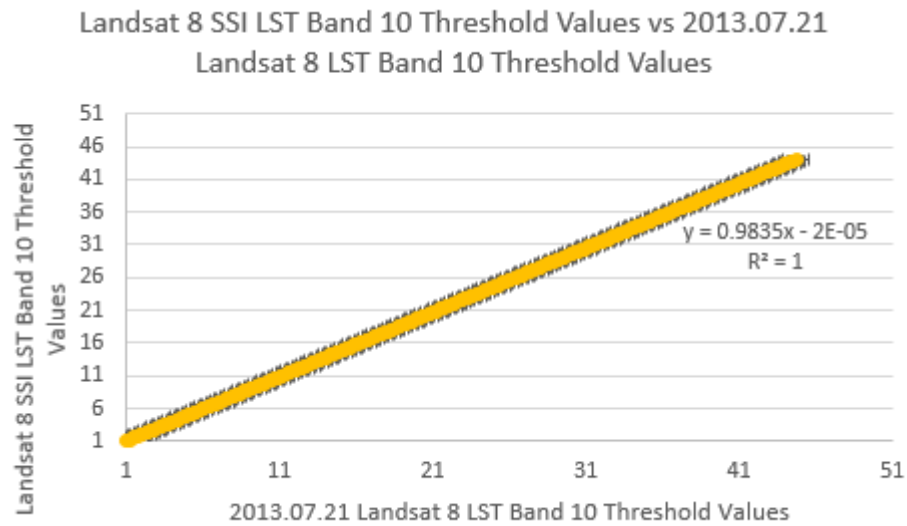


Figure 5.8: The Correlation Graphic of the Landsat 8 SSI LST Band 10 Threshold Values and the 2013.07.21 Landsat 8 LST Band 10 Threshold Values

- The correlation between the Landsat 8 SSI LST Band 10 threshold image values and the 2013.07.21 Landsat 8 LST Band 10 threshold image values is approximately % 98.35 percent.

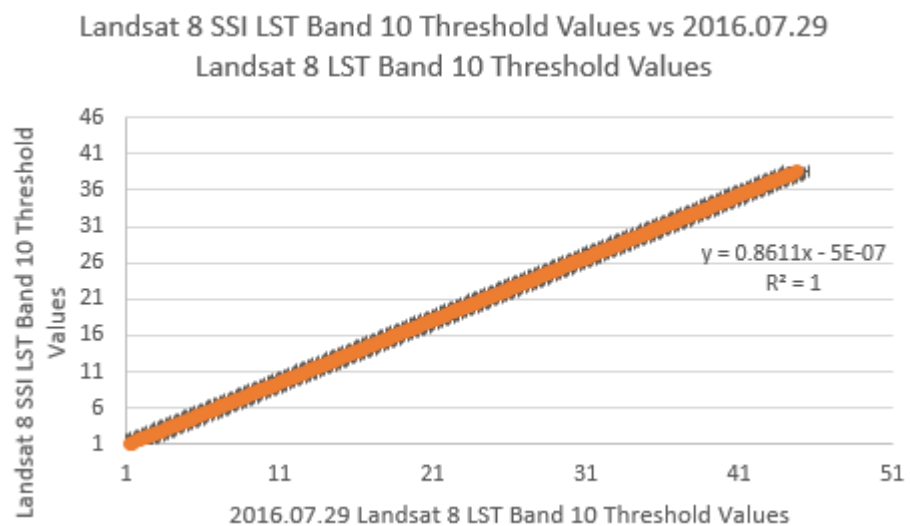


Figure 5.9: The Correlation Graphic of the Landsat 8 SSI LST Band 10 Threshold Values and the 2016.07.29 Landsat 8 LST Band 10 Threshold Values

- The correlation between the Landsat 8 SSI LST Band 10 threshold image values and the 2016.07.29 Landsat 8 LST Band 10 threshold image values is approximately % 86.11 percent.

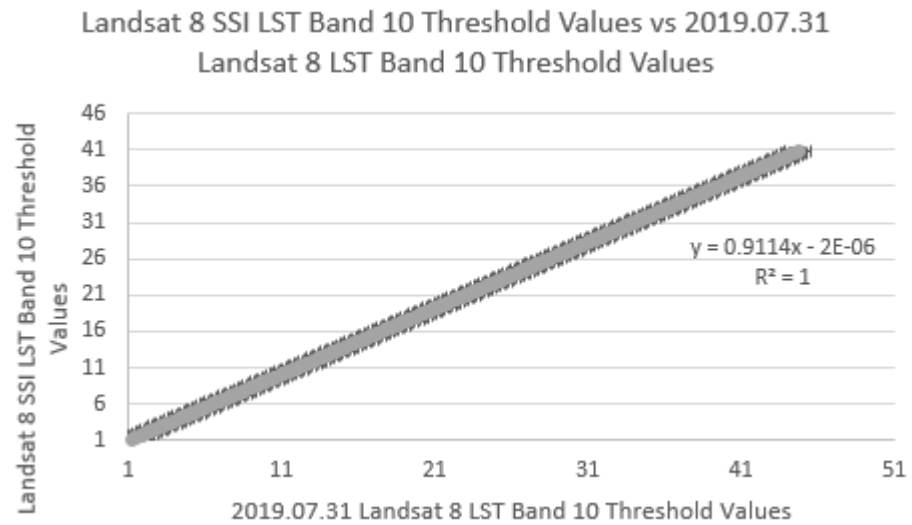


Figure 5.10: The Correlation Graphic of the Landsat 8 SSI LST Band 10 Threshold Values and the 2019.07.31 Landsat 8 LST Band 10 Threshold Values

- The correlation between the Landsat 8 SSI LST Band 10 threshold image values and the 2019.07.31 Landsat 8 LST Band 10 threshold image values is approximately % 91.11 percent.

Thus, it has been proven that without analyzing each image one by one, a high correlation can be achieved with only the produced SSI image. Also, according to the Landsat 8 SSI LST Band 10 threshold image data, there are a total of 6303 pixels falling into the coal mine area. This number was determined as 9838 in the 2013.07.21 Landsat 8 LST Band 10 threshold image data, 12244 in the 2016.07.29 Landsat 8 LST Band 10 threshold image data and 10901 in the 2019.07.31 Landsat 8 LST Band 10 threshold image data. It is seen that this variable situation may have taken pixels other than possible fire pixels as a result of examining the threshold value images of three different years.

As a result of the interpretation of the created coal fire maps, it can be emphasized that the potential coal fire areas shown in red are within the Soma licensed coal mine extraction areas shown in light orange in Figure 5.7. The reasons for the detection of hot spot areas in high temperature observed in areas without coal mine extraction areas

can be counted as the proximity of these areas to the city center and places where industrial activities are common. In places with low NDVI value, such as bare soil areas, the land surface temperature (LST) values were high, and in places with high NDVI value, such as forests and densely vegetated areas, the land surface temperature (LST) values were very low.

According to the findings obtained as a result of the operations, the land surface temperature (LST) data obtained by using Landsat 8 Band 10 data were examined, and it was determined that the locations of the high temperature areas with the possibility of coal fires were similar to the data obtained by processing Landsat 8 Band 11 data. In order to easily distinguish possible coal fire areas, threshold values (LST) were determined according to the current relative land surface temperature values of the land. The range of these threshold values is between highest % 10-15 of LST values in the whole region, and each pixel exceeding the threshold was perceived as indicating a possible coal fire.

There are a number of differences in the coal fire maps mapped at three-year intervals above. Among the primary reasons for these differences are the acquisition dates of Landsat satellite data, changing weather conditions, regional division of land cover into several classes, terrain types, thermal radiation affecting the land surface temperature (LST), underground coal fire burning situations, background temperatures of the study area, and so on. Some fire areas may not be noticed due to seasonal changes. The spatial resolution of thermal image data is a significant factor for determining the potential coal fire areas accurately. Landsat 8 OLI/TIRS thermal bands (Band 10 and Band 11) with 100 m spatial resolution were used for the study so that the areas smaller than 100x100 m SSA on the ground couldn't be identified.

The Landsat 8 SSI Band 10 threshold coal fire pixel data, 20130721 Band 10 threshold coal fire pixel data, 20160729 Band 10 threshold coal fire pixel data, and 20190731 Band 10 threshold coal fire pixel data were converted to .kmz format by using ArcGIS program to be opened on Google Earth application. It has been determined that the threshold coal fire pixels data were located on the Kırakdere Open Pit Coal Mine area in Soma (Figure 5.11).



(a)

(b)



(c)

(d)

Figure 5.11: The Google Earth display of Soma open pit mine and matching threshold coal fire pixels of (a) SSI Band 10 Threshold data, (b) 20130721, (c) 20160729 and (d) 20190731

# Chapter 6

## Conclusions

Coal is a substance found in many countries, including our country, and is extracted from coal mines to obtain energy and to meet similar needs. The Soma district of Manisa province is also rich in coal reserves, and coal extraction has been done here for many years. Coal can be in the depths or surface of coal mines. Coal combustion can occur as a result of the extraction of coal from underground by various mining activities or while at the surface of the coal mine. Coal fire is an event that occurs due to contact with air (oxygen) and releases heat, and for this reason, temperatures higher than normal air temperatures can often be observed in areas where coal fires are experienced. Coal fires are very dangerous both for the area they are in and for the lives of people, and the locations of these fires must be identified and intervened upon, so the damage caused by the coal fires must be minimized. There are a number of tools and methods that can be used to detect coal fires. Field measurements made by applying field measurement methods in the coal mine areas provide a lot of information about the land temperatures of the area. However, remote sensing methods have started to be preferred with the fact that both the field measurements take a long time and cannot be easily performed in large areas, and the technology has gradually developed. It is estimated that the use of remote sensing technology in combination with geophysical methods in studies to be conducted on this subject will greatly increase the accuracy of the results.

The main purpose of this thesis is to detect coal fires, which are caused by the contact of coal with oxygen in the coal mines in the Soma region and in the areas around the coal mines, by processing satellite images obtained by using remote sensing techniques. For this reason, Landsat 5 TM and Landsat 8 OLI/TIRS satellite image data were used. According to the results of the studies, Landsat 5 TM images were

excluded from this project because it was considered that the accuracy of the Landsat 5 TM LST images was not sufficient for this project. In this study, land surface temperatures were calculated with an algorithm which uses single thermal band data (a single channel algorithm). Landsat 8 OLI/TIRS Band 10 data is main data of the project. Since Landsat 5 TM data could not be used, Landsat 8 OLI/TIRS Band 11 data as a second data type was included in the project, and each operation made for Landsat 8 OLI/TIRS Band 10 was also applied to Landsat 8 OLI/TIRS Band 11 for validation.

A total of 23 Landsat 8 OLI/TIRS data has been downloaded. The date range of these data is between 2013 and 2020. Before Landsat 8 OLI/TIRS data is processed, it has been subjected to a preparation stage called preprocessing, and the brightness temperatures of the pixels are displayed. Afterwards, the land surface emissivities of Landsat 8 OLI/TIRS data were calculated by using NDVI. And finally, by retrieving the land surface temperatures (LST), the pixels with the highest temperature which is the sign of coal mine fires, were determined.

Each pixel is the smallest piece of data that represents the characteristic features of the geographic location it belongs to. The use of large amounts of data reveals the temporal change rate of the subject under investigation and contributes to the increase in the consistency and reliability of the data analysis. Therefore, the simulated single images (SSI) of Landsat 8 OLI/TIRS data with land surface temperatures were calculated. Threshold ranges (10-15%) of Landsat 8 LST SSI data were identified, as the pixel spacing with the highest temperature may represent the places where coal mine fires occur and spread. Normalized Landsat 8 LST SSI values were found for both Band 10 and Band 11 in order to easily interpret the Landsat 8 LST SSI threshold data. Afterwards, these two data groups were overlapped to find out how accurate the Normalized Landsat 8 LST SSI Band 10 and Band 11 threshold values were. This method is quite necessary since field work cannot be done. As a result of this study, it was seen that the threshold values of Band 10 and Band 11 generally have the same pixels. In another application, it has been observed that Band 10 and Band 11 threshold pixels contain many common pixels corresponding to the Soma coal mines region. Accuracy and correlation analyses of Landsat 8 LST, Normalized Landsat 8 LST SSI, and Normalized Landsat 8 LST SSI Band 10 and Band 11 threshold data were made, and it was deduced that the two data types gave consistent results with each other.

Finally, coal mine fire maps were made with 3-year Landsat 8 LST Band 10 threshold data and the areas under the influence of possible coal mine fires were given visually.

Landsat 8 LST SSI Band 10 images obtained by combining 18 Landsat 8 LST Band 10 images were examined, and it was determined that this image has higher accuracy (about %64.07 percent) than other 18 Landsat 8 LST Band 10 images in determining the location of the fire pixels thought to belong to the fire areas. Normalized images of these images were created, and by this means, the temperature values were reduced to a certain range and data interpretation could be done easily.

The Landsat 8 SSI LST Band 10 data is a highly preferable data type compared to the 7 Landsat 8 LST SSI image obtained in the same month (July), because 7 Landsat 8 LST SSI image was formed by the combination of 7 Landsat 8 LST Band 10 data and these were insufficient in the detection process of fire pixels. In addition, in the 7 Landsat LST SSI Band 10 image, which consisted of not enough data groups, it was observed that there were also very high temperatures in the areas far outside the mining areas, which made the detection of mine fires difficult. In this study, the comparison of Band 10 and Band 11 bands, which are thermal bands, was also made using Landsat 8 OLI/TIRS data, and Band 10 data outperformed Band 11.



# References

- [1] Levine JR. Coalification: the evolution of coal as source rock and reservoir rock for oil and gas: Chapter 3.
- [2] World Coal Institute. The coal resource: A comprehensive overview of coal. Coal Resource Overview of Coal Report. 2005;1:1-4.
- [3] Chen Y, Liao S, Qin D. Study on inversion of coal seam temperature in mining area--Pingshuo mining area of Shanxi Province. InE3S Web of Conferences 2020 (Vol. 165, p. 03014). EDP Sciences.
- [4] Tomlinson T. Coal fires: an Environmental Disaster.
- [5] Schmal D, Duyzer JH, van Heuven JW. A model for the spontaneous heating of coal. Fuel. 1985 Jul 1;64(7):963-72.
- [6] Ozdeniz AH, Corumluoglu O, Kalayci I, Sensogut C. 3.5 D temperature model of a coal stockpile. Energy Sources, Part A. 2008 Apr 14;30(12):1085-97.
- [7] Zhang J., Zhongdan, H., Mei, Wang, Yaling, X., 2005. 3D Detection and visualization of underground coal fires. ERSEC Ecological Book Series 4, International Conference on Spontaneous coal seam fires: Mitigating a global disaster at Beijing PR China. November 29–December 1. 410–425.
- [8] Nordman E. Why the Lamu coal plant doesn't make sense. Kenya has better energy options. The Conversation. 2017 May;31. [Date of Access: 12.10.2020]. <https://theconversation.com/why-the-lamu-coal-plant-doesnt-make-sense-kenya-has-better-energy-options-78479>.
- [9] Taraba B, Michalec Z. Effect of longwall face advance rate on spontaneous heating process in the gob area–CFD modelling. Fuel. 2011 Aug 1;90(8):2790-7.
- [10] Yuan L, Smith AC. Numerical study on effects of coal properties on spontaneous heating in longwall gob areas. Fuel. 2008 Nov 1;87(15-16):3409-19.
- [11] Zhang J, Kuenzer C. Thermal surface characteristics of coal fires 1 results of in-situ measurements. Journal of Applied Geophysics. 2007 Dec 5;63(3-4):117-34.

- [12] Zhu HQ, Song ZY, Tan B, Hao YZ. Numerical investigation and theoretical prediction of self-ignition characteristics of coarse coal stockpiles. *Journal of Loss Prevention in the Process Industries*. 2013 Jan 1;26(1):236-44.
- [13] Ozdeniz AH, Corumluoglu O, Kalayci I. The relationship between the natural compaction and the spontaneous combustion of industrial-scale coal stockpiles. *Energy Sources, Part A: Recovery, Utilization, and Environmental Effects*. 2010 Nov 15;33(2):121-9.
- [14] Hu X, Yang S, Zhou X, Yu Z, Hu C. Coal spontaneous combustion prediction in gob using chaos analysis on gas indicators from upper tunnel. *Journal of Natural Gas Science and Engineering*. 2015 Sep 1;26:461-9.
- [15] Ren XW, Wang FZ, Guo Q, Zuo ZB, Fang QS. Application of foam-gel technique to control CO exposure generated during spontaneous combustion of coal in coal mines. *Journal of occupational and environmental hygiene*. 2015 Nov 2;12(11):D239-45.
- [16] Du X, Cao D, Mishra D, Bernardes S, Jordan TR, Madden M. Self-adaptive gradient-based thresholding method for coal fire detection using ASTER thermal infrared data, Part I: Methodology and decadal change detection. *Remote sensing*. 2015 Jun;7(6):6576-610.
- [17] Rosema A, Guan H, Veld H, Vekerdy Z, Ten Katen A, Prakash A. Manual of coal fire detection and monitoring. Report of the project: Development and implementation of a coal fire monitoring and fighting system in China, 245p. 1999.
- [18] <https://encrypted-tbn0.gstatic.com/images?q=tbn:ANd9GcQMgijj-63BZjS4jT-gJfO0HDIEVY8vi-zL9A&usqp=CAU> [Date of Access: 22.11.2020]
- [19] Van Genderen JL, Haiyan G. Environmental monitoring of spontaneous combustion in the North China coalfields: final report to European Commission.
- [20] Melody SM, Johnston FH. Coal mine fires and human health: What do we know?. *International Journal of Coal Geology*. 2015 Dec 1;152:1-4.
- [21] Bhattacharya A, Reddy S. Underground and surface coal mine fire detection in India's Jharia coal field using airborne thermal infrared data. *Asian Pacific Remote Sensing Journal*. 1994;7:59-73.

- [22] Demirel N, Emil MK, Duzgun HS. Surface coal mine area monitoring using multi-temporal high-resolution satellite imagery. *International journal of Coal geology*. 2011 Apr 1;86(1):3-11.
- [23] Han Y, Li M, Li D. Vegetation index analysis of multi-source remote sensing data in coal mine wasteland. *New Zealand Journal of Agricultural Research*. 2007 Dec 1;50(5):1243-8.
- [24] Lima AT, Mitchell K, O'Connell DW, Verhoeven J, Van Cappellen P. The legacy of surface mining: Remediation, restoration, reclamation and rehabilitation. *Environmental Science & Policy*. 2016 Dec 1;66:227-33.
- [25] Feng Y, Wang J, Bai Z, Reading L. Effects of surface coal mining and land reclamation on soil properties: A review. *Earth-Science Reviews*. 2019 Apr 1;191:12-25.
- [26] Ranjan A, Zhao Y, Sahu HB, Misra P. Opportunities and challenges in health sensing for extreme industrial environment: perspectives from underground mines. *IEEE Access*. 2019 Sep 13;7:139181-95.
- [27] Zhang J, Wagner W, Prakash A, Mehl H, Voigt S. Detecting coal fires using remote sensing techniques. *International journal of Remote sensing*. 2004 Aug 1;25(16):3193-220.
- [28] Zhang X, Van Genderen JL, Kroonenberg SB. A method to evaluate the capability of Landsat-5 TM band 6 data for sub-pixel coal fire detection. *International Journal of Remote Sensing*. 1997 Oct 1;18(15):3279-88.
- [29] Kuenzer C, Hecker C, Zhang J, Wessling S, Wagner W. The potential of multidirectional MODIS thermal band data for coal fire detection. *International Journal of Remote Sensing*. 2008 Feb 1;29(3):923-44.
- [30] Li F, Li J, Liu X, Meng X. Coal fire detection and evolution of trend analysis based on CBERS-04 thermal infrared imagery. *Environmental Earth Sciences*. 2020 Aug;79(16):1-5.
- [31] Hecker C, Kuenzer C, Zhang J. Remote-sensing-based coal-fire detection with low-resolution MODIS data. *Geology of coal fires: case studies from around the world: Geological Society of America, Reviews in Engineering Geology*. 2007;18:229-39.

- [32] Agarwal R, Singh D, Chauhan DS, Singh KP. Detection of coal mine fires in the Jharia coal field using NOAA/AVHRR data. *Journal of Geophysics and engineering*. 2006 Sep 1;3(3):212-8.
- [33] Song Z, Kuenzer C, Zhu H, Zhang Z, Jia Y, Sun Y, Zhang J. Analysis of coal fire dynamics in the Wuda syncline impacted by fire-fighting activities based on in-situ observations and Landsat-8 remote sensing data. *International Journal of Coal Geology*. 2015 Mar 1;141:91-102.
- [34] Haiyan G. Spontaneous coal seam fires: the Chinese perspective. In *Spontaneous Coal Seam Fires: Mitigating a Global Disaster—International Conference, Beijing, PR China, November 29–December 1, 2005* 2005 (pp. 67-81). Beijing, China: Tsinghua University Press and Springer.
- [35] He X, Yang X, Luo Z, Guan T. Application of unmanned aerial vehicle (UAV) thermal infrared remote sensing to identify coal fires in the Huojitu coal mine in Shenmu city, China. *Scientific Reports*. 2020 Aug 17;10(1):1-3.
- [36] Nayak S. Remote sensing for national development: the legacy of Dr. Vikram Sarabhai. *Journal of the Indian Society of Remote Sensing*. 2020 Sep 2:1-20.
- [37] Mishra RK, Pandey JK, Pandey J, Kumar S, Roy PN. Detection and analysis of coal fire in Jharia Coalfield (JCF) using Landsat remote sensing data. *Journal of the Indian Society of Remote Sensing*. 2020 Feb;48(2):181-95.
- [38] Xue Y, Liu J, Li J, Shang C, Zhao J, Zhang M. Use of Landsat thermal imagery for dynamically monitoring spontaneous combustion of Datong Jurassic coalfields in China. *Journal of Earth System Science*. 2018 Jun;127(4):1-1.
- [39] Biswal SS, Gorai AK. Detection and Delineation of Subsurface Coal Mine Fire from Spaceborne Thermal Infrared Data in Jharia Coalfield, Dhanbad, India. *International Archives of the Photogrammetry, Remote Sensing and Spatial Information Sciences*. 2019 Sep 3;42(3/W8).
- [40] Mishra RK, Bahuguna PP, Singh VK. Detection of coal mine fire in Jharia Coal Field using Landsat-7 ETM+ data. *International journal of coal geology*. 2011 Apr 1;86(1):73-8.
- [41] Zablotskii VR. The application of LANDSAT multi-temporal thermal infrared data to identify coal fire in the Khanh Hoa coal mine, Thai Nguyen province, Vietnam. *Izvestiya, Atmospheric and Oceanic Physics*. 2017 Dec;53(9):1081-7.

- [42] Valor E, Caselles V. Mapping land surface emissivity from NDVI: Application to European, African, and South American areas. *Remote sensing of Environment*. 1996 Sep 1;57(3):167-84.
- [43] Van de Griend AA, OWE M. On the relationship between thermal emissivity and the normalized difference vegetation index for natural surfaces. *International Journal of remote sensing*. 1993 Apr 1;14(6):1119-31.
- [44] Gangopadhyay PK, Lahiri-Dutt K, Saha K. Application of remote sensing to identify coalfires in the Raniganj Coalbelt, India. *International Journal of Applied Earth Observation and Geoinformation*. 2006 Sep 1;8(3):188-95.
- [45] Huo H, Ni Z, Gao C, Zhao E, Zhang Y, Lian Y, Zhang H, Zhang S, Jiang X, Song X, Zhou P. A study of coal fire propagation with remotely sensed thermal infrared data. *Remote Sensing*. 2015 Mar;7(3):3088-113.
- [46] Cracknell AP, Mansor SB. Detection of sub-surface coal fires using Landsat Thematic Mapper data. *International Archives of Photogrammetry and Remote Sensing*. 1993;29:750-.
- [47] Jiang W, Zhu X, Wu J, Gu L, Ma G, Liu X. Retrieval and analysis of coal fire temperature in Wuda coalfield, Inner Mongolia, China. *Chinese Geographical Science*. 2011 Apr 1;21(2):159-66.
- [48] Bhattacharya A, Reddy S, Mukherjee T. Multi-tier remote sensing data analysis for coal fire mapping in Jharia coalfield of Bihar, India. In *Proceedings of the Twelfth Asian conference on remote sensing 1991 Oct 30* (pp. 22-1). National University of Singapore Singapore.
- [49] Mukherjee TK, Bandyopadhyay TK, Pande SK. Detection and delineation of depth of subsurface coalmine fires based on an airborne multispectral scanner survey in a part of the Jharia Coalfield, India. *Photogrammetric Engineering and Remote Sensing*. 1991 Sep;57(9).
- [50] MAnSoR SB, CRACKnEll AP, Shilin BV, Gornyi VI. Monitoring of underground coal fires using thermal infrared data. *International Journal of Remote Sensing*. 1994 May 20;15(8):1675-85.
- [51] Prakash A, Saraf AK, Gupta RP, Dutta M, Sundaram RM. Surface thermal anomalies associated with underground fires in Jharia coal mines, India. *International Journal of Remote Sensing*. 1995 Aug 1;16(12):2105-9.

- [52] Prakash A, Gupta RP, Saraf AK. A Landsat TM based comparative study of surface and subsurface fires in the Jharia coalfield, India. *International journal of remote sensing*. 1997 Jul 1;18(11):2463-9.
- [53] Gangopadhyay PK, Maathuis B, Van Dijk P. ASTER-derived emissivity and coal-fire related surface temperature anomaly: a case study in Wuda, north China. *International Journal of Remote Sensing*. 2005 Dec 20;26(24):5555-71.
- [54] Chen Y, Jing L, Bo Y, Shi P, Zhang S. Detection of coal fire location and change based on multi-temporal thermal remotely sensed data and field measurements. *International Journal of Remote Sensing*. 2007 Aug 10;28(15):3173-9.
- [55] Saatçılar R, İnan S, Cankurtaranlar A, Duygun F, Demirbağ E, Ergintav S, Yılmaz M, Toygar AR, Kösebalaban A, Yalçın MN. An environmentally-friendly integrated seismic imaging for coal exploration in the Miocene Soma Basin, Western Turkey. *International Journal of Oil, Gas and Coal Technology*. 2014 Jan 1;7(4):399-414.
- [56] <http://www.eli.gov.tr/> [Date of Access: 10.12.2020]
- [57] Wulder MA, Loveland TR, Roy DP, Crawford CJ, Masek JG, Woodcock CE, Allen RG, Anderson MC, Belward AS, Cohen WB, Dwyer J. Current status of Landsat program, science, and applications. *Remote sensing of environment*. 2019 May 1;225:127-47.
- [58] Bhattacharya A, Reddy CS, Dangwal M. Coal mine fire inventory and monitoring in Jharia coalfield Bihar, India, using thematic mapper thermal IR data. Environmental Research Institute of Michigan (ERIM), Ann Arbor, MI (United States); 1996 Aug 1.
- [59] Saraf AK, Gupta RP, Kumar A. Remote sensing technique in underground fire detection in coal mines of Jharia. India: Tata-McGraw-Hill Publications; 1992 Feb.
- [60] SARAF AK, PRAKASH A, Sengupta S, GUPTA RP. Landsat-TM data for estimating ground temperature and depth of subsurface coal fire in the Jharia coalfield, India. *International Journal of Remote Sensing*. 1995 Aug 1;16(12):2111-24.
- [61] Prakash A, Saraf AK, Gupta RP, Dutta M, Sundaram RM. Surface thermal anomalies associated with underground fires in Jharia coal mines, India. *International Journal of Remote Sensing*. 1995 Aug 1;16(12):2105-9.

- [62] Wan Z, Dozier J. A generalized split-window algorithm for retrieving land-surface temperature from space. *IEEE Transactions on geoscience and remote sensing*. 1996 Jul;34(4):892-905.
- [63] Rothery DA, Francis PW, Wood CA. Volcano monitoring using short wavelength infrared data from satellites. *Journal of Geophysical Research: Solid Earth*. 1988 Jul 10;93(B7):7993-8008.
- [64] Francis PW, De Silva SL. Application of the Landsat Thematic Mapper to the identification of potentially active volcanoes in the Central Andes. *Remote Sensing of Environment*. 1989 Apr 1;28:245-55.
- [65] Raju A, Gupta RP, Prakash A. Delineation of coalfield surface fires by thresholding Landsat TM-7 day-time image data. *Geocarto International*. 2013 Jul 1;28(4):343-63.
- [66] Reddy CS, Srivastav SK, Bhattacharya A. Application of Thematic Mapper short wavelength infrared data for the detection and monitoring of high temperature related geoenvironmental features. *International Journal of Remote Sensing*. 1993 Nov 1;14(17):3125-32.
- [67] Gupta RK, Badarinath KV. Volcano monitoring using remote sensing data. *International Journal of Remote Sensing*. 1993 Nov 1;14(16):2907-18.
- [68] Andres RJ, Rose WI. Description of thermal anomalies on 2 active Guatemalan volcanos using Landsat Thematic Mapper imagery. *Photogrammetric engineering and remote sensing*. 1995;61(6):775.
- [69] Zhang X. Coal fires in Northwest China. Detection, monitoring, and prediction using remote sensing data.
- [70] <https://eos.com/find-satellite/landsat-8/> [Date of Access: 04.02.2021]
- [71] Yu X, Guo X, Wu Z. Land surface temperature retrieval from Landsat 8 TIRS—Comparison between radiative transfer equation-based method, split window algorithm and single channel method. *Remote sensing*. 2014 Oct;6(10):9829-52.
- [72] Rajeshwari A, Mani ND. Estimation of land surface temperature of Dindigul district using Landsat 8 data. *International Journal of Research in Engineering and Technology*. 2014 May;3(5):122-6.
- [73] Wang M, Zhang Z, Hu T, Liu X. A practical single-channel algorithm for land surface temperature retrieval: application to Landsat series data. *Journal of Geophysical Research: Atmospheres*. 2019 Jan 16;124(1):299-316.

- [74] Greene GW, Moxham RM, Harvey AH. Aerial infrared surveys and borehole temperature measurements of coal mine fires in Pennsylvania. *Remote Sensing of Environment*, VI. 1969:517.
- [75] Ellyett CD, Fleming AW. Thermal infrared imagery of the Burning Mountain coal fire. *Remote Sensing of Environment*. 1974 Jan 1;3(1):79-86.
- [76] Peng WX, Van Genderen JL, Kang GF, Guan HY, Tan YJ. Estimating the depth of underground coal fires using data integration techniques. *Terra Nova*. 1997 Dec;9(4):180-3.
- [77] Lillesand TM, Kiefer RW, Chipman JW. *Remote sensing and image interpretation*. John Willey & Sons. New York. 2000;724.
- [78] Chen W, editor. *Neonatal monitoring technologies: design for integrated solutions: design for integrated solutions*. IGI Global; 2012 Apr 30.
- [79] Wang C, Maathuis BH, Prakash A, Dijk VP. Detection of coal fires in Xinjiang (China) using remote sensing techniques. *Deposits and Geoenvironmental Models For Resources Exploitation and Environmental Security II*. 2002 Apr 5:23.
- [80] Zhang X, Zhang J, Künzer C, Voigt S, Wagner W. Capability evaluation of 3–5  $\mu$  m and 8–12.5  $\mu$  m airborne thermal data for underground coal fire detection. *International Journal of Remote Sensing*. 2004 Jun 1;25(12):2245-58.
- [81] van Genderen JL, Cassells CJ, Xiangmin Z. The synergistic use of remotely sensed data for the detection of underground coal fires.
- [82] Markham BL, Barker JL. Spectral characterization of the Landsat Thematic Mapper sensors. *International Journal of Remote Sensing*. 1985 May 1;6(5):697-716.
- [83] <https://www.usgs.gov/core-science-systems/nli/landsat> [Date of Access: 10.02.2021]
- [84] Song C, Woodcock CE, Seto KC, Lenney MP, Macomber SA. Classification and change detection using Landsat TM data: when and how to correct atmospheric effects?. *Remote sensing of Environment*. 2001 Feb 1;75(2):230-44.
- [85] Chavez Jr PS. An improved dark-object subtraction technique for atmospheric scattering correction of multispectral data. *Remote sensing of environment*. 1988 Apr 1;24(3):459-79.



- [86] Chavez PS. Image-based atmospheric corrections-revisited and improved. *Photogrammetric engineering and remote sensing*. 1996 Sep 1;62(9):1025-35.
- [87] Sobrino JA, Jiménez-Muñoz JC, Paolini L. Land surface temperature retrieval from LANDSAT TM 5. *Remote Sensing of environment*. 2004 Apr 30;90(4):434-40.
- [88] Sobrino JA, Jiménez-Muñoz JC, Paolini L. Land surface temperature retrieval from LANDSAT TM 5. *Remote Sensing of environment*. 2004 Apr 30;90(4):437.
- [89] Hadjimitsis DG, Papadavid G, Agapiou A, Themistocleous K, Hadjimitsis MG, Retalis A, Michaelides S, Chrysoulakis N, Toullos L, Clayton CR. Atmospheric correction for satellite remotely sensed data intended for agricultural applications: impact on vegetation indices. *Natural Hazards and Earth System Sciences*. 2010 Jan 14;10(1):89-95.
- [90] Saini V, Tiwari RK, Gupta RP. Comparison of FLAASH and QUAC atmospheric correction methods for Resourcesat-2 LISS-IV data. In *Earth Observing Missions and Sensors: Development, Implementation, and Characterization IV 2016 May 2 (Vol. 9881, p. 98811V)*. International Society for Optics and Photonics.
- [91] [https://www.ctahr.hawaii.edu/miuralab/projects/makaha/intro\\_RS.html](https://www.ctahr.hawaii.edu/miuralab/projects/makaha/intro_RS.html) [Date of Access: 22.02.2021]
- [92] Jensen JR. *Introductory digital image processing: a remote sensing perspective*. Prentice-Hall Inc.; 1996.
- [93] Ceballos-Silva A, Lopez-Blanco J. Delineation of suitable areas for crops using a Multi-Criteria Evaluation approach and land use/cover mapping: a case study in Central Mexico. *Agricultural systems*. 2003 Aug 1;77(2):117-36.
- [94] Hu J, Chen W, Li X, He X. Roof confusion removal for accurate vegetation extraction in the urban environment. In *2008 International Workshop on Earth Observation and Remote Sensing Applications 2008 Jun 30 (pp. 1-7)*. IEEE.
- [95] Backlund P, Janetos A, Schimel D. *The effects of climate change on agriculture, land resources, water resources, and biodiversity in the United States. Synthesis and Assessment Product 4.3*. Washington, DC: US Environmental Protection Agency, Climate Change Science Program. 240 p.. 2008.

- [96] Pettorelli N, Vik JO, Mysterud A, Gaillard JM, Tucker CJ, Stenseth NC. Using the satellite-derived NDVI to assess ecological responses to environmental change. *Trends in ecology & evolution*. 2005 Sep 1;20(9):503-10.
- [97] <https://static.eos.com/wp-content/uploads/2020/07/tree.jpg> [Date of Access: 08.03.2021]
- [98] Tucker CJ. Red and photographic infrared linear combinations for monitoring vegetation. *Remote sensing of Environment*. 1979 May 1;8(2):127-50.
- [99] Purevdorj TS, Tateishi R, Ishiyama T, Honda Y. Relationships between percent vegetation cover and vegetation indices. *International journal of remote sensing*. 1998 Dec 1;19(18):3519-35.
- [100] Mondal P. Quantifying surface gradients with a 2-band Enhanced Vegetation Index (EVI2). *Ecological Indicators*. 2011 May 1;11(3):918-24.
- [101] Ke Y, Im J, Lee J, Gong H, Ryu Y. Characteristics of Landsat 8 OLI-derived NDVI by comparison with multiple satellite sensors and in-situ observations. *Remote Sensing of Environment*. 2015 Jul 1;164:298-313.
- [102] Li ZL, Wu H, Wang N, Qiu S, Sobrino JA, Wan Z, Tang BH, Yan G. Land surface emissivity retrieval from satellite data. *International Journal of Remote Sensing*. 2013 May 1;34(9-10):3084-127.
- [103] Dash P, Göttsche FM, Olesen FS, Fischer H. Land surface temperature and emissivity estimation from passive sensor data: Theory and practice-current trends. *International Journal of remote sensing*. 2002 Jan 1;23(13):2563-94.
- [104] Cristóbal J, Jiménez-Muñoz JC, Sobrino JA, Ninyerola M, Pons X. Improvements in land surface temperature retrieval from the Landsat series thermal band using water vapor and air temperature. *Journal of Geophysical Research: Atmospheres*. 2009 Apr 27;114(D8).
- [105] Jiménez-Muñoz JC, Sobrino JA. A single-channel algorithm for land-surface temperature retrieval from ASTER data. *IEEE Geoscience and Remote Sensing Letters*. 2009 Sep 22;7(1):176-9.
- [106] Jiménez-Muñoz JC, Sobrino JA. A generalized single-channel method for retrieving land surface temperature from remote sensing data. *Journal of geophysical research: atmospheres*. 2003 Nov 27;108(D22).
- [107] Becker F, Li ZL. Towards a local split window method over land surfaces. *Remote Sensing*. 1990 Mar 1;11(3):369-93.

- [108] Coll C, Caselles V, Sobrino JA, Valor E. On the atmospheric dependence of the split-window equation for land surface temperature. *Remote sensing*. 1994 Jan 1;15(1):105-22.
- [109] Price JC. Land surface temperature measurements from the split window channels of the NOAA 7 Advanced Very High Resolution Radiometer. *Journal of Geophysical Research: Atmospheres*. 1984 Aug 20;89(D5):7231-7.
- [110] Sobrino JA, Caselles V, Coll C. Theoretical split-window algorithms for determining the actual surface temperature. *Il Nuovo Cimento C*. 1993 May 1;16(3):219-36.
- [111] Sobrino JA, Li ZL, Stoll MP, Becker F. Improvements in the split-window technique for land surface temperature determination. *IEEE Transactions on Geoscience and Remote Sensing*. 1994 Mar;32(2):243-53.
- [112] Sobrino JA, Li ZL, Stoll MP, Becker F. Multi-channel and multi-angle algorithms for estimating sea and land surface temperature with ATSR data. *International Journal of Remote Sensing*. 1996 Jul 1;17(11):2089-114.
- [113] Amiri R, Weng Q, Alimohammadi A, Alavipanah SK. Spatial-temporal dynamics of land surface temperature in relation to fractional vegetation cover and land use/cover in the Tabriz urban area, Iran. *Remote sensing of environment*. 2009 Dec 15;113(12):2606-17.
- [114] Corumluoglu O, Asri I. The effect of urban heat island on Izmir's city ecosystem and climate. *Environmental Science and Pollution Research*. 2015 Mar;22(5):3202-11.
- [115] Qin Z, Karnieli A, Berliner P. A mono-window algorithm for retrieving land surface temperature from Landsat TM data and its application to the Israel-Egypt border region. *International journal of remote sensing*. 2001 Jan 1;22(18):3719-46.
- [116] Coll C, Caselles V, Valor E, Niclòs R. Comparison between different sources of atmospheric profiles for land surface temperature retrieval from single channel thermal infrared data. *Remote Sensing of Environment*. 2012 Feb 15;117:199-210.
- [117] Wang F, Qin Z, Song C, Tu L, Karnieli A, Zhao S. An improved mono-window algorithm for land surface temperature retrieval from Landsat 8 thermal infrared sensor data. *Remote sensing*. 2015 Apr;7(4):4268-89.

- [118] Jiménez-Muñoz JC, Sobrino JA, Skoković D, Mattar C, Cristóbal J. Land surface temperature retrieval methods from Landsat-8 thermal infrared sensor data. *IEEE Geoscience and remote sensing letters*. 2014 Apr 8;11(10):1840-3.
- [119] Artis DA, Carnahan WH. Survey of emissivity variability in thermography of urban areas. *Remote sensing of Environment*. 1982 Sep 1;12(4):313-29.
- [120] Chander G, Markham B. Revised Landsat-5 TM radiometric calibration procedures and postcalibration dynamic ranges. *IEEE Transactions on geoscience and remote sensing*. 2003 Nov 17;41(11):2674-7.
- [121] Jiménez-Muñoz JC, Sobrino JA. Error sources on the land surface temperature retrieved from thermal infrared single channel remote sensing data. *International Journal of Remote Sensing*. 2006 Mar 1;27(05):999-1014.
- [122] Li H, Liu Q, Du Y, Jiang J, Wang H. Evaluation of the NCEP and MODIS atmospheric products for single channel land surface temperature retrieval with ground measurements: A case study of HJ-1B IRS data. *IEEE Journal of selected topics in applied earth observations and remote sensing*. 2013 Apr 11;6(3):1399-408.
- [123] CORUMLUOGLU O. SSD Analyze for the Assessment of Long Term Thermal Effect of Urbanization on the Izmir City's Local Climate Change.

# Appendices

# Appendix A

## Publications from the Thesis

### **Conference Papers**

1. Detection Of Soma Coal Mine Fire Areas By Time Series Analysis Of Landsat Thermal Images

Republic of Turkey  
İzmir Kâtip Çelebi University  
Graduate School of Natural and Applied Sciences

# Detection of Coal Fires in Soma with Landsat Temporal Thermal Images

Department of Geomatics Engineering  
Master's Thesis

Merve KÖŞKER

Thesis Advisor: Prof. Dr. Özşen ÇORUMLUOĞLU

June 2022

**KÖŞKER**      **Detection of Coal Fires in Soma with Landsat Temporal Thermal Images**  
**MASTER' S THESIS**      **2022**



# Curriculum Vitae

Name Surname : Merve KÖŞKER  
E-mail (1) : Y190212001@ogr.ikcu.edu.tr  
E-mail (2) : mervekoskertr@gmail.com

## Education:

2014–2019 İzmir Kâtip Çelebi University, Dept. of Geomatics Eng.  
2019–2022 İzmir Kâtip Çelebi University, Dept. of Geomatics Eng.

## Work Experience:

2021 Erikçi Harita Mühendislik Bürosu  
2021 İstanbul Büyükçekmece 3.Bölge Kamulaştırma Birim Başmühendisliği